4D SEISMIC RESEVOIR SIMULATION: AN ALTERNATIVE APPROACH TO IMPROVE THE PERMEABILITY FIELD THROUGH THE USE OF TIME-LAPSE SEISMIC DATA

A thesis submitted to **The University of Manchester**

for the degree of **MSc by Research**

in **Basin Analysis and Petroleum Geoscience**

in the faculty of **Engineering and Physical Sciences**

2012

SALOMÃO MARAVILHOSO CHISSONDE

School of Earth, Atmospheric and Environmental Sciences

This page intentionally left blank

LIST OF CONTENTS

Final word count: 27371

NOMENCLATURE

Symbol

λ = phase mobility [m^2/Pa s]

μ = phase viscosity [Pa s and cP]

ρ = phase density [kg/m^3]

S_o = saturation of oil

S_w = saturation of water

S_w = saturation of gas

$\varnothing$ = porosity

K = absolute permeability [mD or m^2]

k_{ro} = relative permeability of oil

k_{rg} = relative permeability of gas

k_{rw} = relative permeability of water

t = time [s]

x = distance [m]

y = distance [m]

z = depth [m]

mD = millidarcies

D = darcies

V_p = compressional wave velocity [m/s]

V_s = shear wave velocity [m/s]

I = number of grid points or blocks in x-direction

J = number of grid points or blocks in y-direction

P = pressure [Pa, bar or psi]

P_c = capillary pressure [Pa]

T = temperature [°F or °R]

c_f = compressibility factor [1/psi]

R_{so} = solution gas-oil-ratio [scf/bbl]

g = gravitational acceleration [m/s^2]

f_w = fractional flow

h_w = function of saturation involving mobility and capillarity [m^2/s]

Q = total volumetric rate [m^3/d]

A = area

Δ = difference

$\dfrac{\partial f}{\partial x}$ = partial derivative of f with respect to x

∇ = numerical operator

$$\nabla . f = \frac{\partial f}{\partial x} + \frac{\partial f}{\partial y} + \frac{\partial f}{\partial z}$$

A_0 = Initial amplitude of the seismic wavelet

A_1 = final amplitude of the seismic wavelet

Δ = Difference

ΔA = change in 4D seismic amplitude

ΔS = average saturation change

ΔGOR = average GOR change

ΔP = average pressure change

Knew = new permeability

Subscripts and superscripts

abs   absolute parameter/quantity

avg   average parameter/quantity

g   gas phase

i   index in x-direction

j   index in y-direction

n   non-wetting phase

o   oil phase

w   water phase, or wetting phase

x   refers to x-direction

y   refers to y-direction

Abbreviations

API   American Petroleum Institute

BHP   Bottom hole pressure

GOR   Gas Oil Ratio

4D   two or more 3D surveys at different times time is the fourth dimension

AVO   amplitude versus offset

NTG   net-to-gross

OWC   oil-water contact

RMS   root- mean- square

MDT   Modular formation Dynamic Tester

RFT   Repeat Formation Tester

OBN   Ocean Bottom Nodes

T0   Initial time, coincident with the date of the first seismic survey

T1   Final time, coincident with the date of the monitor seismic survey

SGS   Sequential Gaussian Simulation

MPS   Multi-Point Statistics

RT   Rotary table

UTM   Universal Transverse Mercator

LIST OF FIGURES

LIST OF TABLES

ABSTRACT

Field data from a producing field was used to correlate changes in pressure and saturation with changes in seismic attributes from 4D seismic. The correlations explored how the seismic responses and the distribution of rock properties (i.e.: permeability, pressure and saturation) are related to the changes caused by the production from a reservoir. An extended approach for estimating horizontal permeability was developed through an integrated approach involving multiple disciplines and an initial permeability model including 4D seismic and field production data. The development of the approach involved the use of mathematical, numerical and computer modelling techniques through partial differential equations and computer software to solve these equations. The robustness, applicability and accuracy of the approach were tested on the Dalia field for which a 3D static reservoir model was built for extraction of the numerical data.

The static model of the Dalia field was populated with up-scaled reservoir properties of the field in addition to information obtained from wells logs (5 oil producers and 3 water injector wells); in addition to the well data, 4D seismic data (consisting of 2 seismic volumes shot at *T0 and T1*), completion data, well trajectories, time-depth laws, horizon information, geological and geophysical information were also used. A single 2D layer model was produced by averaging reservoir properties in the vertical direction from the 3D model. The permeability estimation approaches proposed by this project were successfully implemented by building computer programs that used equations derived by the numerical analysis; the input data for the computer programs was the data quantitatively extracted from the average 2D single layer model of the Dalia field. The approach made use of an initial log-derived permeability, saturation models in addition to reservoir dynamic and rock properties. Results produced by the approach show permeability estimates that honour the input data by displaying patterns correlatable to the initial permeability model, while revealing detailed features that can be interpreted as a better distribution of the channels. Therefore, the approach has proven possible to generate detailed permeability information using 4D seismic and production data.

Permeability estimation approaches using 4D seismic have been developed before (Vasco, et al., 2004; MacBeth & Al-Maskeri, 2006). Compared to the previous work, the approach here proposed poses the advantage of being adaptable to different physical and production scenarios – oil-gas-water production and oil and water production. In essence, the method can have different applications estimating reservoir properties, updating simulation models or used as a tool that takes advantage of the advances in the computer imaging developments by making more quantitative use of the seismic data to use in parallel with traditional techniques. The uncertainty and limitations of the approach were explored and minimized where possible. The permeability estimated using the approach is dependent on the initial permeability model, the spatial distribution of the rock properties, pressure, saturation, flow properties - all related to changes in the seismic attribute.

DECLARATION

No portion of the work referred to in the dissertation has been submitted in support of an application for another degree or qualification of this or any other university or other institute of learning.

COPYRIGHT STATEMENT

i.   The author of this thesis (including any appendices and/or schedules to this thesis) owns certain copyright or related rights in it (the "Copyright") and s/he has given The University of Manchester certain rights to use such Copyright, including for administrative purposes.

ii.   Copies of this thesis, either in full or in extracts and whether in hard or electronic copy, may be made **only** in accordance with the Copyright, Designs and Patents Act 1988 (as amended) and regulations issued under it or, where appropriate, in accordance with licensing agreements which the University has from time to time. This page must form part of any such copies made.

iii.   The ownership of certain Copyright, patents, designs, trade marks and other intellectual property (the "Intellectual Property") and any reproductions of copyright works in the thesis, for example graphs and tables ("Reproductions"), which may be described in this thesis, may not be owned by the author and may be owned by third parties. Such Intellectual Property and Reproductions cannot and must not be made available for use without the prior written permission of the owner(s) of the relevant Intellectual Property and/or Reproductions.

DEDICATION

To Lucia Salatiel,

mother your efforts have finally paid off

ACKNOWLEDGMENTS

THE AUTHOR

The author of this thesis has received a Bachelor of Engineering degree in Petroleum Engineering from the University of Manchester in 2010. Having started a degree in Civil Engineering in 2004, author also worked as Civil Engineering assistant for an Engineering firm in Angola while attending university. In 2006 he received funding that allowed him to dedicate solely to his academic studies. His primary research interests include developing tools to estimate and improve reservoir properties through integrated reservoir description using time-lapse data. The author received awards of merit from his sponsors during his academic years, in addition to internships with Sonangol E.P; one of the internships served him to acquire 4D seismic and production data for this thesis as well as obtaining industrial insight.

This page intentionally left blank

CHAPTER 1   INTRODUCTION

Overview

This chapter briefly discusses some advantages of modern computers to reservoir engineering and simulation and as well as potential benefits of 4D seismic towards estimation of reservoir parameters and better understanding of the permeability. The Objectives, motivations and methodology of the project are introduced together with a road map of the project.

1.1   Introduction to reservoir Engineering and simulation

Reservoir simulation is an important tool for solving reservoir-engineering problems. Reservoir simulation combines the subjects of mathematics, computer programming, geophysics and reservoir engineering, becoming a powerful tool that can be used to predict reservoir performance optimizing hydrocarbon recovery through the allocation of resources and maximize profit while keeping capital expenses low. Computers and their ability to solve complicated numerical problems are now used to aid engineers solving otherwise difficult calculations through simulators which, despite running many automatic simultaneous iterations, are fast and efficiently produce reliable results. The primary objective in a reservoir management study is to determine the optimum conditions needed to maximize the economic recovery of hydrocarbons from a prudently operated field (Fanchi, 2001).

Time-lapse seismic (4D) is increasingly being used in the field of reservoir engineering and management for monitoring changes in the fluid properties in reservoirs during production. Fewer than expected quantitative interpretations are currently being derived from the use of 4D seismic data and the level of accuracy of the existent ones is often dependent on the resolution the seismic data (Stephen, et al., 2006).

The use of 4D seismic has led to the improvement of understanding of fluid movement in reservoirs, which in turn has allowed the location of un-accessed reserves to be identified; drilling options have been identified leading to the creation of value through increased production rate and/or recovery (Marsh, et al., 2000). However most 4D seismic is used for qualitative purposes through the identification of bright, dim and flat spots on seismic sections. A great deal of research is currently being devoted to techniques involving the use of 4D seismic data to acquire more quantitative estimates which could potentially be used to improve reservoir prediction by means of updating flow simulation models (Huang, 2001; Vasco, et al., 2004; MacBeth & Al-Maskeri, 2006).

For reservoir recovery and optimization, the development of an accurate numerical approach that extracts reservoir properties using 4D seismic could represent a groundbreaking tool to optimize hydrocarbon recovery. Efficient extraction of reservoir properties and understanding their distribution can potentially play an important role in the reduction of the uncertainty of parameters obtained through conventional techniques as well as improving interpretations provided by qualitative interpretations. The number of blocks used in reservoir models has increased to millions and seismic visualisation has evolved from 2D to 3D to 4D, similarly graphics and computer speed have also evolved, making simulations faster (Fanci, 2001). Advances in 4D seismic processing technologies can be used to produce seismic inversion tools that estimate changes in relevant reservoir properties such as pressure and saturation (Fanci, 2001) and results produced by these inversion techniques can be calibrated with confidence by core data and petrophysical information.

1.2   Aims and objectives

For the purposes of reservoir management, the present study takes advantage of the most sophisticated methodologies to improve and/or better understand the behaviour of reservoir rock properties; sophisticated methodologies to understand reservoir behaviour involve the use of computer simulations for describing and understanding fluid flow within reservoirs (Mattax et al., 1990).

The aim of the project is to use high-resolution 4D seismic and production data from the Dalia Field located offshore Angola to quantitatively improve the initial permeability estimated from well logs. The results are analysed in relation to similar approaches previously developed (MacBeth & Al-Maskeri, 2006; Vasco, et al., 1999; Vasco, et al., 2004).

The objective was to optimize field data from the Dalia Field to the needs of the project by performing pressure-saturation analysis, obtaining PVT data and dynamic properties of reservoir fluids from the field data as well as integration of all the available information of the field. Management and integration of all the field data was achieved through a static 3D reservoir model built using standard software platforms; the model allowed 3-Dimensional analysis and visualization of all the parameters, tests, interpretations and data available. In addition to the field data, the model used interpretations and results from the pressure-saturation analysis as an additional source of data.

Relevant seismic attributes at two different times were extracted from the 3D model to perform pressure-saturation inversion – a method through which changes in the seismic attribute with time and progress of the fluid saturation front were related to changes in reservoir pressure for numerical extraction of attribute information.

1.3   Motivations of the project

This project concentrates on the study of reservoir engineering for development of methodologies that use seismic and dynamic data to estimate and/or better understand reservoir rock properties and heterogeneity.

In assessing the heterogeneity of the reservoir, arguably the most significant parameter to consider is the permeability and in particular its degree of variation across the reservoir section (Willhite, 1986). The project focuses on the study of permeability because it is the belief of the author that permeability is one of the key properties to have first order impact on predictions of simulation models. The author also considers that the property plays an important role on strategies for well completion and production profiles. Furthermore, the available methods for permeability estimation don't always meet the expectations of reservoir engineers despite using reliable techniques such as core and wireline logs (Ali & Thomas, 2000). Permeability it is one of the most difficult petrophysical properties to predict (Timur, 1969), in some instances reservoirs are divided into small compartments for which average permeability values are assigned; the averaging approach has its limitations.

Standard core derived permeability measurements are obtained by passing air or nitrogen through cleaned whole cores or core plugs. Permeability is mathematically determined from plots of fluid rates. These measurements however represent localised measurements that are often extrapolated and/or used to constrain reservoir properties. Because core is the single most important piece of data from a reservoir, permeability measurements from core are regarded as high quality one despite their dependency on borehole conditions and the way core is handled (Ahmed, et al., 1989).

Interpretation problems may arise from permeability measurements acquired from core due to scale problems because core data only provides permeability measurement on a sample of the reservoir and the various permeability measurements currently available (i.e., minipermeameter, core plug or whole-core analysis) have their respective volumes of investigation that range from centimetre to meter-scale. Diagenetic features such as fractures, vugs and stylolites can

produce large-scale anisotropy due to the differences in the volumes of investigation of the available tools. Downhole logs providing permeability information have centimetre to decimetre-scales depth of investigation respectively. At the field scale, 3D models normally focus on generating sedimentary units at scales of 50 cm or a meter, vertically and of a few metres, horizontally with the implicit assumption that rocks can be considered homogeneous at smaller scales; therefore the upscalling process can only be perceived as starting with fine gridblocks used in the stochastic models up to the coarser ones in the reservoir flow simulators.

Literature shows that mathematical transforms exist and can in some cases be used with confidence to convert wireline log data into permeability. Timur (1969) estimated permeability using well log correlations from sandstones. Coates, et al., (1947), Wyllie, et al., (1950) also discuss the estimation of permeability from log data as well limitations inherent from assumptions taken by their approaches. The project used of these theoretical models to estimate the initial permeability. Some of the standard techniques for permeability estimation are listed in the *Table 1*; the table discusses the sources of data, resolution, coverage and time taken to collect the data.

Table 1: List and comparison of different methods used for permeability estimation, adapted after (Coates, et all., 1989).

Source of data	Resolution	Aerial Coverage	Remarks	Use
Core	Vertical - Excellent (0.05-0.1 m)	Poor-sparse in 1D	Scale issues	Geological models and petrophysical interpretations
Wireline log	Vertical & horizontal – very good (0.1-1 m)	1D	Indirect conversion to permeability	Geological models and petrophysical interpretations
Well testing (RFT, BUP and interference)	Well testing: Vertical – poor. Horizontal – moderate (i.e.: 30 m by 30 m by 10 m). Interference: Horizontal: Good (dependant on well distance)	Extends partly into 2D–variable radius of influence	Well testing: Run through the field life Interference test: expensive	Data analysis, static and petrophysical models
History matching	Vertical & Horizontal: Moderate (i.e.: 100 m by 100 m by 3 m)	Coarse 2D scale, as based on well data	Resolution dependant on cell size, flow type and input data	Dynamic model
3D seismic	Horizontal - good Vertical - poor (i.e.: 12.5 m 12.5 m by 12 m)	Potentially excellent	Arguable use of attenuation or porosity	Static model only
3D time-lapse (4D)	Horizontal - good. Vertical - poor (i.e.: 12.5 m 12.5 m by 12 m)	Potentially excellent	Highest potential	3D and numerical models

1.4   Methodology

Through the use of numerical modelling and simulation, two distinct 3D seismic surveys, a baseline survey, at time 0 (*T0*) and a monitor survey at time 1 (*T1*) together with field production data from the Dalia Field were used to improve the estimates of an initial permeability distribution. To derive a new approach through a set of equations that incorporate production data and 4D seismic, the author used mathematical formulae from the literature (Stroud & Booth, 2007; Peaceman, 1977). The applications of these equations were tested using real data from the Dalia field and synthetic data from a UK field.

A cohesive structure consisting of 4 main parts was designed to overcome the objectives of the project. The structure consists of:

1.4.1   Dalia data analysis and reservoir modelling

Field data form the Dalia Field was analysed, dynamic and reservoir fluid properties were extracted, these properties were then inspected in relation to published Dalia Field data (Caie, et al., 2007; Prat, et al., 2010 ; Vemba, et al., 2011). A static 3D reservoir model of the Dalia Field was built using seismic data and information obtained though analysis of the production data together with all the relevant production data and geological/sedimentological information available. Numerical data from the 3D model, pressure saturation inversion and seismic attribute information extracted from the static model was used to write the Matlab computer program.

1.4.2   Mathematical modelling

The reservoir system was modelled and all the physical processes expressed in terms of mathematical equations. All the assumptions and simplifications made to provide solutions were outlined.

Appendices B contains the fundamental equations used by the project to model fluid flow within reservoirs; these equations, from the general literature (Dake, 1978; Peaceman, 1977; Craft & Hawkins, 1959) were used to derive the partial differential equations of the *mathematical model (chapter 3)*. The objective of the mathematical model was to produce a systematic mathematical approach to estimate the permeability incorporating 4D time-lapse and production data. Two sets of equations were proposed by the project: The first one is based on those

reservoirs in the Dalia Field producing oil, gas and water; the second one is based on a reservoir producing only oil and water.

1.4.3 Numerical modelling

Due to the inherited complexity of some of the equations derived by the *mathematical model*, it was not possible to solve these analytically. Necessary approximations were needed to solve these equations with the aid of finite difference methods (Stroud & Booth, 2007).

Covered in *chapter 4,* these approximated equations are here called *numerical models* and they were generated through discretization of the equations derived by the *mathematical model*.

1.4.4 Computer modelling

To solve the numerical models, *computer programs* were written by the author; these used simple algorithms based on the differential equations derived by the numerical approach in addition to the use of software packages (i.e.: MatLab 2011) to solve numerical problems. The software platform used for integrated study and reservoir characterization was Petrel^{TM} by Schlumberger - 2010 licence. The computer models produced were custom-made to suit the objectives of the project.

The computer models built using Petrel 2010 are here referred to as *reservoir models* and these were used for characterization, dynamic modelling and petrophysical analysis in addition to extraction of numerical data for the pressure-saturation inversion.

*C*hapter 5 analyses the results produced by the computer models. For the first part, using results numerical information extracted from Dalia Field static model, horizontal permeability is estimated using the first permeability equation proposed by the project. Qualitative appreciation of the uncertainty associated with these estimates was performed considering the probabilistic nature of the approach here proposed. The second part of *chapter 5* utilizes synthetic data and the appropriate permeability equation to investigate the possibility of incorporating production and geological information into a crude permeability model.

Chapter 6 deals with the reservoir simulation and characterization of the Dalia field from geometry to mapping of the relevant petrophysical properties such as porosity, permeability, and dynamic data saturation such and pressure.

An overview of some of disciplines considered in the project is illustrated *Figure 1* to show the interaction between various disciplines; altogether an attempt to produce a cohesive strategy for more effective data integration.
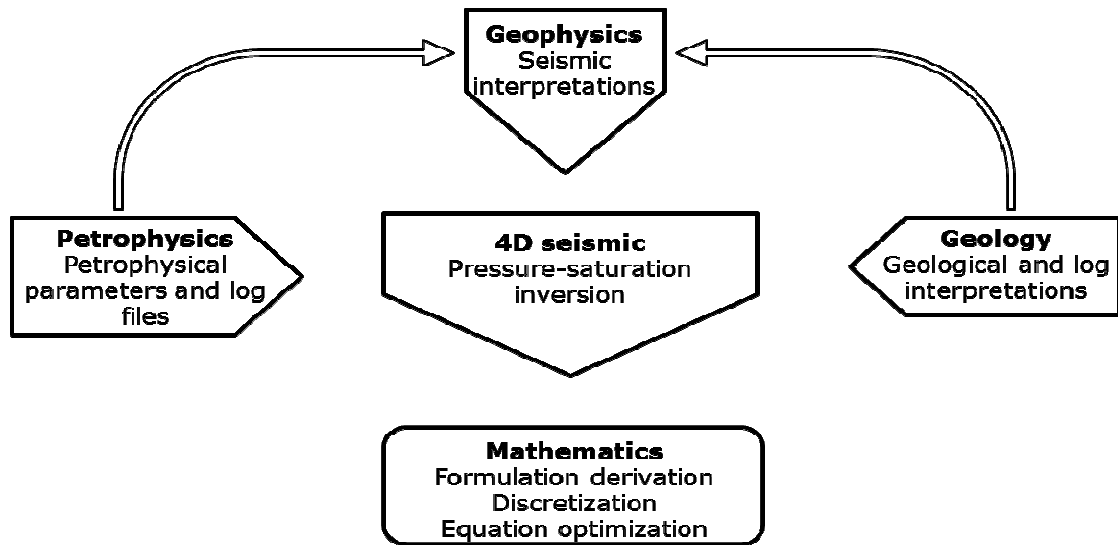
Figure 1: Interaction of the main disciplines used in the project

CHAPTER 2   THE DALIA FIELD DATA ANALYSIS AND RESERVOIR MODELLING

Overview

Field analysis, petrophysical characterization and dynamic behaviour of the reservoir were studied for the integrated approach through which the geo-cellular model was built. Initial distributions of saturation and permeability were based on theoretical models; the 3D reservoir model used these initial models as input in addition to interpretations from field data. Reservoir descriptions and geometry delineation were performed through seismic interpretation where pressure saturation inversion was achieved by attribute analysis.

2.1 Field Data analysis

2.1.1 Introduction to the Dalia field

The Dalia Field covers an area of about 230 km^2 and is located in Angola offshore of Cabinda (fig *2a*). The field was discovered in September 1997. It is estimated to contain 1 billion barrels of recoverable oil in reservoirs (Caie, et al., 2007) at 800 metres below seabed and water depths 1200-1400 metres (Picard, et al., 2007).

A seismic survey was started on the 27th August 1999 and completed on 19th October 1999. In 2006 the field was brought onto production, with a projected production system of 67 wells, of which 34 producers, 30 water injectors and 3 gas injectors.

In 2008 a conventional towed streamer survey and an OBN survey were carried out around Dalia. The conventional towed streamer survey conducted over Dalia started between July-September 2008. The 1st phase of the OBN survey was performed between September to December 2008 while the second between February to April 2009. The project used two seismic volumes covering the lower flanks of the field, the baseline survey (acquired in 2007) and the monitor survey (acquired in 2008). These volumes were used for seismic interpretation and reservoir characterization to provide an understanding of the reservoir connectivity and level of heterogeneity. Fig *2* shows the geographical location of the Field and the location of the licenced fields/blocks of Angola such as the neighbouring Girassol and Camila fields. For confidential purposes Sonangol E.P has restricted the geological information and core data from Dalia Field reservoirs. Stratigraphic information of the reservoirs can be found in Fig 66-H.
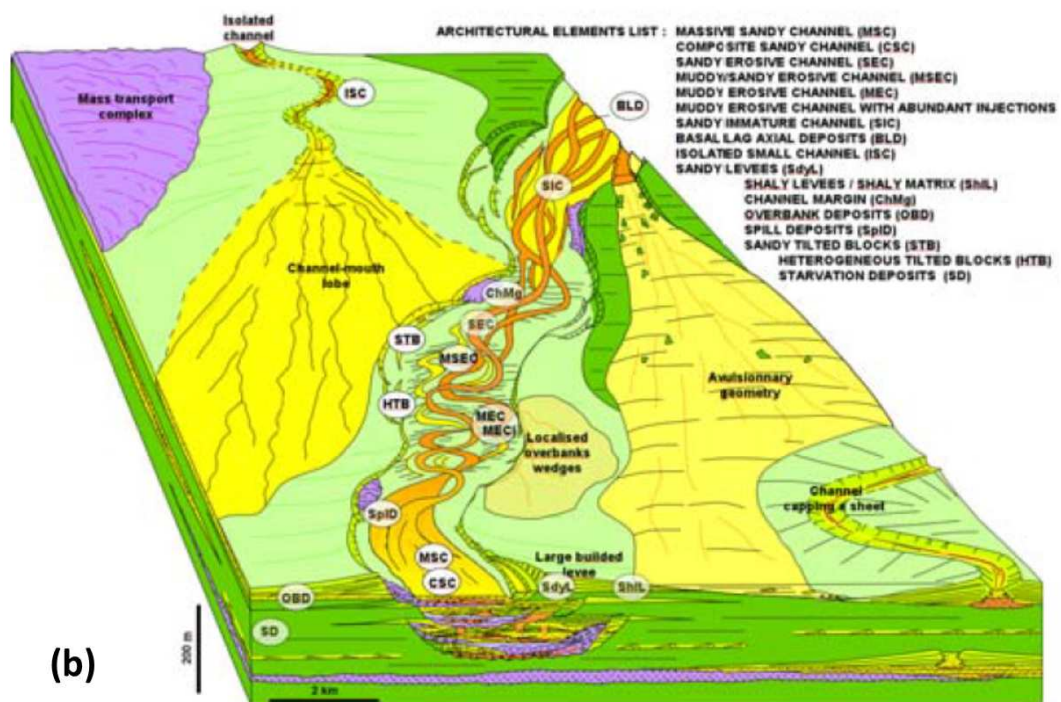
Figure 2: a) Geographical location of the Dalia field, adapted from (Aremu, 2000). **b)** Sedimentological model showing the main sand complexes in the Dalia field, after (Caie, et al., 2007).

The field is divided into four complexes comprising turbidite sediments of Lower to Middle Miocene age ±25 ma (Vemba, et al., 2011). These sediments were accumulated at the mouth of the Congo River and through turbiditic events were

moved deep offshore being deposited along edges of seabed channels (Caie, et al., 2007) where they were affected by a succession of submarine slumps at the edge of the Angolan continental shelf (Picard, et al., 2007). Oil properties from the Dalia Field show heavy oils, due to the relatively shallow depths of the reservoirs (about 800 metres). The reservoir pressures range between 215 to 235 bar while the temperatures are relatively low (*see table 2*).

The reservoirs are extensive, relatively unconsolidated and very heterogeneous. Compartmentalization of the sands by clay deposits constitutes the main source of heterogeneity given that the clays constitute flow barriers that potentially reduce/inhibit connectivity (Caie, et al., 2007). Fig 2b shows the sedimentological model that illustrates the level of heterogeneity of the reservoirs, channel distribution sand complexes.

Average characteristics of the oils in Dalia Field are summarized in *Table 2.* These properties were correlated with fluid analysis and PVT tests to calibrate properties mapped in the reservoir model.

Table 2: Average characteristics of the oil (Caie, et al., 2007)

Parameter	Value
Specific gravity	0.920 (21 – 23° API)
Viscosity	4 – 7 cP @ 40 °C
GOR	70 m^3/ m^3 (400 scf/bbl)
Reservoir pressure	215 – 235 bars
Reservoir temperature	46 – 56 °C
Reservoir water salinity	120 g/l
CO2	3-7% (gas)

2.1.2   Petrophysical data

Petrophysical information from the field shows results from analysis performed on core samples of the upper reservoir

Table 3: Petrophysical results of sample test from the uppermost reservoir

Parameter	Value	Arithmetic mean
Porosity	24.9 – 39.4 %	31.8%
Brine Permeability	0.5 – 4197 mD	966 mD
Gas Permeability	19.9 – 4872 mD	1738 mD
Grain Density	2.63 – 2.84 g/cc	2.66 g/cc
Cementation Factor	1.17 – 2.28	1.74
Reservoir permeability	3000 – 6000 mD	4500 mD
Initial Reservoir Temperature	52.6 – 56.6 °C (mid perforation 2363.5m TVD)	

PVT analysis was performed on oil and gas samples using the Modular formation Dynamic Tester (MDT) tools, the results are shown in tables in *Tables 4* and *5*.

Table 4: PVT results realised on oil and gas obtained through MDT tool

Parameter	Value
Density at BHP	835.2 kg/m^3
Viscosity at BHP	4.29 cP
Boi (process)	1.162
RSI (process)	74
Bob	1.165
Rsb	74.6
Pour point	-39 °C

Table 5: Crude oil PVT results obtained through the MDT tool

Parameter	Value
Density at 15°C	915.2 kg/m3 (23.02 °API
Organic acidity	1.90 mg KOH/g and KUOP
Characterization factor	11.68
Pour point	-39 °C

Information from *Tables 4&5* compared with results obtained by the fluid analysis; information from the fluid analysis was important for characterization of the reservoir fluids.

Although PVT results can be regarded as reliable, they should only be considered a good approximation of real fluid properties (Dake, 2001). Because the PVT information measured in the laboratory is prone to human error, often it also requires calibration to match them with other production data; therefore, the field and production data (*tables 10-15, appendix E*) was carefully examined in terms of the behaviour of dynamic properties to help identifying production regimes (i.e.: saturated or under-saturated conditions).

2.1.3   Dynamic Behaviour

The 3D static model of the Dalia Field was built using the available field data, building the model required an integrated approach for constructing spatial distribution of petrophysical parameters and fluid properties. The dynamic behaviour of the reservoir results from the evaluation of the most relevant parameters used whose distribution was crucial to interpret the inter-well reservoir properties in addition to the seismic data. Estimation of the average reservoir pressure, inspection of pressure gradient/GOR plots, and fluid rates were used to access the dynamic behaviour of the reservoir.

2.1.3.1 Dynamic production analysis

The dynamic analysis was performed through the following parameters:

Oil production

The cumulative oil production, N_p [m³] was estimated using the relationship between the oil flow rate and time, using the equation:

$$N_p = \int_0^t Q_0 \, dt \tag{2-1}$$

Where Q_o is the rate of oil [m³/d] and dt is the difference between *T0* and *T1*, [days].

The trends of the cumulative production were used to access the amount of hydrocarbons extracted from the reservoir through the producer wells (OP1-OP5). The location and distribution of the producer and injector wells is shown in Fig 57-H in the appendices. *Table 13* on the *appendix E.2* contains a summary all the well information used by the project, well utm coordinates, and the number of layers that each well penetrates and the rotary table elevation are also available on the table.
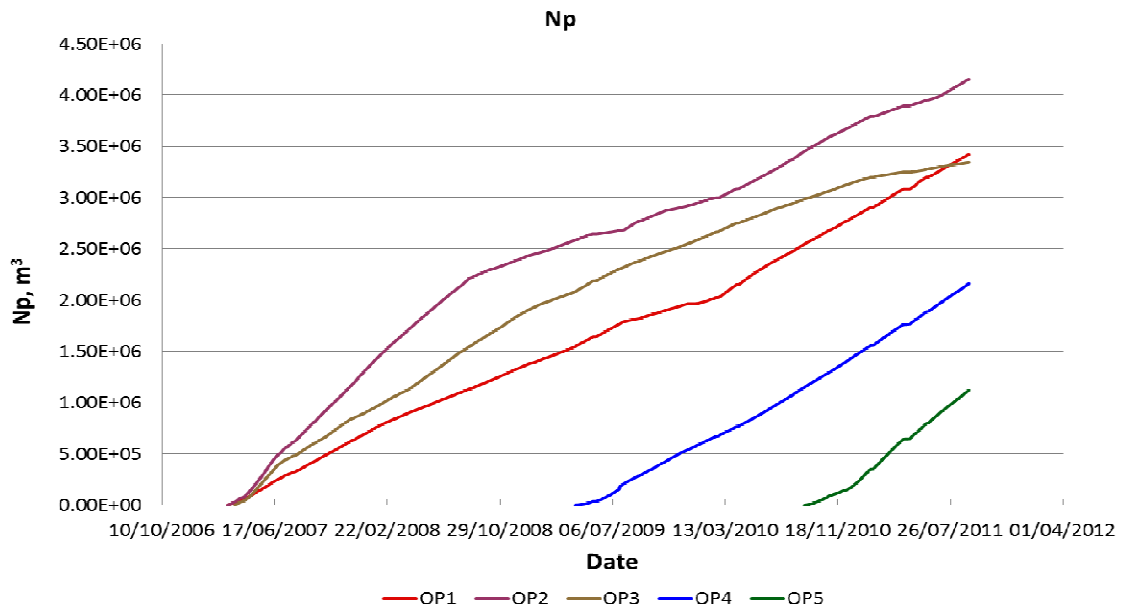
Figure 3: Cumulative oil production per well vs. time.

Close inspection of Fig 3 shows that OP2 has produced the greatest volume of hydrocarbon while well OP5 the smallest. For well OP1, between T0 and T1, oil production flow rate ranged between 500 - 2000 m³/d (fig 7b*).*

Gas-Oil-Ratio, GOR

The GOR is the ratio between the gas and oil rates, using the equation:

$$GOR = \frac{Q_g}{Q_o}$$

(2-2)

Where Q_o is the rate oil [stm^3/d] and Q_g is the rate of gas [m^3/d]

The figure below shows the behaviour of the GOR with pressure and GOR with time for well OP1 only (see *appendices E.5* for all producer wells).
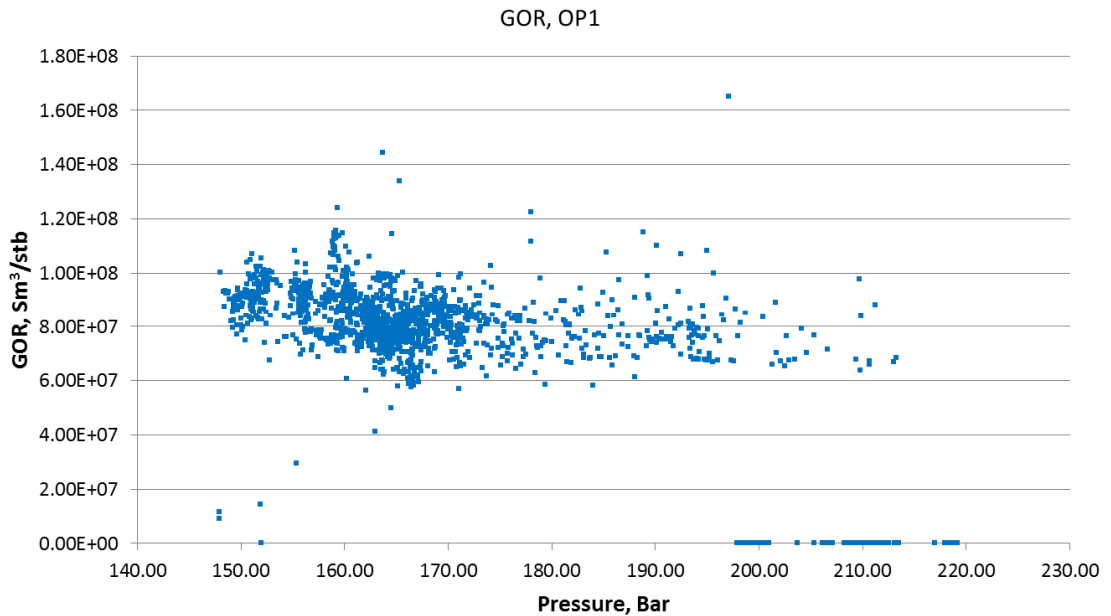
Figure 4: Behaviour of the GOR with pressure for producer OP1.

The behaviour of the GOR with pressure suggests a reservoir producing bellow bubble point; this interpretation is based on the fact that the trend of the GOR is relatively constant as pressure decreases because if the reservoir were above bubble point Fig 4 would show a significant rise of the GOR accompanied by a sudden drop in the flowing pressure indicating that the reservoir would have fallen below bubble point.

The varying behaviour of the GOR is in response to the fluctuating amount of gas being released from solution, a result of the reduction in the reservoir pressure with time (fig 7a). Simultaneous interpretation of Figs 4, 7a and 7b suggests that as reservoir pressure declines, more solution-gas is liberated from the saturated oil. Similarly, as the pressure decreases from a continually producing reservoir, the

30

rate of oil decreases (fig 7b) which is why the decrease has to be compensated by secondary recovery programme.

The behaviour of the GOR vs. pressure for the wells OP2-OP5 (*appendices E.5*) appears to be consistent with the interpretation above. Plots of GOR vs. pressure (fig 4); Reservoir pressure vs time (fig 7a) and oil flowrate vs time (fig 7b) provide further evidence that the reservoir is under saturated conditions (no gas cap). This information is important, and was used to establish the appropriate flow equations to characterize the reservoir in the *mathematical model*.

2.1.3.2 Pressure

In order to make reliable interpretations from the field data, data from Dalia Field was analysed to aid the reservoir characterization and extraction of essential reservoir information; the essential information extracted from the production data includes:

Gradient of pressure

By implementing conventional reservoir engineering techniques such as pressure-depth plots, the data available from Dalia Field was used to extract crucial information about the reservoir fluids. Pressure-depth plots require information of pressure a depth (i.e.: well log data), this information was available in form of the specialized MDT and RFT tools. When correctly interpreted pressure-depth plots of data from these tools allow interpretation of fluids types within a column, location of fluid contacts (or fluids up/down to), density and some understanding of the pressure regimes.

Pressure-depth plots were produced and the information obtained from these was compared to the results provided by the PVT tests and literature (Caie, et al., 2007). The pressure-depth plots in Fig 5 were generated using production data in *Table 11*, *appendix E. 1*.
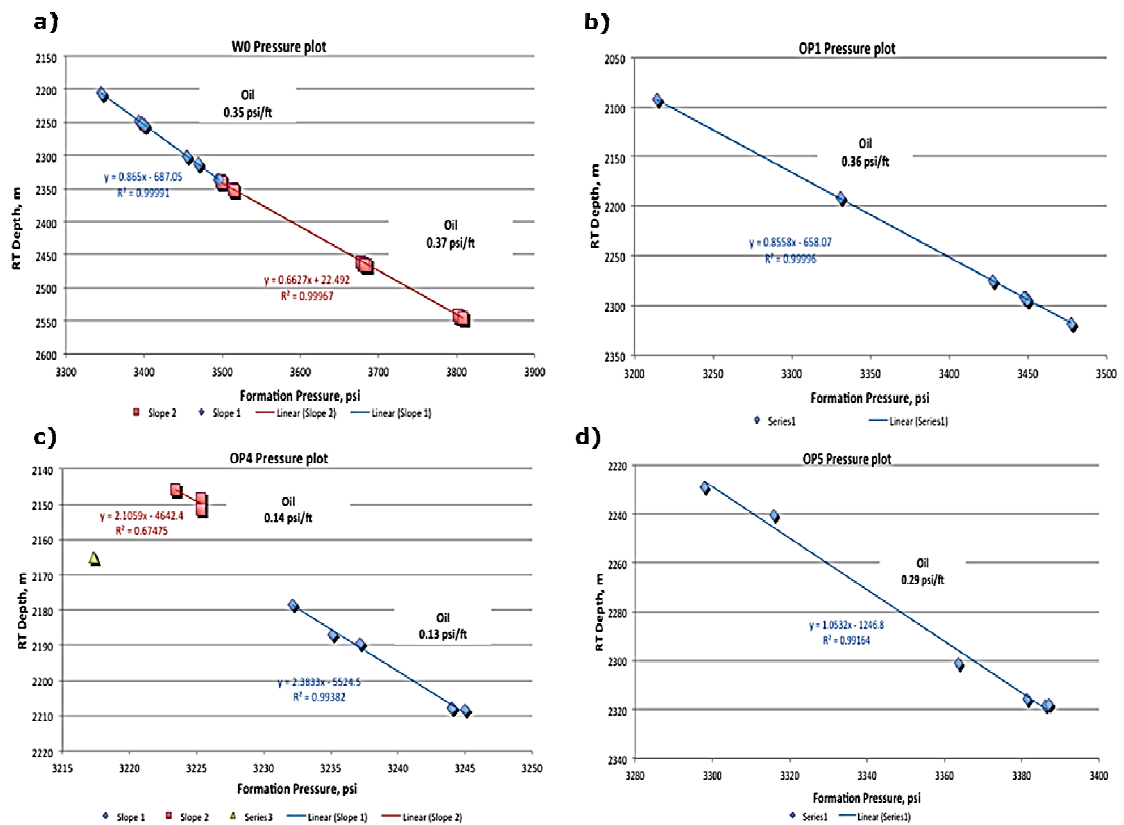
Figure 5: Pressure-depth plots obtained using data acquired by MDT and RFT tools on: **a)** Exploration well W0. **b)** Production well OP1. **c)** Production well OP4. **d)** Production well OP5

Fig 5a shows two fluid gradients (0.35 and 0,37 psi/ft), the average between the two is 0.36 psi/ft. Using the workflow in Table 12, *appendix E,* the fluid gradient from Fig 5a was being converted into density information (828 kg/m^3). Identification of reservoir fluid types was done through comparison between density information (fig 5) and typical fluid gradients (see table 6*).*

The table below contains typical values of pressure gradients used to identify the reservoir type fluids of the Dalia field.

Table 6: Typical pressure gradients for fresh water, salt water, oil and gas (Dake, 2001)

Fluid	Gradient	
Fresh water ≈	1 g/cc	0.43 psi/ft
Salt water ≈	1.2 g/cc	0.50 psi/ft
Oil <	1 g/cc	0.35 psi/ft
Gas <	0.3 g/cc	0.045 psi/ft

Correlation between *Tables 7* and *12* identified the main reservoir fluid of the Dalia Field as oil with a density between 812 - 843 kg/m³, this information agrees with the results of PVT petrophysical data of the field (*table 4*) showing oil density of 835.2 kg/m³. Giving the degree of agreement in the fluid analysis and reported PVT data, it can be concluded that the pressure-depth plots and the fluid analysis successfully characterizes the reservoir fluids and the results can be used with confidence.

Average pressure

This parameter was estimated using a relationship between fluid data (*table 12, appendices E*), Mid-Perforation depth (table 3) and height of the hydrocarbon column (estimated as the difference between the top and base of the reservoir interval (table 11*, appendices E*). The expression to estimate the pressure at reservoir conditions was derived using the concept of hydrostatic pressure regimes (Dake, 1978) and a conceptual reservoir with 2 fluids, oil and water (fig 6*)* where the pressure at the reservoir ($P_{@res}$) is proportional to the difference between the bottom hole pressure (BHP) and pressure gradient of the fluid (dp/dD) by the height of the oil column (h):

$$ P_{1@res} = BHP - \left(\frac{dp}{dD} \right)_{oil} \times h_1 \qquad (2\text{-}3) $$
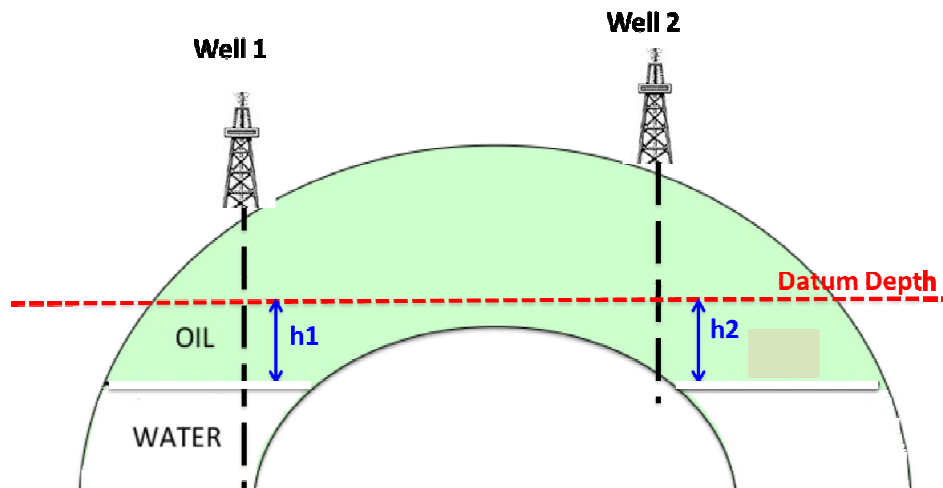
Figure 6: Schematic representation conceptual reservoir used to derive expression for the average reservoir (fluid contacts not identified).

Interpretation of the pressure trends (fig 7a) together with the behaviour of the GOR trend (fig 5) and oil flow rate (fig 7b) were used to understand the reservoir

flow pressure regimes (observing wetter a gas cap is present or whether the reservoir is under-saturated). The figures below show the behaviour of the reservoir pressure with time and the oil flow rate with time for well OP1 only.
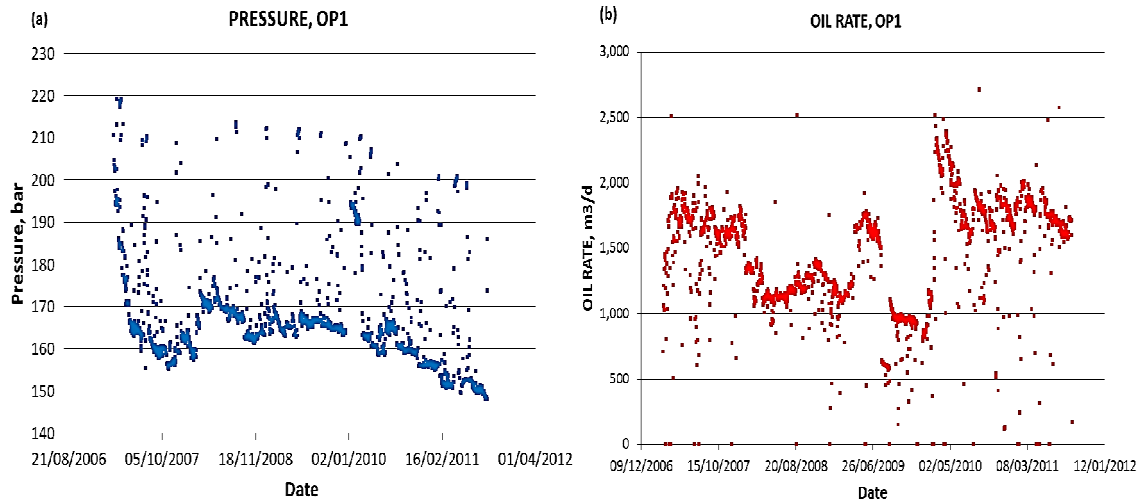
Figure 7 a): Behaviour of the reservoir pressure with time for producer OP1. **b):** Pattern of fluid oil flow rate from T0 to T1 for producer OP1.

Overall inspection of Fig 7 reveals a gradual decrease in the reservoir pressure with time (fig 7a) and a relative increase in the flow rate with time (fig 7b); sharp changes are seen on the plots above, when the wells were shut-down/open.

A small but noticeable inverse relationship between the reservoir pressure and the oil flow rate was observed at the wells (*see appendices E.3 & E.4*), this is because as the reservoir is depleted, its primary drive mechanism decreases (for the time of investigation the drive mechanism was identified to be a combination of water drive, gas drive and solution gas drive).

Pressure maps

The average pressure data estimated using equation (2-3) and field data was sampled into the 3D static model to take advantage of the geostatistical tools incorporated on Petrel. This process was used to produce a spatial distribution of the pressure based on values at well location. The process of sampling pressure was as follow:

I. Following calculation of average pressures, the pressure values corresponding to T0 and T1 were extracted.

34

II. Pressure values at T0 and T1 were used to build synthetic logs with the same coordinates of the production wells.

III. The synthetic logs were upscaled and the pressure was modelled in a similar fashion to other reservoir parameters using stochastic modelling techniques.
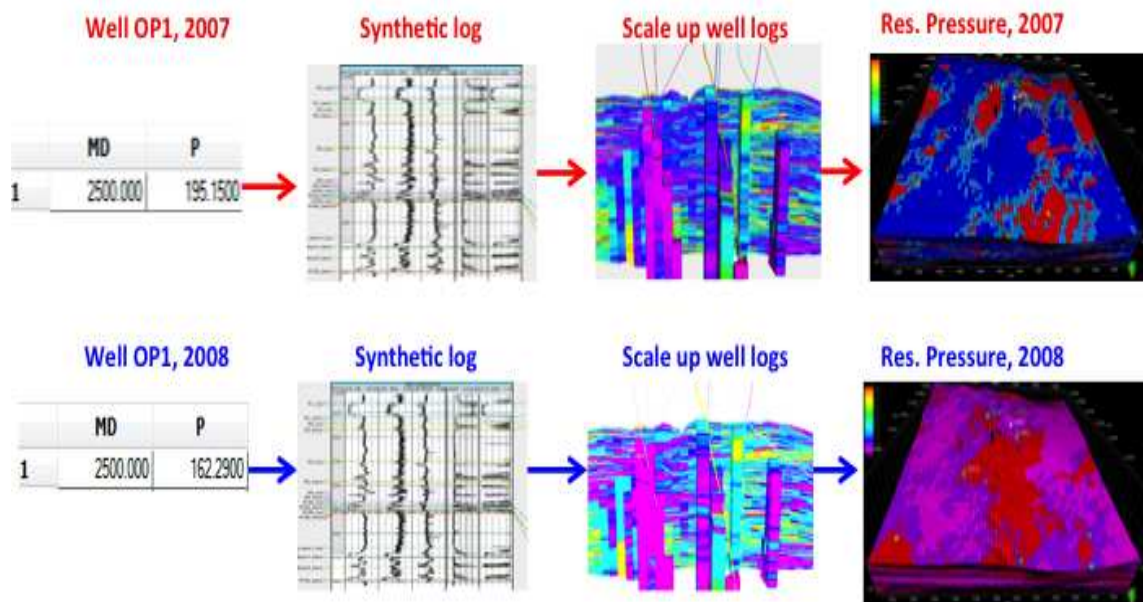
Figure 8: Schematic representation of the steps involved on the modelling of the reservoir pressure.

Fig 8 illustrates the main steps involved in the modelling of the average pressure. Once the average pressure was estimated, maps were generated in the 3D domain, and then single layer 2D maps were produced using the statistical arithmetic averaging tool in Petrel. The approach for sampling the pressure (fig 8) became the standardised approach used to sample other reservoir parameters into the model, these parameters included: GOR, saturation, initial permeability, porosity, etc.

Fig 9 shows the average pressure of the reservoir sampled into the 3D model using the workflow illustrated in Fig 8. The pressure ranged from 194-214 bar at *T0* and 160-187.5 at *T1* this reduction in pressure agrees with the information in Fig 7a where the plot shows a decrease in pressure. The difference in average pressure between T0 and T1 was computed to estimate the pressure drop associated with oil depletion, these computed pressure differences *(*fig 10) were used to calibrate 4D signal information. Around oil producers the measured depletion ranges from about 28 to 34 bar (fig 10) this range corresponds to changes in head between 296 to 367 metres a phenomenon that would contribute considerably to gas exsolution.
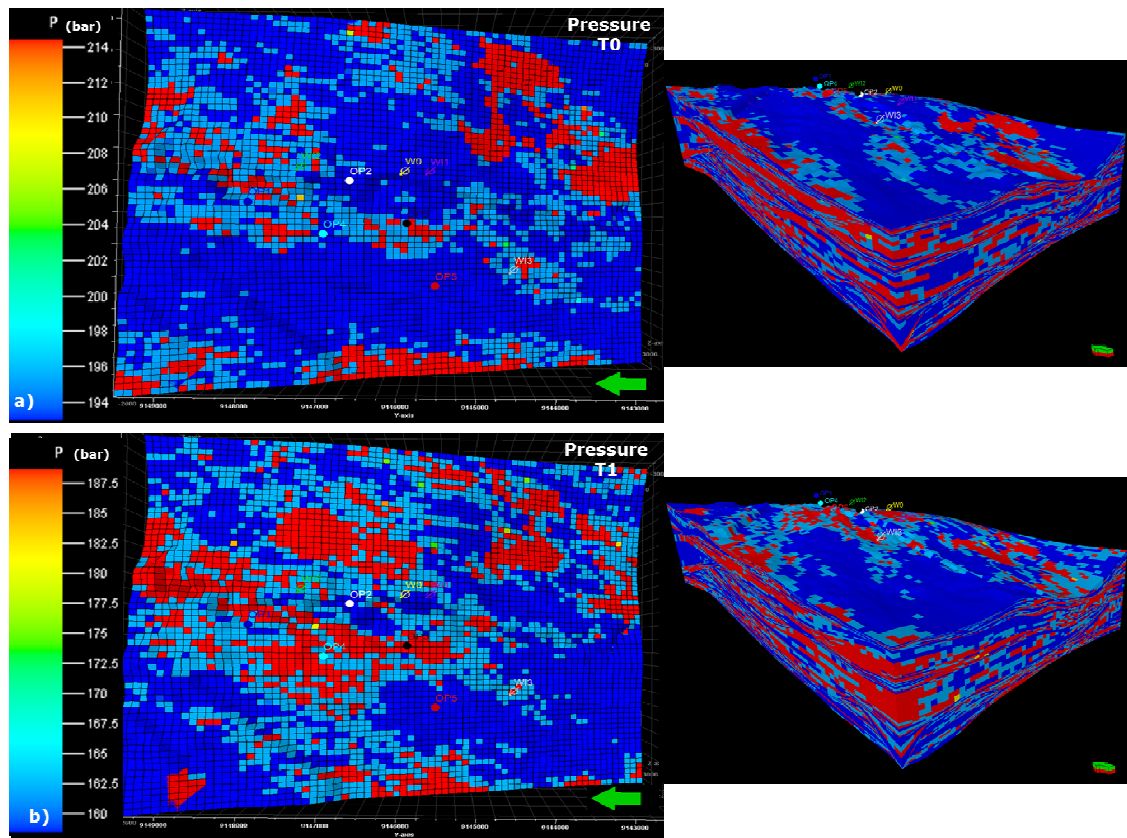
Figure 9: Distribution of the reservoir pressure at different times a**)** T0 and **b)** T1.
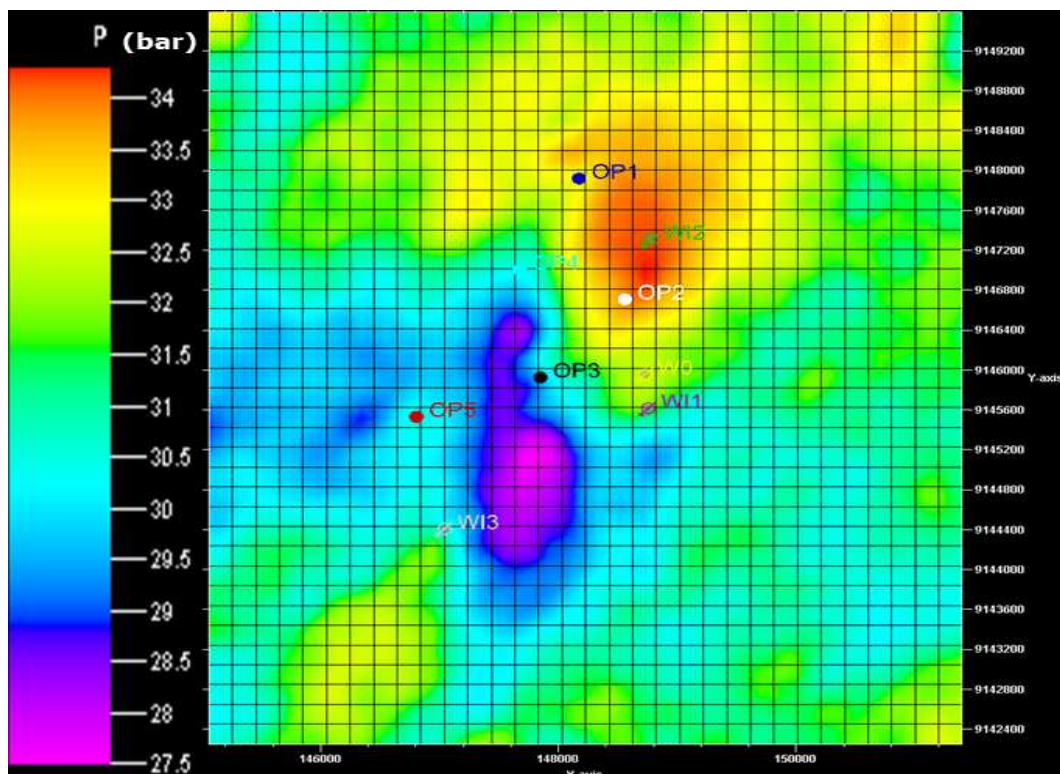
Figure 10: Changes in the reservoir pressure between T0 and T1. The figure suggests that greatest depletion occurred around OP1, OP2 compared to other producers.

2.2 Dalia Reservoir Model

The static 3D reservoir model of the Dalia field was built to incorporate and visualise all the characteristics of the reservoir relevant to its ability to store and produce hydrocarbons. The model is also the tool used to extract the numerical data necessary to estimate the horizontal permeability using the approach here developed. Building the model followed careful consideration of the input parameters necessary for the numerical approach through planning and careful review of the best model building practices.

2.2.1 Model workflow

The model workflow for the 3D model started with optimization of field data for integration into Petrel. Here data files with horizon information, check shot surveys, well tops, and well trajectories were formatted to Petrel import specifications. The formatted data was then imported into Petrel (seismic, well data, average pressure, well rate, GOR, well derived permeability, etc.). Following seismic interpretation, the 3D grid was defined using the pillar gridding tool and 100x100x100 grid cells. The generation of surfaces, definition of the zone model up to the petrophysical modelling followed the 3D grid generation and through petrophysical modelling, relevant properties were modelled in the 3D domain. By using surface operations, average maps of parameters/properties were generated, these average maps were created through arithmetic averaging the properties thought the modelling process. Numerical data from the average maps became the input data for the computer models used to estimate the horizontal permeability. *Table 14* on the *appendix E.2* contains a summary of the model information (model size, input parameters, grid cell dimensions, input wells, and input parameters).

The workflow here described does not focus on the individual steps taken to build the model but on the overall approach to extract quantitative data from the model. The steps of the 3D model building process included:

1. *Data import:* Seismic data, wells, wellheads, well tops, horizon data, etc.
2. *Geophysical interpretation*: Seismic interpretation, seismic track, make horizons and attribute extraction.
3. *Corner point gridding:* Definition of the 3D skeleton, generation of surfaces using horizon data, definition of zones and layering of the reservoirs.
4. *Property modelling:* Scaling up of the well logs, property and petrophysical modelling.
5. *Geometrical modelling:* Generation of 3D grid properties such as pressure, saturation, seismic resampling, permeability and rate. Mathematical

37

estimation of difference in the properties for the two dates of the seismic analysis (i.e.: ΔP, ΔGOR, ΔA, etc.).

6. *Average maps and Data export:* Generation of average 2D images by averaging properties from the 3D model and exporting numerical data (matrices) from these 2D average maps.
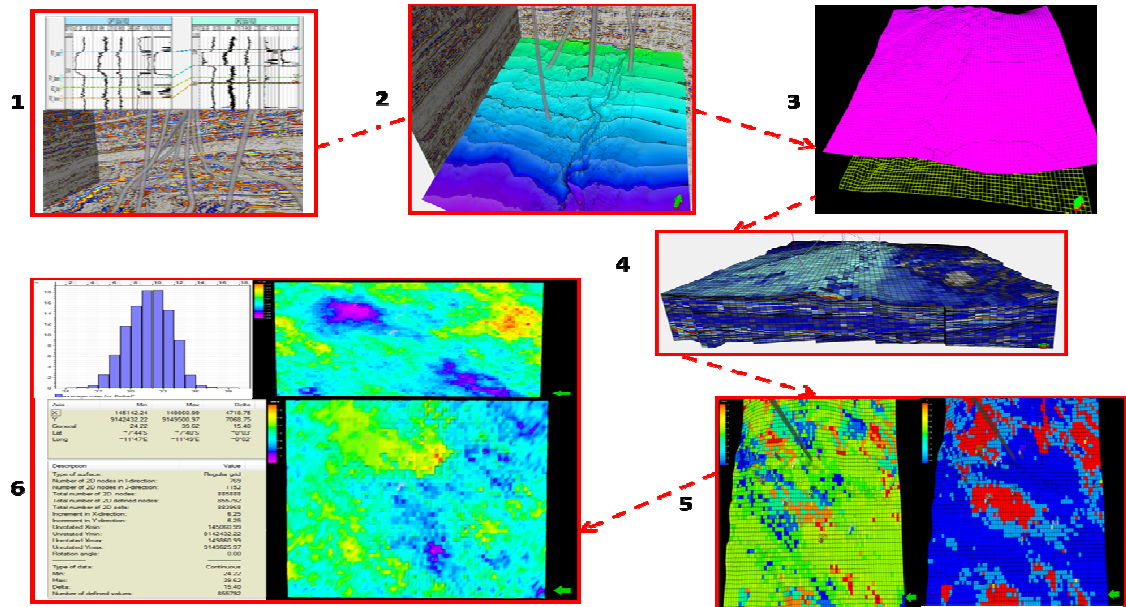
Figure 11: Workflow of the Dalia 3D model bluidnging process, showing the natrure on information extracted from each phase of the model.

Some of the main reasons behind building the 3D reservoir model of the Dalia field include:

- To allow a 3-D analysis and visualization of all the parameters, tests, interpretations and data from various sources
- To integrate all the geological and sedimentological knowledge from the field by aggregating data from numerous sources
- To provide better understanding of Dalia reservoir geometry, dependant on the input data.
- To help managing all the field data
- To generate interwell data and populate it across the reservoir through geostatistical tools in Petrel
- To extract numerical data from the 2D average maps

2D average images were used for the numerical approach due to robustness, computational efficiency and relative accuracy, 2D heterogeneous formulation are relatively easier to implement in terms of computer codes compared to the 3D formulations. However, the arithmetic averaging approach through which 2D

images were generated potentially adds uncertainty to the results as the true vertical distribution of the properties mapped are not considered as such local highs and lows are not considered, in other words, the number of parameters would be the same as that for a smoothly heterogeneous medium without discontinuities.

The most important steps included the extraction of numerical data from the model and the ability to estimate interwell data populating it across the field though geostatistics. Nevertheless, reservoir modelling and characterization intended to describe different reservoir features by maximizing the use of all the available data to produce realistic reservoir descriptions (honouring the underlying geology). Reservoir characterization was performed and the features described comprise petrophysical properties such as permeability and saturation as well as important parameters/properties such as porosity, GOR, flow rate, pressure, etc. The picture bellow illustrates the workflow used for the reservoir description mainly based on stratigraphic information from seismic.
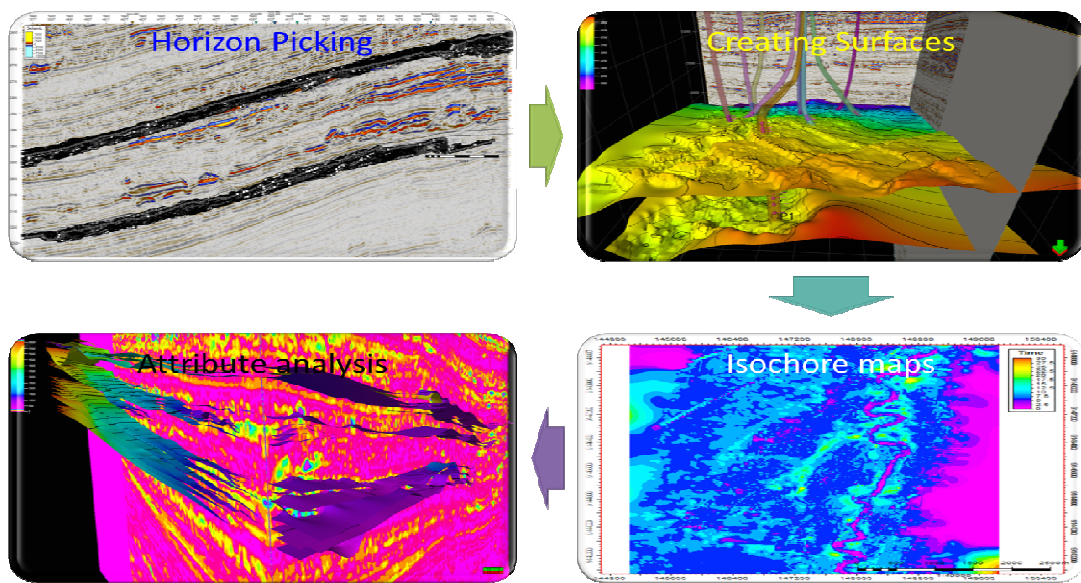
Figure 12: Workflow for the seismic interpretation from which stratigraphic interpretations were derived.

For the seismic interpretation, the reservoir surfaces were picked once the polarity of the reflections was established, based on the reflection of the seabed using a combination of structure related features, high amplitude reflections and trapping information. Surfaces were created using horizon data interpreted from seismic; these surfaces were then used to the create sediment thickness maps and isoproportional slices between surfaces. Seismic attributes were used to enhance information that might be subtle in conventional seismic, leading to a better

understanding and interpretation of the data. The attributes were also used to extract quantitative property information from the seismic volumes based on analysis of the signal shape.

Effective reservoir simulation resulted from a multidisciplinary interaction between various subjects anticipated to contribute data to the final reservoir model (fig 1); however, the interpretations here presented represent as reflection of the available data, and its quality. Special attention was paid to the quality of the data prioritising certain types of data based on the uncertainty attached. Core data or core derived interpretations (PVT) were considered the most important piece of data because being a physical evidence of the reservoir, greater weight had to be given to it; despite the fact that the reliability of core derived interpretations can be affected by the way it is prepared or handled from site of collection up the site of measurements, core properties are regarded as more reliable because they represent direct reservoir measurements performed without any transforms or assumptions (Djebbar & Donaldson, 2003).

Fig 57-H (appendix *H*) shows the distribution and number wells used by the project. The data used by the project, utm coordinates of the wells and number of layers of the model are summarized on *Table 13* while the model, grid size and information of the parameters used by the project is summarized in *Table 14.*

2.2.2   **Stochastic modelling**

The Dalia 3D model was built for prediction of the spatial and temporal variation of the reservoir properties such as porosity, facies proportions, saturation permeability, etc. Given the degree of heterogeneity of the Dalia Field, without an adequate choice of stochastic algorithm it would not be possible fully describe any single reservoir property from one or a set of measurements of a single property at one given time or location.

A probabilistic approach was chosen to calculate multiple deterministic realizations used for characterizing the distribution of reservoir and petrophysical properties from the Dalia Field using data from the well logs, seismic, spatial correlations and probabilistic distribution of the properties to relevant to the study. The spatial distribution obtained through stochastic analysis is regarded as an approximation of the actual properties (Kellkar & Perez, 2002); an alternative to using stochastic approach would be deterministic one; taking this course would however require assessment of uncertainty for which the available data was not sufficient.

Using a dataset comprised by seismic and production data, most of the interwell space was estimated from nearby wells through stochastic modelling, an approach based on statistical methods. Geostatistics was used to generate multiple realistic 3-D realizations of the relevant reservoir parameters to be characterized together with the distributions of their heterogeneities.

Input data for the mathematical and numerical models was extracted from the 3D model, the model in turn used geostatistics to populate the inter-well data; therefore, understanding the distribution of this data across the field was important to establish a link between the computer models and the 3D reservoir models. The choice of the geostatistical methods was constrained by the input data and results produced, that is, the stochastic method should effectively fill the interwell spacing while honouring the real data. Realizations of distributions using different stochastic methods were produced to determine the most suitable stochastic approach (fig 13).

Using the limited data points sampled from the wells, statistical information was extracted from the production data following approaches proposed by Kellkar & Perez, (2002; Benerjee, et al., (2004); Clark, (1979); Cressie, (1993); Strebelle & Jounel, (2001). The algorithms used by the project to perform petrophysical and property modelling comprised a combination of *Sequential Gaussian Simulation* (SGS) and *Multi-Point Statistics* (MPS), both Monte Carlo Simulation based approaches. Consideration was given to other algorithms such as *Gaussian random simulation, Kriging interpolation, Kriging and Kriging by Gslib* (Schlumberger, 2009*),* however results produced by these did not meet the requirements of the project neither honoured the real data as closely as the combination of SGS and MPS approaches (fig 13*).*

The figure bellow illustrated the difference in results when different stochastic approaches are used, Fig 13a shows a distribution of water saturation using Sequential Gaussian Simulation algorithm while Fig 13b shows the distribution of the same property using the Krigging stochastic algorithm; from the figure, it can clearly be seen that SGS algorithm produces a more realistic distribution of the saturation (water saturation relatively higher at greater depth) as opposed to the Krigging which produces anomalous distribution of the property where the water saturation is unusually low across the whole field.
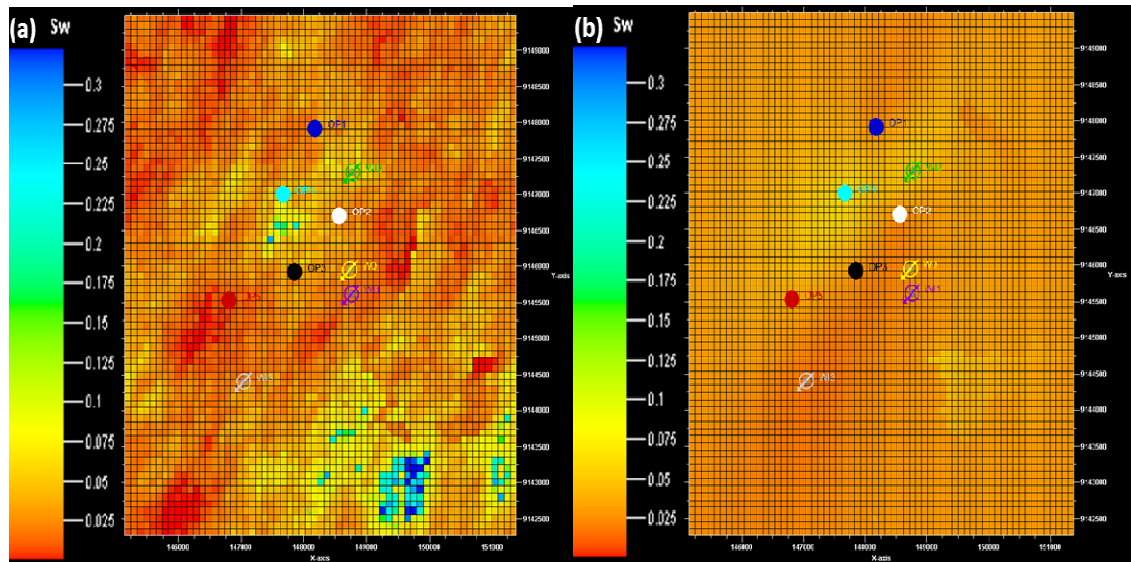
Figure 13: Comparison between water saturation distribution using different stochastic approaches a**):** SGS algorithm and **b):** Kriging algorithm.

Sequential Gaussian Simulation stochastic algorithm used to populate the geomodel using continuous data while honouring well data, input distribution, variograms and trends (Schlumberger, 2009). Local variations of the data (even data away from the wells) were created by the variograms and distributions; the type of variogram used to model the properties and its details can be seen in Fig 65-H (*appendix H)*. For inspection of uncertainty, multiple representations of the properties were produced, the final model however used a random seed number to produce the stochastic simulations.

Multi-Point Statistics this modelling technique was used to integrate geological information to the model through training images (Strebelle & Jounel, 2001). Training images can be used to imitate stationary physical and structural reality of reservoirs (Strebelle, 2002). Replacing the two-point statistic variogram with information obtained from training images allowed the modelling of nonlinear facies, geobody shapes such as sinuous channels, as well as capturing complex spatial relationships between multiple facies. The training images were generated by using geobody algorithms with more defined shapes, easily definable by measurement and less limited by conditioning data. The training images were created using horizon probes that used geological, surface information and seismic data, through manipulation of the opacity setting and volume rendering process the high amplitudes of the seismic data where made partly opaque, the crossover amplitudes partly transparent, and hidden structural or depositional identifiable.

Statistical information obtained from the training images generated through MPS was populated into the 3D model by attaching this information to the seismic and

42

well data using Sequential Gaussian Simulation algorithms. The training images were then used to define the major trends in (azimuth) orientation of the major horizontal direction.
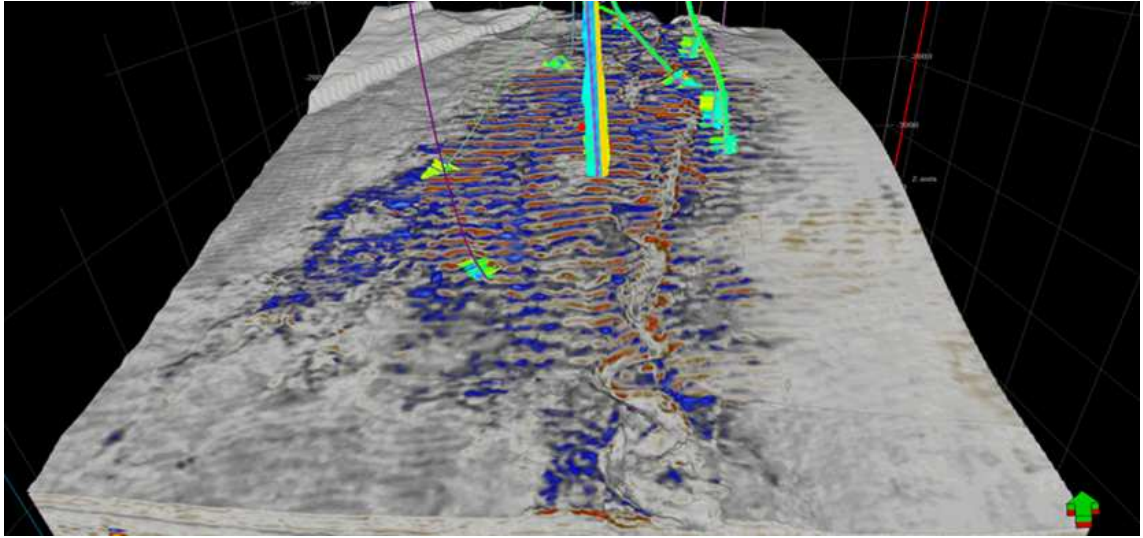
Figure 14: Geobody extracted using seismic and surface information calibrated by well data. Through MPS training images from the geobody were created and used to estimate the anisotropy range and orientation of the petrophysical properties. The N-S direction of was then used as do define the azimuth of the properties (green arrow points north).

The geological structures in the model were characterized using combination of both modelling techniques (SGS and MPS) through which data variability was expressed in more than two locations at time while honouring the input data. The use of a random seed in the SGS produced results with some random aspects and the uncertainty associated with this was characterized by producing equally probable realizations of a similar property.
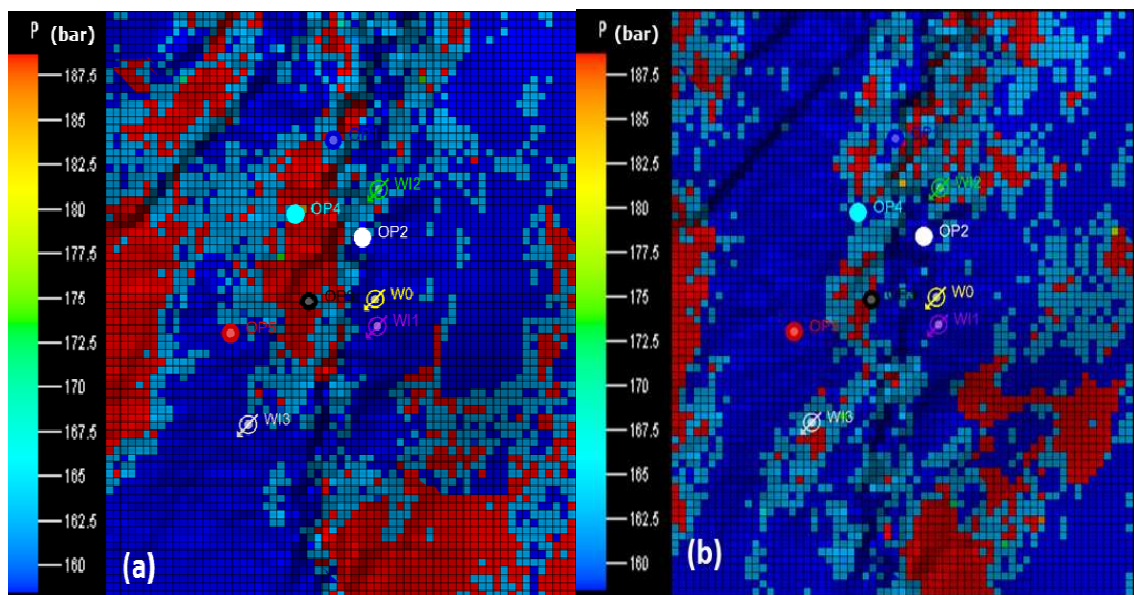
Figure 15: Equally probable stochastic realizations of the up-scaled reservoir pressure at *T2* introduced into the geocelular model using SGS with different seed number **a):** Seed number 12173 **b)** Seed number 24346

The picture above shows equiprobable realizations of the average pressure; the scale shows that maximum and minimum values do not change, however the distribution of the parameter across the field is completely different from one scenario to another. A random seed is a number or vector used to initialise a pseudorandom number generator; using a seed number of 12173 (fig 15a) produced completely different distribution of the same parameter when compared to the channel-like pattern obtained with a number of 24346 (fig 15b). Statistical analysis of the distributions in the figure above provides means of assessing the range of uncertainty.

2.3   Property modelling

Property modelling consisted in filling the cells of the grid with discrete continuous petrophysical properties. The number of layers of the 3D grid (*table 13*) is reflective of the reservoir geometry defined by the seismic interpretation where horizons, surfaces, isochores and other seismic derived features played an important role in defining the model skeleton (fig 58-Hb). The processes involved in the property modelling include:

Geometrical modelling: process where relevant properties of the model were built based on the geometrical properties of the actual grid cells (i.e.: cell volume, angle, height, etc). Most of the parameters had to be introduced into the model by sampling techniques (i.e.: seismic resampling was used to input seismic attributes into the grid).

Scale up well logs: Process by which values from the well logs, well attributes and synthetic well logs were sampled into the grid for posterior use in geometrical and petrophysical modelling.
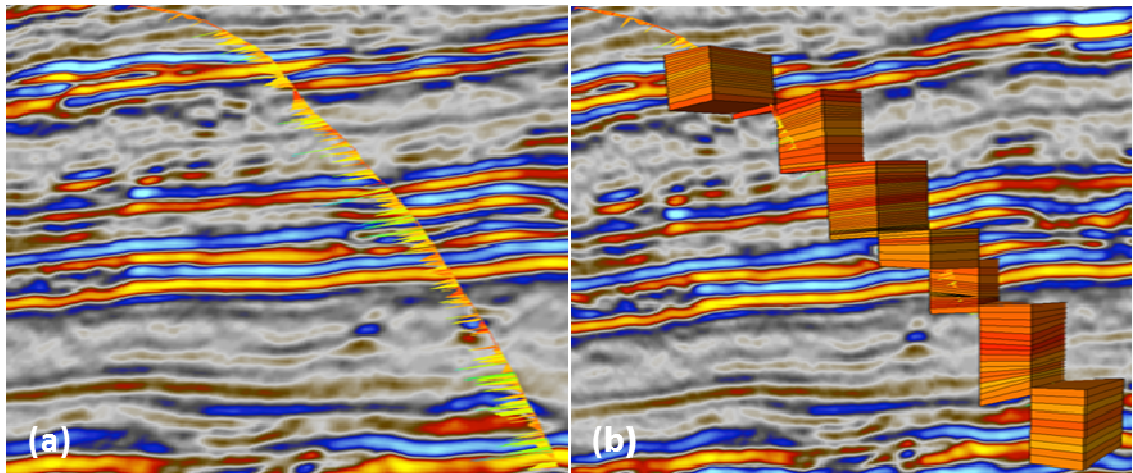
Figure 16: a): OP1 synthetic well of water saturation **b):** Upscaled synthetic log of water saturation at producer OP1.

Data analysis: This process consisted of preparing the upscaled log data for property modelling. The data was prepared by applying transforms to the input data, identification of trends for continuous data, vertical proportions and probability for discrete data obtained from training images. To ensure that similar trends of the data appear in the grid variogram for describing the data were defined based on training images created through MPS.

Pattern correlation: The neighbouring relationship between the properties was incorporated by introduction of secondary variables/properties (co-kriging). Through pattern correlation, the simulation of one property was steered using a spatial distribution of a secondary variable. Water saturation was used as the conditioning property (secondary variable) during pattern correlation because it was calculated directly from the well log data.

For a complete reservoir characterization, the spatial distribution of different rock properties was obtained; these are simply images of the most relevant rock properties used to build the reservoir model and perform the reservoir characterization.

At the well location, estimation of the most relevant parameters used standard geological and reservoir engineering techniques. The actual distribution of the estimated values followed a careful stochastic approach depicted in section 2.2.2. Synthetic wells of the properties were generated and afterwards upscaled and combined with appropriate stochastic technique were used for spatial distribution of the properties needed by the numerical model.

The approach used to estimate the most important reservoir properties is outlined in the sections that follow.

2.3.1　Water saturation

Using the available well log data, saturation was calculated based on the relationship between rock resistivity and fluid resistivity using the Archie's equation in the form:

$$S_w = \left(\frac{R_w}{R_t \phi^m} \right)^{1/n}$$
(2-4)

where

S_w = the water to be estimated

R_w = the original resistivity at 100% water saturation

R_t = the true resistivity

n = saturation exponent

m = cementation factor

$\emptyset$ = effective porosity

The saturation curve was derived from relationships established between resistivity, porosity and water saturation within the reservoir and water leg. Comparison of these relationships with capillary data can be used for characterization of the uncertainty:

in the water leg: $R_o = R_w \times \phi^{-m}$

in the oil leg: $R_o = R_w \times \phi^{-m} \times S_w^{-n}$

where R_o is the resistivity of the rock

Conventional techniques for estimation of n and m parameters consists of using Pickett plots to estimate Rw by plotting porosity vs true resistivity, however, these technique produced un-satisfactory results which were not used due to lack of saturation data to compare. For the purpose of uncertainty characterization the table below shows the m and n values used by the project to estimate the initial

saturation model.

Table 7: Selection from the industry standard values of the petrophysical parameters used to estimate the water saturation.

Parameter	Case 1	Case 2	Case 3
m	1.7	2	3.2
n	1.3	2	2.6
Rt	log	log	log
Rw	0.29	0.29	0.29
Ø	log	log	log

The initial water saturation was estimated using well log data, equation *(2-1)* and parameters on Table 7; using property modelling tool on Petrel, the spatial distribution of the property for the 3 scenarios was obtained (figs 17a to 17c).

Water saturation distribution and estimates generated by the model differ between the 3D and a 2D (the average map) domain, such differences are illustrated on *Table 8*; the information on the table represents the numerical data extracted from Figs 17a to 17c, such information was used for uncertainty analysis to determine the most likely scenario for the initial saturation by comparing results in (figs 17a to 17c) with water production and fractional flow data. Case 3 was chosen for parameters *m* and *n* based on analysis of the results in (figs 17a to 17c).
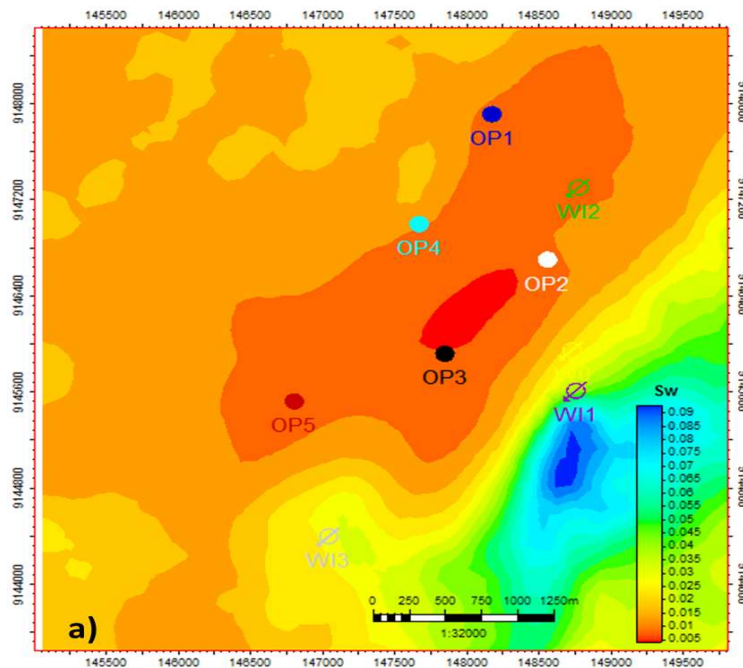
Figure 17: a) Saturation map (2D) generated using petrophysical parameters m=1.7 and n=1.3.
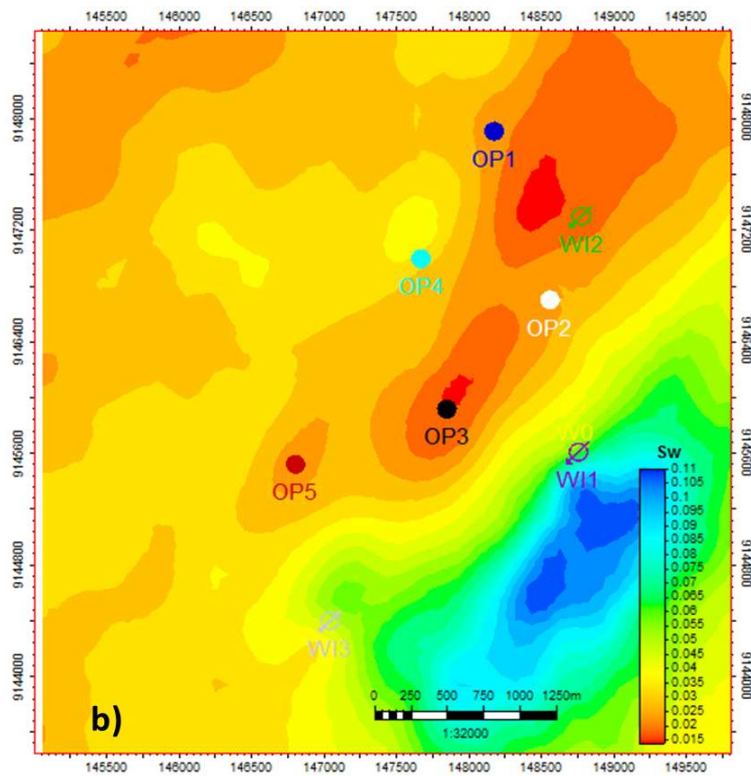
Figure 17: b) Saturation map (2D domain) generated using petrophysical parameters m=n=2
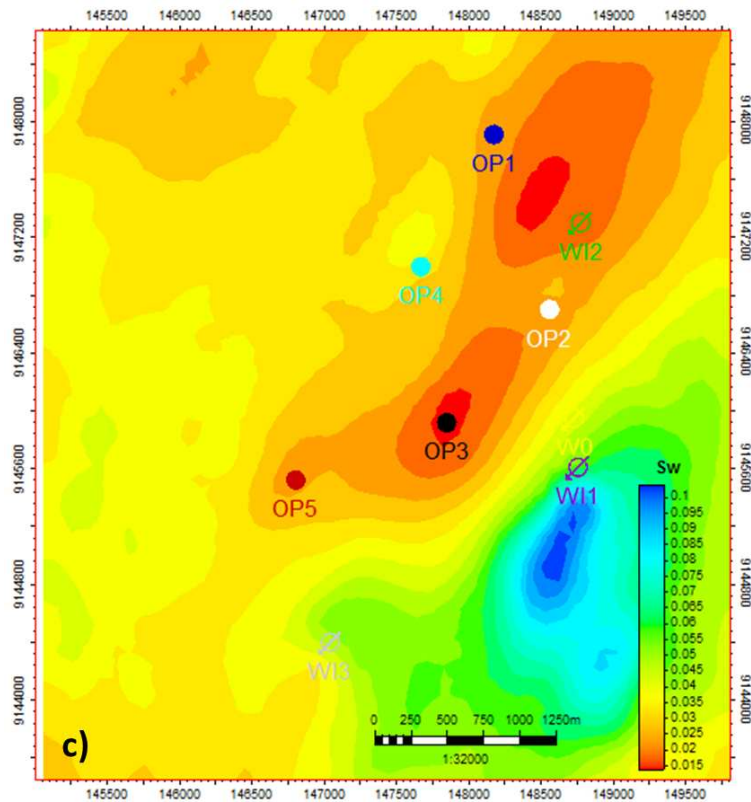
Figure 17: c) Saturation map (2D domain) generated using petrophysical parameters m= 3.2 and n=2.6.

Fig 18 shows the distribution of the saturation estimated using the parameters for case 3, the figure shows a general low water saturation being the highest values in the southern part of the field, this information is consistent with the fact that water production started after *T1* and fractional flow data shows very little amount of water being produced.
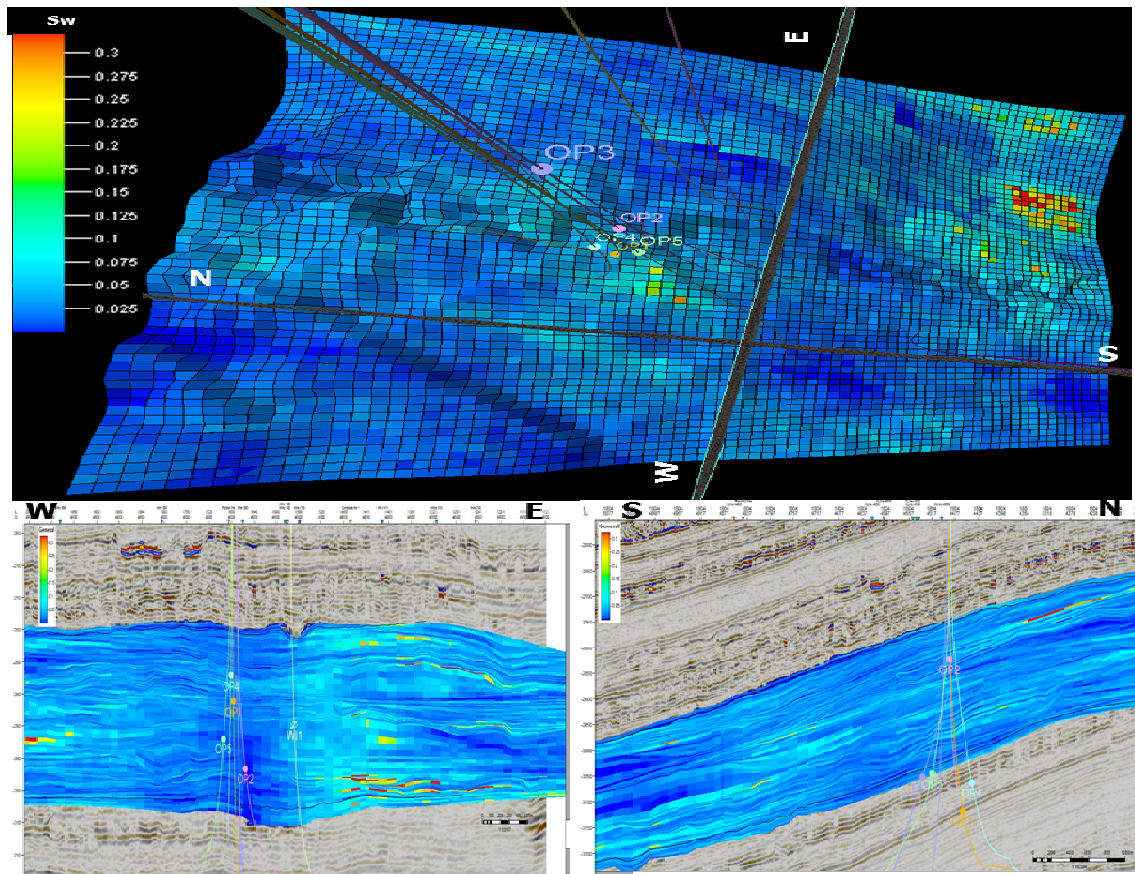
Figure 18: Saturation distribution at *T0* showing considerably low saturation values. Saturation is highest in the aquifer region (southern part of the field) and around injector WI1

2.3.2   Permeability

The numerical model needed an initial permeability model to be updated by the approach that considers time-lapse 4D seismic and production data, for this reason an initial permeability map that best honours the field data had to be produced. The complexity of the permeability function and challenges establishing a general relationship with other parameters turned the permeability into one of the most difficult parameters to estimate and predict.

Scientists have dedicated a great deal of time and work into developing predicting models for permeability (Wyllie & Rose, 1950; Ahmed, et al., 1989; MacBeth & Al-

Maskeri, 2006). The project made use of the existing empirical models based on the relationship between irreducible water saturation, porosity to estimate permeability (Coates & Dumanoir, 1974; Timur, 1968; Tixier, 1949). For the purpose of uncertainty characterization, three approaches were considered for estimation of the initial permeability, inspection of the results produced by each model allowed the selection of *the best, most likely and worst* case scenario. While exploring different possibilities and comparison of results, the approach allowed minimization of uncertainty therefore maximizing the confidence interval of the initial permeability results.

The theoretical models used to estimate the initial permeability are:

Timur, 1968 – This model relates measurable rock properties with permeability following work done by (Kozeny, 1927) and (Wyllie & Rose, 1950). The Timur model used the equation in the form:

$$K = 8.581 \frac{\phi^{4.4}}{S_{wi}^2} \tag{2-5}$$

where

K is the estimated permeability (miliDarcies)

ϕ is the effective porosity from log

S_{wi} is the irreducible water saturation from log

Coates, 1981 - this empirical technique estimates permeability (in Darcies) following an approach proposed by Coates & Dumanoir, (1974), in the form:

$$K^{\frac{1}{2}} = 100 \frac{\phi^2 (1 - S_{wi})}{S_{wi}^2} \tag{2-6}$$

Tixier, 1949 - derived on a relationship between resistivity, water saturation and capillary pressure, Tixier, (1949) proposed the model for determining permeability (in Darcies) from resistivity gradient following work of Wyllie & Rose, (1950). The model takes the form:

$$K^{\frac{1}{2}} = 250 \frac{\phi^3}{S_{wi}} \tag{2-7}$$

Results produced by each method are very different, and the decision as to which model is the more adequate was based on comparison of the permeability values

from Dalia field reports and published data (*table 3*). Fig 19 shows the distribution of the permeability across the Dalia field for each of the theoretical models used.
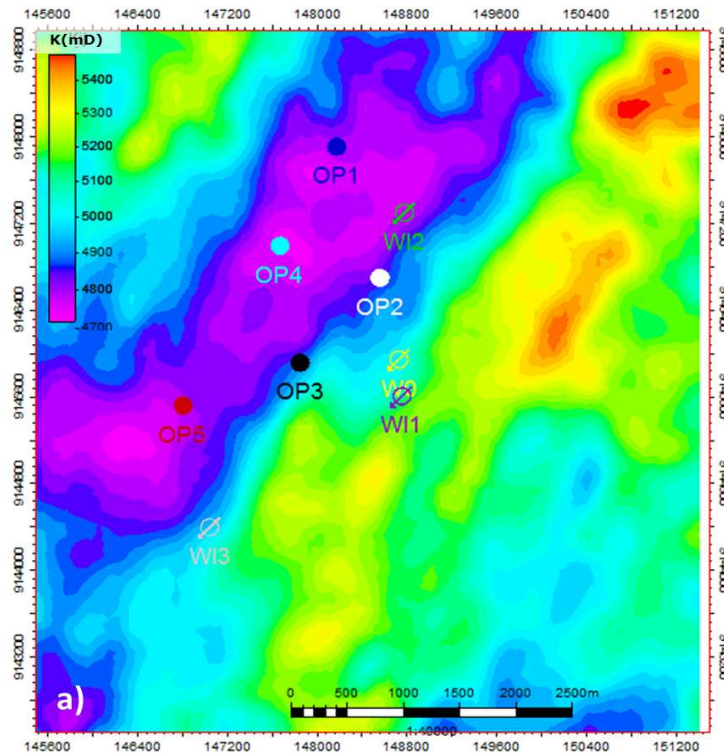
Figure 19: a) Initial permeability 2D map generated using Timur approach.
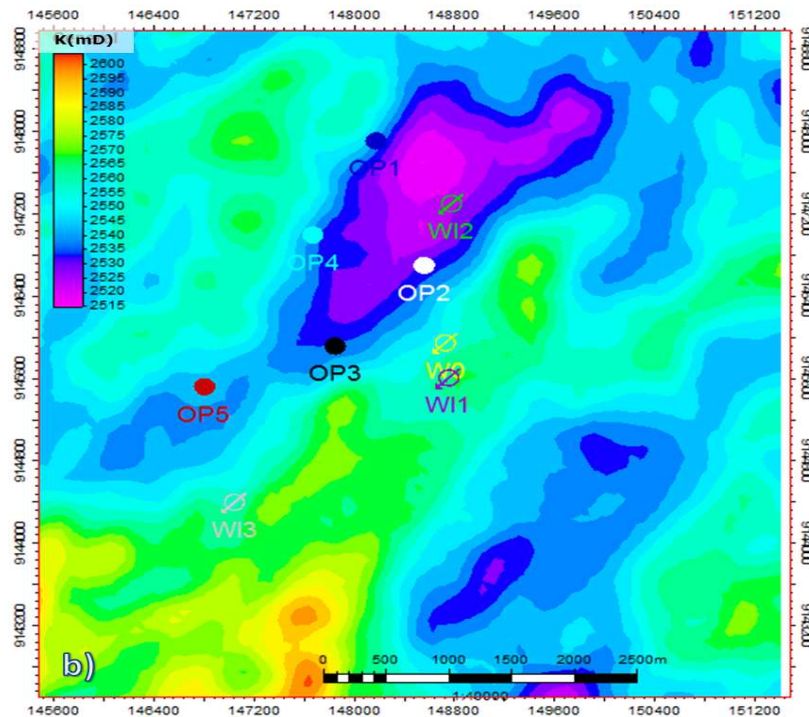
Figure 19: b) Initial permeability 2D map generated using Coates model.
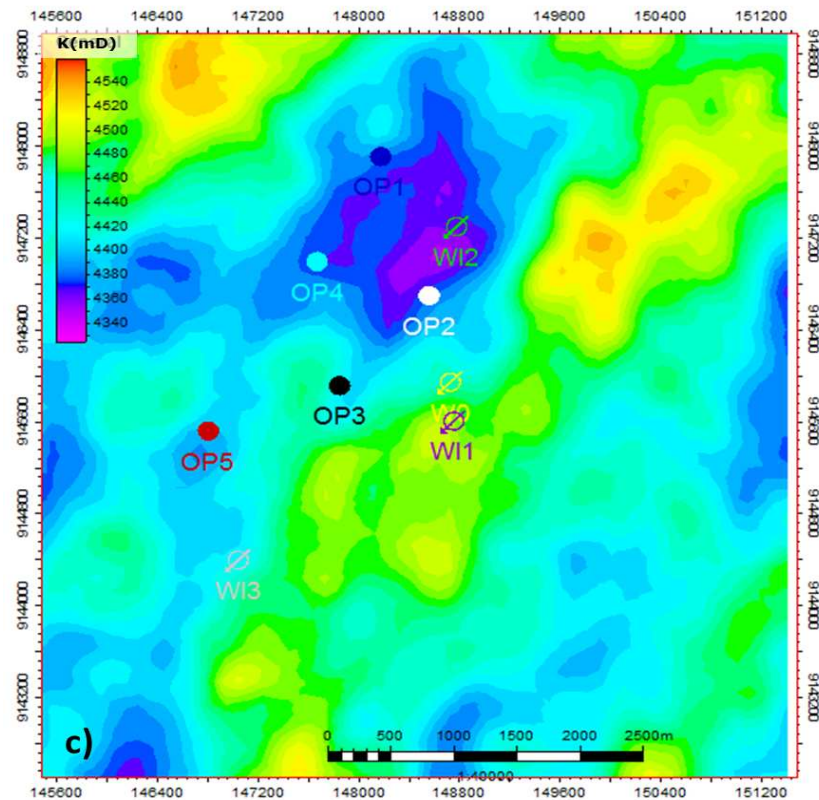
Figure 19: Different initial permeability maps generated using different estimation techniques that relate resistivity, saturation and porosity from well log data. The permeability shows a pattern that reflects the pattern of the meandering channel **c)** Distribution of permeability using the approach proposed by Tixier.

The permeability distribution and estimates generated by the model differ between the 3D and 2D (the average map) domains. The difference in permeability values shown in Figs 19a, 19b & 19c is extremely high this because the averaging methods with which the maps have been generated and because the equations used to generate these maps are strictly empirical despite implicitly using physics relations between grain size and irreducible water saturation. Ideally the results produced by these equations should be calibrated using core data, in its absence the results produced by each method were compared to existing literature and reported field data.

The information in *Table 9* is numerical permeability data, these differences have a considerable impact in the uncertainty of the numerical approach as such analysis of these differences is crucial for uncertainty analysis. The project chose the Timur theoretical model to estimate the initial permeability because it produced the smallest deviation from the field reported and published values. The Figure 20 shows the distribution of the initial permeability (3D) using the Timur approach.

According to Fig 20, the permeability ranges 3500-5750 mD, however Dalia Field reports indicate permeability ranging 3000-6000 mD; the uncertainty between the permeability estimated by the model and the field reports ranges -2% to 8%, and this range was considered acceptable.
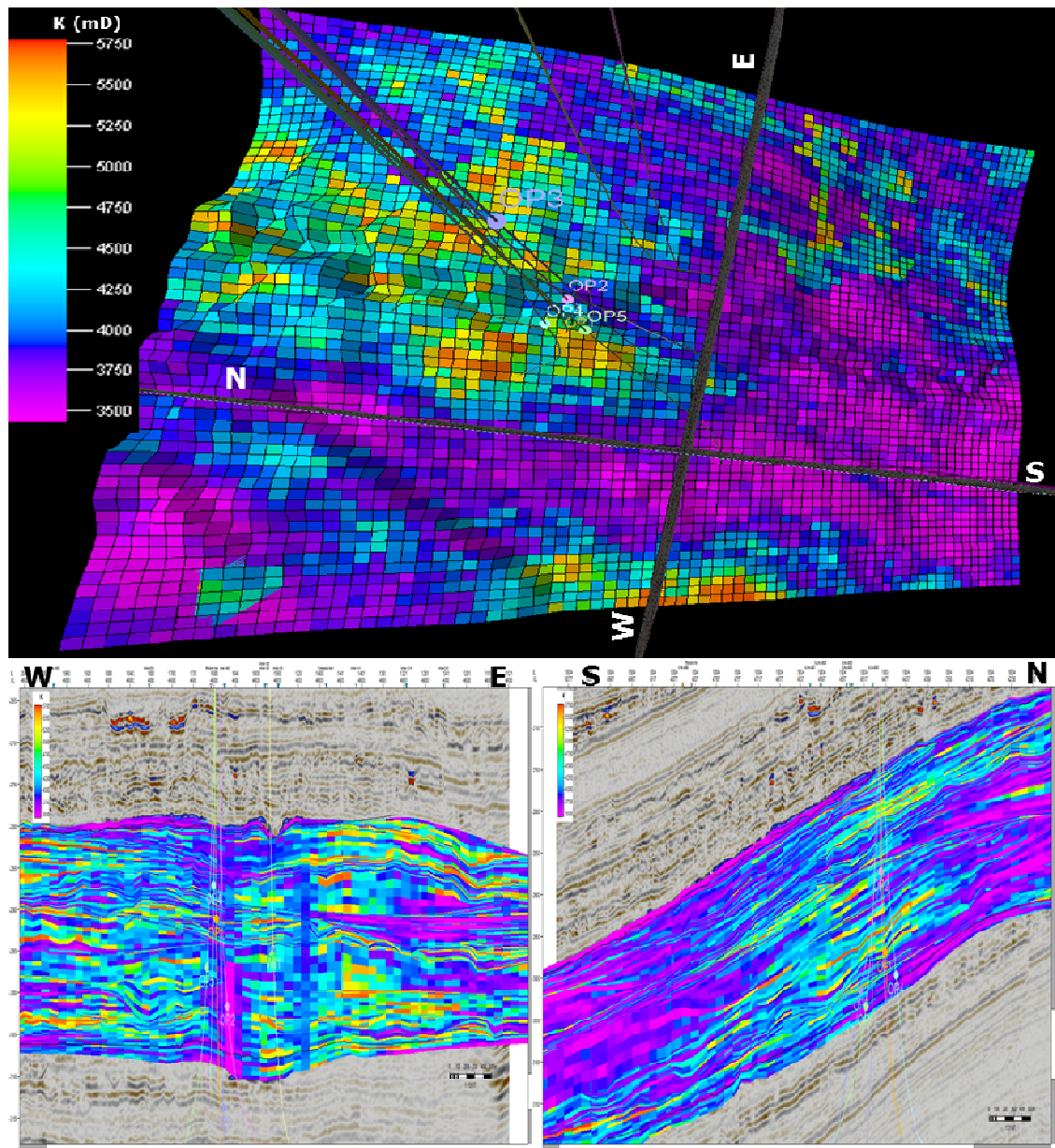
Figure 20: Distribution of the initial permeability in the 3D geocellular model showing higher permeability around the northern/centre part of the field. The cross-sections show good reservoir connectivity between different channel complexes

Fig 20 also shows apparent good reservoir connectivity between the different channel-levee complexes; the connectivity is illustrated by the W-E and S-N cross-sections that show high permeability zones in different complexes that appear to be in communication with each other. Simulated values appear to be in close agreement with permeability values reported by Sonangol E.P (between 3000-6000 mD), however to reduce the uncertainty associated with their estimation, 2D average values of permeability (fig 19a) were used by the numerical approach.

2.4 Reservoir Description

High resolution of the seismic (about 7m vertical resolution, (Prat, et al., 2010)) from the Dalia Field was used to aid reservoir description and characterization of the field. The first step towards building the 3D reservoir model of the Dalia Field was to identify the facies present and map their spatial distribution. Facies interpretation is typically done using the geological information available from well logs, cores and the interpretation of seismic amplitude data (Hanna, et al., 2011). Knowledge of the facies in the area of study results in better application of correlations that are used to generate spatial maps of petrophysical properties (John, et al., 2008). The lack of core data and outcrop analogues imposed difficulties mapping the facies distribution across the Dalia reservoir; these distributions would be used to calibrate the seismic data; furthermore, the absence of a velocity model made it impossible to convert the seismic from time to depth.

The difficulties in identifying facies from the seismic amplitude data and seismic derived structures calibrating these interpretations with localised well-log data. The seismic facies were mapped as groups of seismic reflections with similar characteristics. Because seismic horizons represent an image of the underlying geology (Hanna, et al., 2011), structural maps and detailed geological features were directly obtained from them. The seismic reservoir description approach here presented here intends to provide regional analysis of the sedimentary facies and facies associated with the Dalia Field reservoirs. Considering that the Dalia Field is a producing reservoir, the mapped reservoir layers in the field reports were used (see *tables 10-15*). The focus of the project was to perform a simple stratigraphic study of the field based on reflection data.

Figure 21 shows a N-S distributary meandering channel with a meandering platform and high amplitude overbank deposits, this meandering channel sits on top of the reservoir layer R1. The high amplitude seismic reflections (known as HARs) (Lopez, 2001) seen in yellow/red are interpreted as coarse-grained channel-fill deposits; low amplitude reflections (here termed LAR's), seen in blue/grey are interpreted as silts and muds, these are seen mostly superimposed by HAR's. Channel-avulsion is also seen in Fig 21, where the meandering channels appear to have shifted eastwards. During the avulsion events the flow spread laterally outward depositing the laterally extensive high-amplitude reflection packets (HARPs) (Pirmez, 1994) seen as the red elongated overbank deposits sitting on top of the LARs (figs 21 & 22).
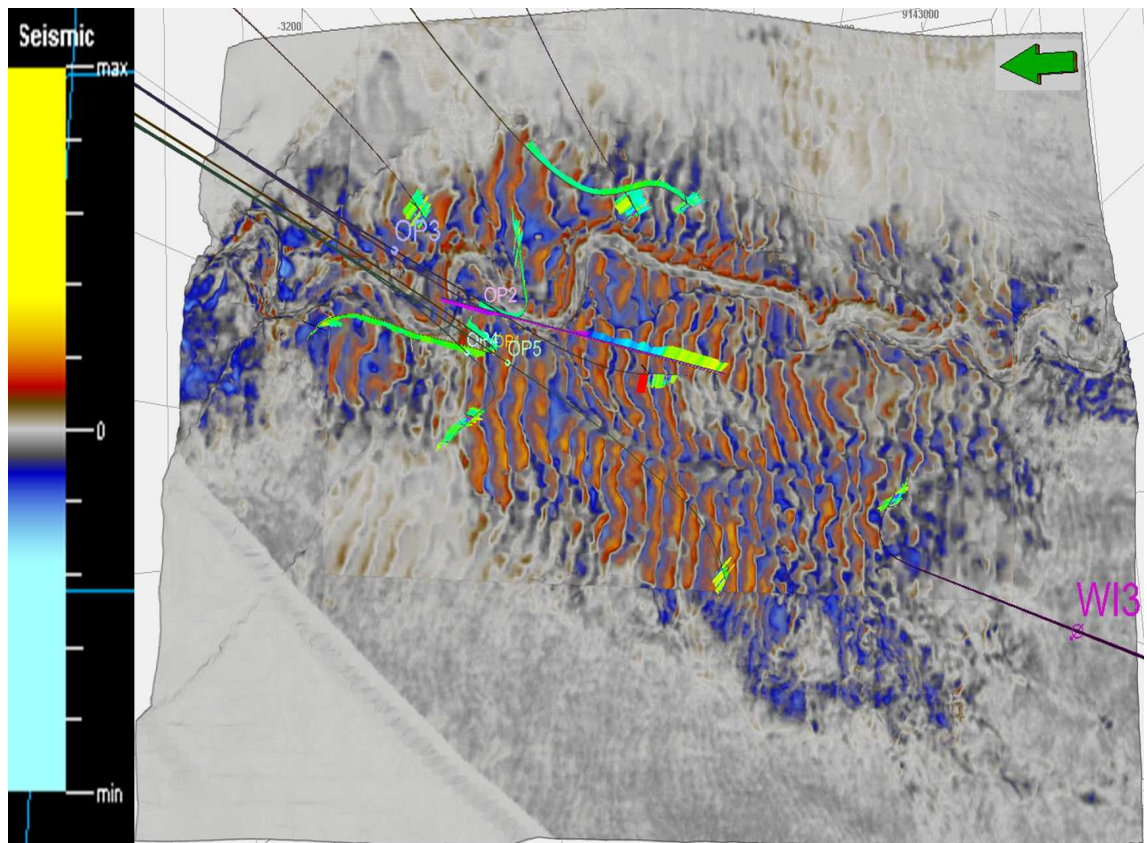
Figure 21: Seismic probe on reservoir layer R1 showing the N-S submarine meandering channel with overbank deposits (green arrow points north).

The Gamma-ray response and the seismic character of the sediments (figs 21 & 22) can be used to infer depositional information that coarse sediments would have been deposited by the river under turbiditic currents where high currents would transport and deposit the channel sands while the fine sediments would have been slowly deposited when the river currents were quiescent. Cross-sections through the reservoir (fig 22) show 4 channel-levee complexes: The Upper, Middle, Lower and Bottom complexes; these complexes were characterised by erosive channels and laterally extended unconfined deposits. The complexes appear to be separated by zero to low amplitude sediments here interpreted as mass-transport deposits (Lopez, 2001).

Stratigraphic interpretations based on the cross-section in Fig 22 show: (1) A thick (~200 m) Upper complex followed by thick semi-structured muds ; (2) A thin (~60 m) Middle complex characterized by flat-lying high amplitude reflectors; (3) a laterally extended thick (~300 m) Lower complex where high amplitude reflectors are interbedded with low amplitude ones, followed by a layer of structureless muds and; (4) a Bottom complex characterized by heterogeneous tilted faulted blocks of sands and muds.
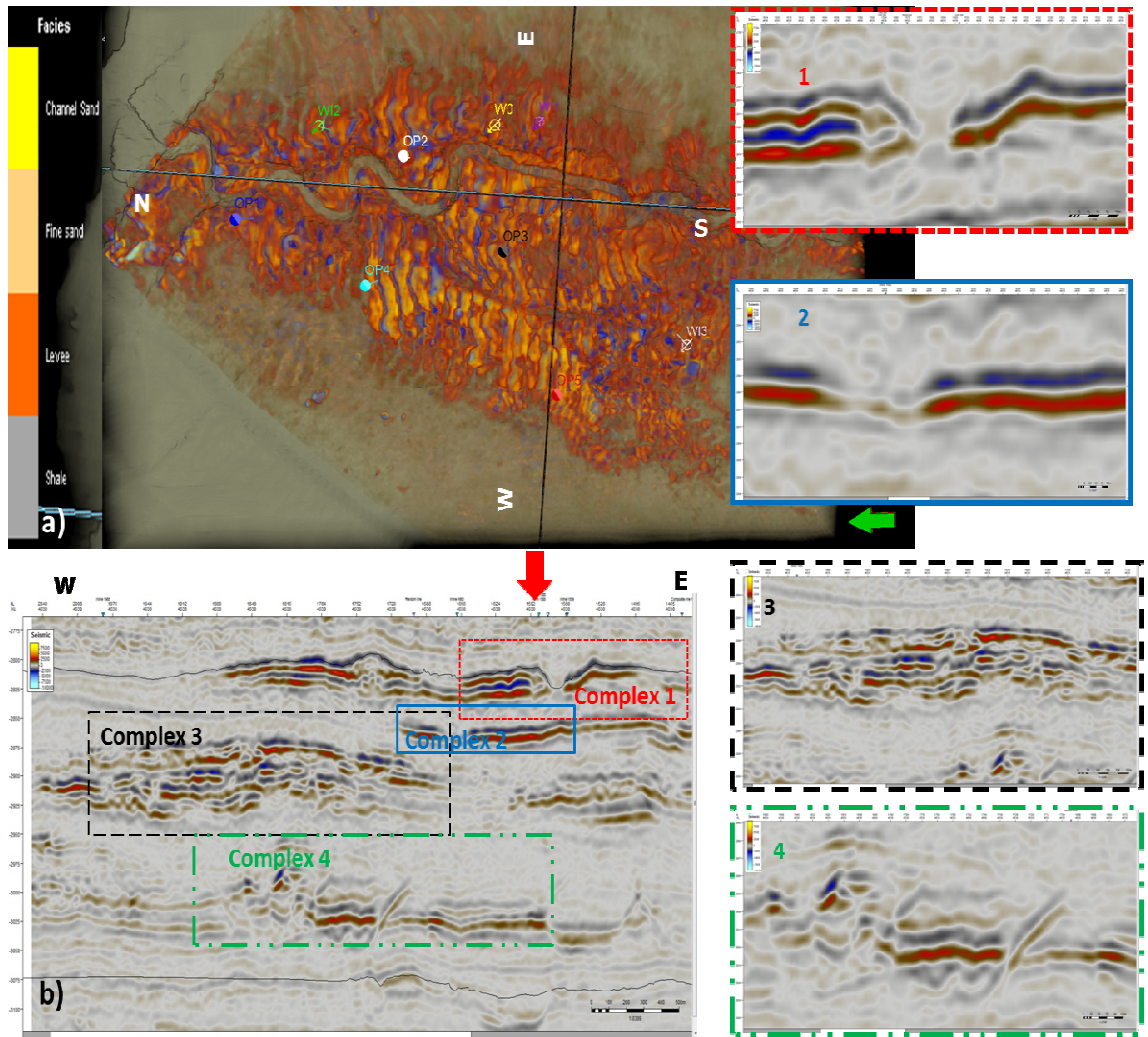
Figure 22: a) Geobody extraction of the uppermost reservoir showing sedimentological information, and N-S and W-E trending intersection. **b)** E-W Cross-section (X-line 4360) showing the seismic character of the interpreted 4 turbiditic complexes.

Palaeo channels in the Dalia Field are laterally extensive and structural comparison with the sedimentological model in Fig 2b (Caie, et al., 2007; Vemba, et al., 2011) allows analogous similarities in terms of sedimentological information in Fig 20a and that in Fig 2.

The reservoir geometry is defined though structural analysis while the petrophysiscal analysis provided information about the spatial distribution of the petrophysiscal properties of the reservoir i.e.: porosity, permeability, and dynamic data such as saturation and pressure.

Reservoir thickness information on (*table 11, appendix E*), was used to access reservoir potential in terms of thickness as: Layer R3 (387 m), R5 (157 m), R10a (108), R1 (62 m), R2 (56 m). Thickness information in terms of penetrated

distance per producer well shows that: OP3 (495 m), OP1 (301 m), OP2 (284 m), OP4 (246 m) and OP5 (28 m).
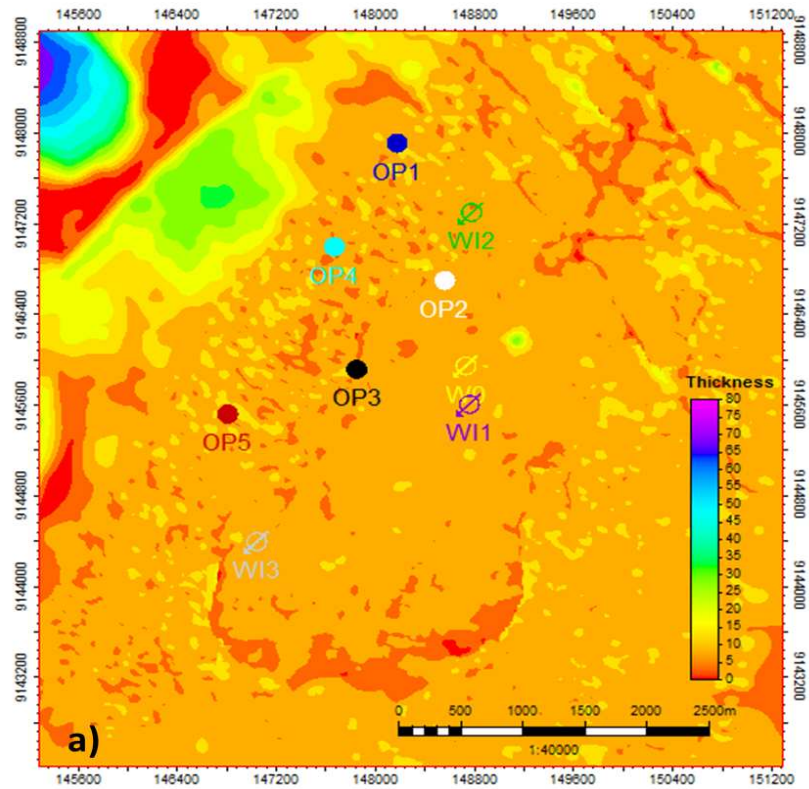
Figure 23: a) Thickness maps (in time) of Reservoir layer R5
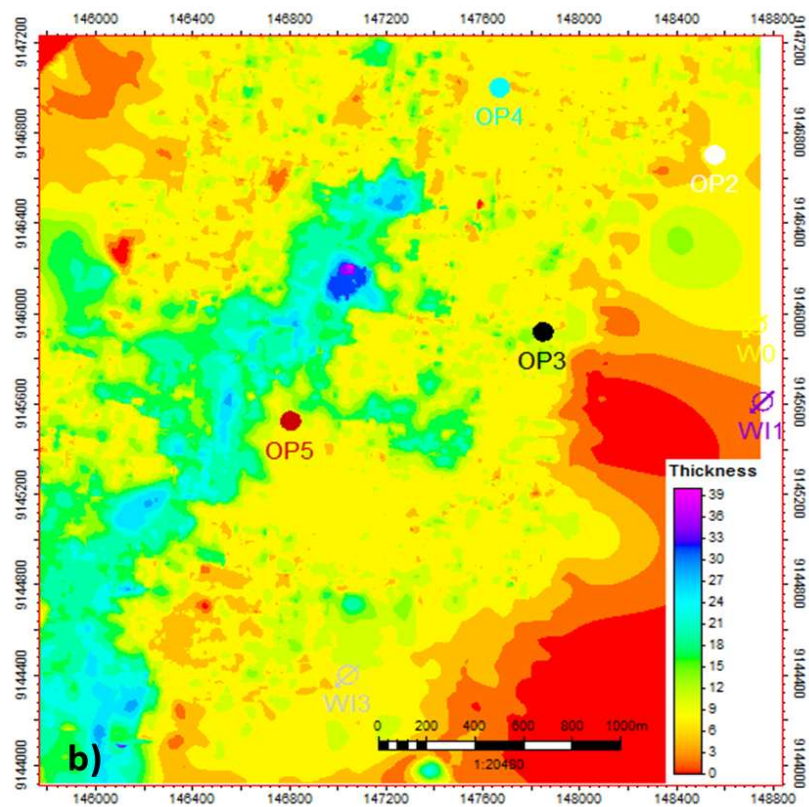
Figure 23: b) Thickness maps (in time) Reservoir layer R3

The information on Table 11 and Fig 23 was correlated with the interpretations on Fig 22 and to rank the reservoir potential of the channel-levee complexes (best to worse) as: complex 2, 3, 4 and 1. Appropriate ranking of these reservoir complexes would have been performed in terms of net pay maps however, the lack of geological information guided the alternative proving that even with less data useful interpretations can be obtained as long as uncertainty is considered.

2.5 Reservoir and fluid characterization

This project used 4D attribute analysis to interpret facies distribution and provide better understanding of reservoir connectivity. Qualitative information extracted from the seismic attributes was used by the numerical analysis. Using the build 3D computer reservoir model, relevant seismic attributes were mapped within the reservoir interval. The seismic attributes were sampled into the reservoir model through seismic resampling tools; average (2D) maps were produced from which quantitative information was extracted. The quantitative data exported represents a matrix of the attribute, where each cell contains attribute information.

Fig 24 shows is schematic representation of the approach taken to extract quantitative information from the seismic data and mapped attributes.
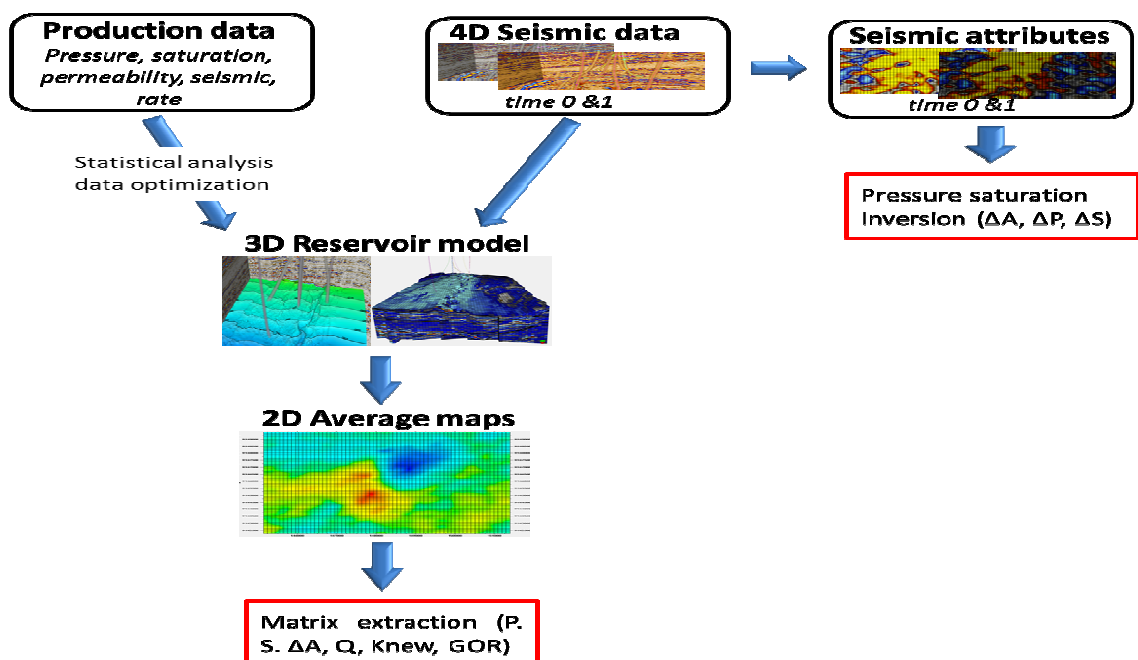
Figure 24: Steps involved in the extraction of quantitative information from 4D seismic and attributes.

Reservoir properties derived from seismic data can be used to predict porosity, lithology, pressure and presence of oil/gas saturation, under good data conditions

and supported by well control (Hanna, et al., 2011). The seismic response is affected by factors such as temperature, pressure, saturation, hydrocarbon viscosity, stress and fractures; therefore the seismic data can be used to quantitatively predict these parameters using seismic attributes derived from the seismic. A seismic attribute is a quantitative measure of a particular seismic characteristic of interest (Chopra, et al., 2005). In a broader sense, seismic attributes are all the information obtained from seismic data, either by direct measurements, logical or experience based reasoning.

Typical attributes include reflection terminations, pore pressure predictions, interval velocity, inversion of acoustic impedance, amplitude variation with offset and complex trace attributes. The amplitude content of the seismic data is the principal factor for the determination of physical parameters, such as the acoustic impedance, reflection coefficients, velocities and absorption while the principal factor in determining the shapes of the reflectors, their geometrical configurations is the phase component (Taner, 1994). The presence of hydrocarbon within the porous media typically lowers the seismic velocity and density of unconsolidated to moderately consolidated sandstones creates differential acoustic impedance contrast between the hydrocarbons charged sandstone and the surrounding water-bearing rock; this contrast produces anomalous seismic amplitude that may be visible on seismic displays (Hanna, et al., 2011).

Considering that the Dalia Field reservoirs are comprised mainly of unconsolidated sands, well data was used to calibrate the acoustic impedance contrast (fig 25) so that impedance contrast effects could accurately be used to map the hydrocarbon existence across the field. The reservoir characterization using the surface seismic combined with a good choice of seismic attribute was used to show the reservoir intervals containing the ultimate recoverable hydrocarbons.

The choice of seismic attributes was based on the attributes that better suit the needs of the project; such attributes should display changes on the seismic signature between T0 and T1. The seismic attributes were generated considering that:

- The seismic proved to be of high quality based on the resolution and the quality of interpretations derived from it (figs 21, 22 & 58-H)
- A good tie exists between the well tops and the seismic horizons (figs 25 & 56-H)
- Well log data was used to calibrate the seismic and seismic derived interpretations (horizons, surfaces, 3D grid), Figs 25 & 56-H.
- Well logs can be used to prove relationships between attributes and reservoir characteristics, Fig 56-H.

- The seismic alone can be used to show those relationships (fig 22)
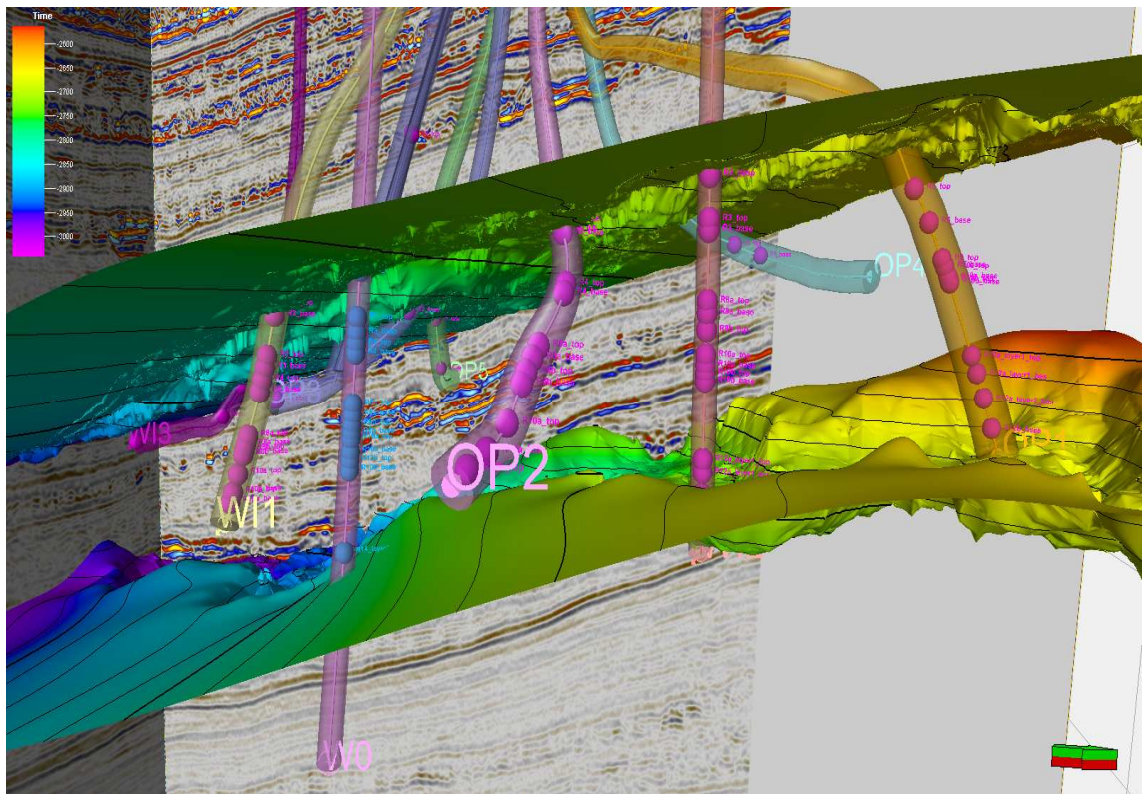
Figure 25: Top and bottom surfaces of the reservoir interval, seismic inline/cross-line and well tops. The picture shows a good relationship between the seismic data and well tops; Well tops were used to calibrate the seismic volume and other interpretations.

Seismic amplitude (P-wave) is an attribute related to the physical properties of the subsurface as a function of the reflectivity at the acoustic boundaries the acoustic impedance (Taner, 1994), this attribute was mapped and interpreted across the reservoir so that 4D anomalies could be related to changes in the reservoir as response to production (reservoir depletion and water injection). Seismic attribute analysis was preceded by the amplitude aliment of both seismic volumes (at *T0* and *T1*) to the same amplitude range so that differences in amplitude response could be attributed to reservoir production and not for differences in amplitude range.

During attribute analysis, the interpreted attributes were compared to saturation and pressure information estimated from well logs. Figs 26 & 27 respectively show the pattern of the mapped seismic attribute (P-wave amplitude) for the base survey (*T0*) and the monitor survey (*T1*), the figures show a very large difference in the amplitude response from T0 *(*fig 26) to T1 (fig 27). The reservoir is bellow bubble point however the strong shift in amplitude from *T0* to *T1* is essentially because the initial pressure is close to bubble point, as production starts ex-solution gas appears in the volume.
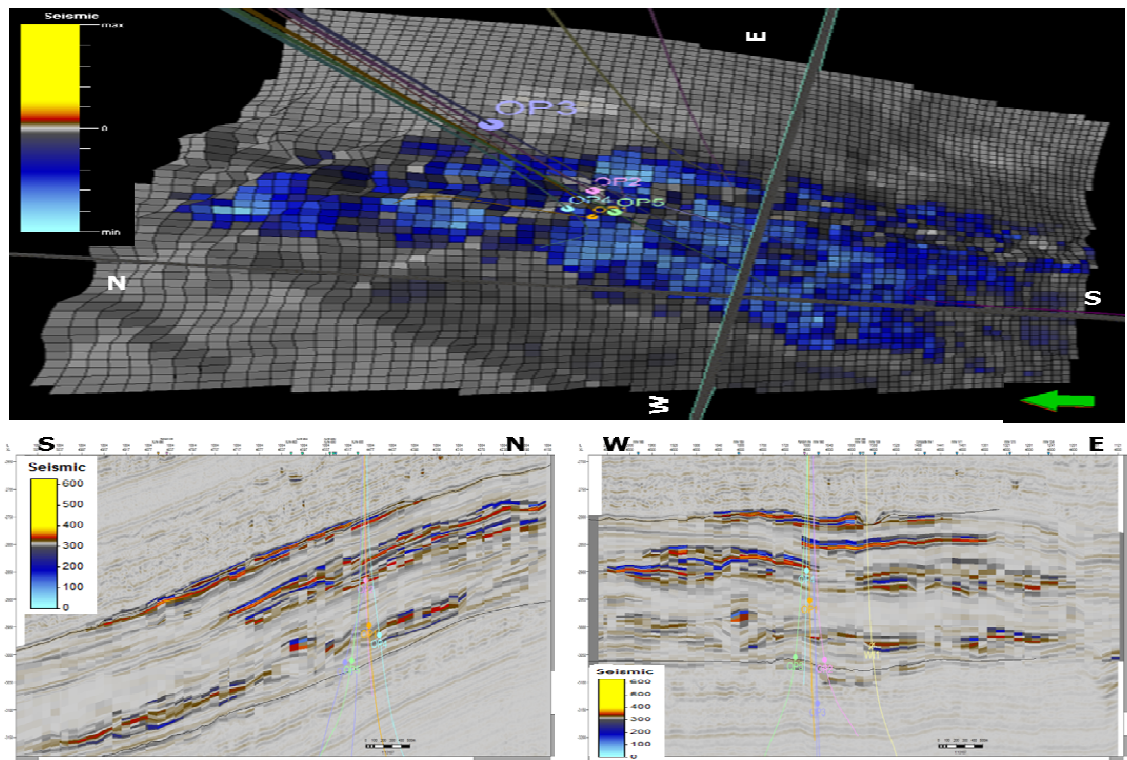
Figure 26: Seismic attribute (P-wave amplitude) on layer R1 of the geocellular model at T0 and S-N and W-E sections on seismic. On plain view (top), low amplitude response appears to be mainly around the channel with a N-S trend. The N-S and E-W cross-sections show the locations and reservoir layers and the magnitudes of the amplitude.
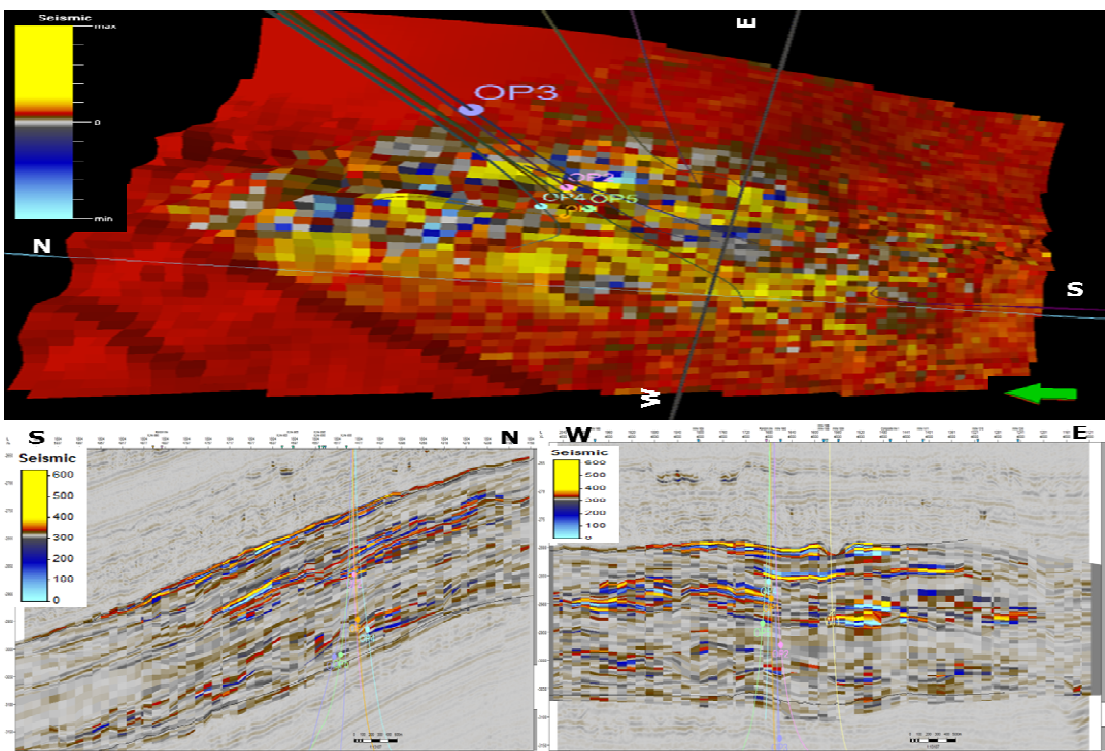
Figure 27: Resulting difference between seismic attribute response (P-wave amplitude) at T0 and T1. The image was used to identify zones where the reservoir has undergone significant changes associated with production.

61
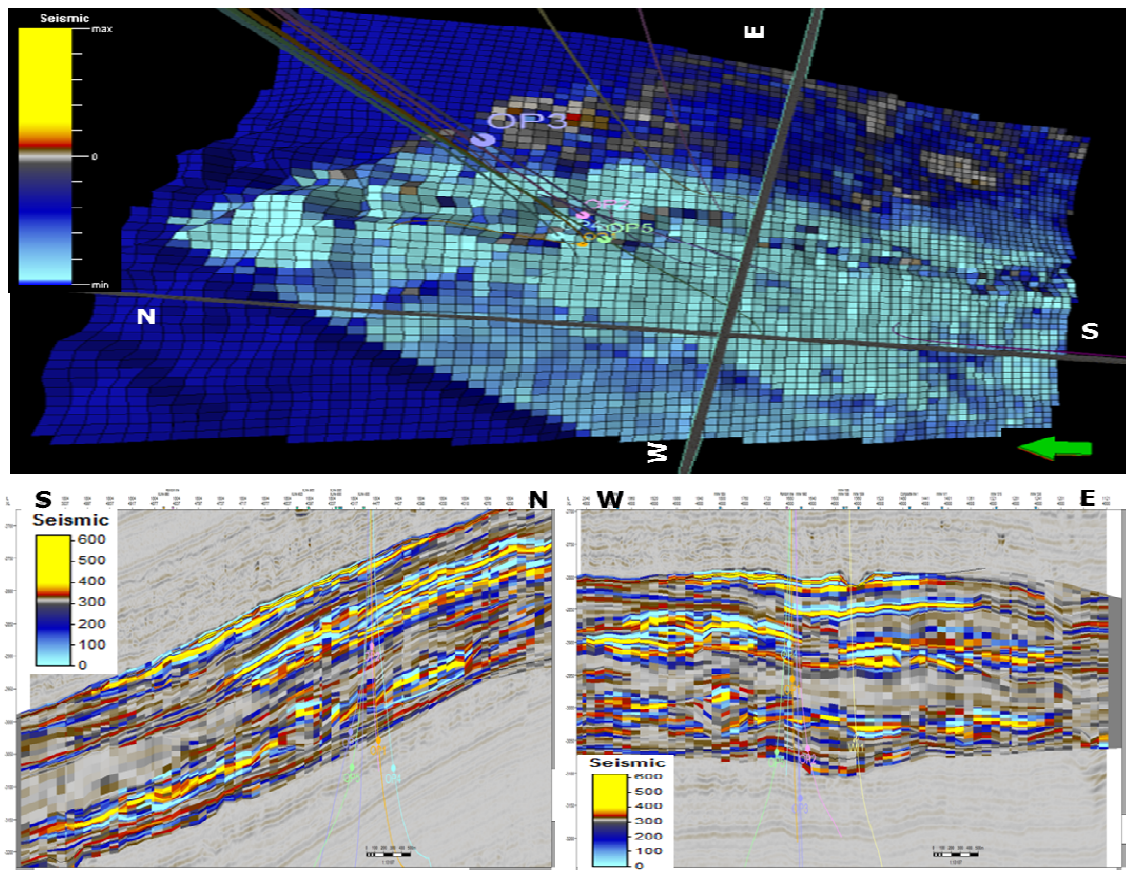
Figure 28: Seismic attribute (P-wave amplitude) on layer R1 of the geocellular model at T1 and S-N and W-E sections on seismic. The plain view (top), shows a wider spread of the amplitude response. The N-S and E-W cross-sections show the layers where the amplitude has changed.
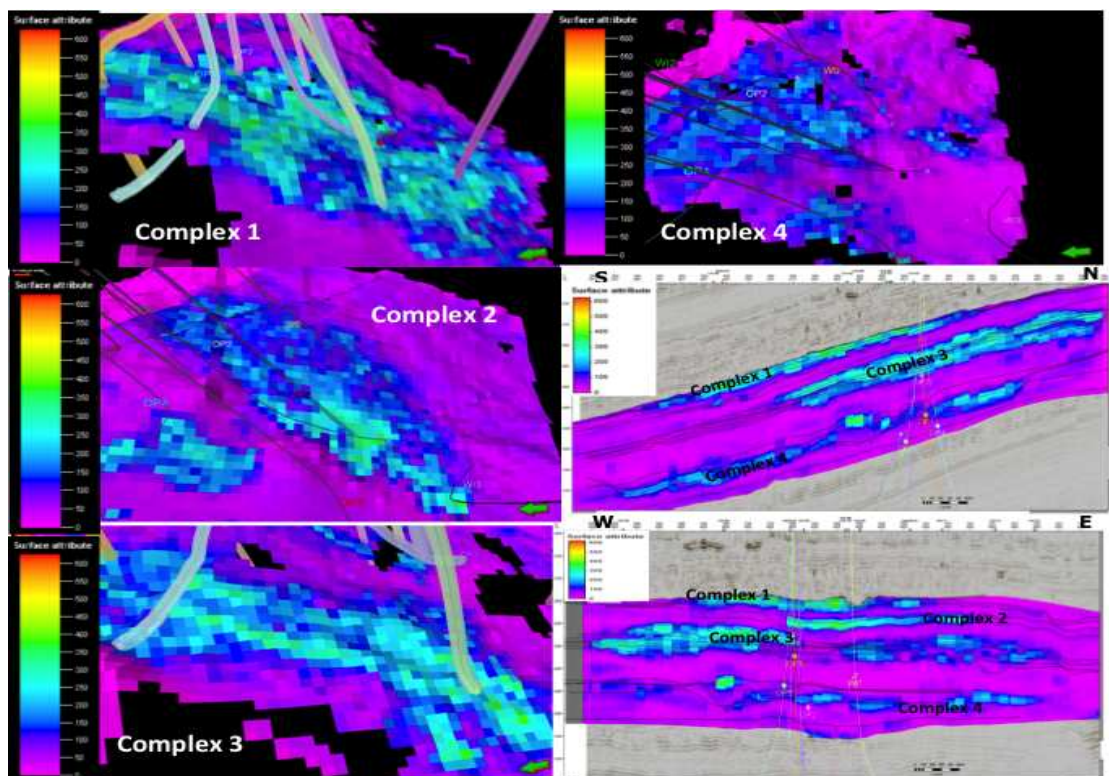
Figure 29: Difference between the seismic attribute response (RMS amplitude) at T0 and T1. In Fig 62-H the water saturation was lower than Fig 63-H, the difference between those two images is here represented to show the advance in water saturation front.

Interpretation of Fig 26-28 allowing inferring that the small increase in in gas saturation decreases the P-wave velocity, which causes strong negative P-wave velocity variations and high positive time shifts between *T0* and *T1*. Closer to the water injectors as water replaces oil a positive P-wave velocity variation is induced and negative time-shifts occur between *T0* and *T1*.

The difference in the RMS amplitude between *T0* and *T1* is shown in Fig 29, the picture shows depletion of the reservoirs in the 4 main channel-levee complexes shown by negative amplitudes. This depletion is attributed to changes in pressure between *T0* and *T1* (~28 to ~36 bars, fig 10) and apparent good reservoir communication within the complexes (Fig 20). The changes in pressure associated with oil depletion would have induced negative changes in the amplitude values of about -18% around the producers (figs 29, 62-H & 63-H). Injection of water would have caused advancement of the waterfront inducing positive changes in the amplitude values 16% (figs 29, 62-H and 63-H).

2.5.1   Pressure saturation inversion

A relationship was established between reservoir properties (i.e.: saturation and pressure) and the mapped seismic attributes (P-wave and RMS amplitude). Computation of the seismic attributes pressure velocity (V_p), shear velocity (V_s) and bulk modulus (K_b) was performed using the Gassmann–Biot equation (Gassmann, 1951; Biot, 1956), in the form:

$$\rho = \frac{\phi}{\rho_{fl}} + \left(1 - \phi\right) \times \rho_{grain} \tag{2-8}$$

$$V_p = \sqrt{\frac{K_{sat} + \frac{4}{3}\mu}{\rho}} \tag{2-9}$$

$$Vs = \sqrt{\frac{\mu}{\rho}} \tag{2-10}$$

Where ρ_{grain} and ρ_{fl} are the grain and fluid densities, μ is the shear modulus which does not depend on fluid, K_{sat} is the effective bulk modulus of the rock with pore fluid, $\varnothing$ is the porosity and ρ is density. The detailed derivation compute seismic attributes (Vp, Vs and Kb) from reservoir properties (S, P and $\varnothing$) can be found in *appendix G.* As a requirement for attribute computation, reservoir properties must exist; hence the petro-elastic model is dependent on reservoir data and constrained by its quality. The three seismic attributes in equations 2-8 to 2-10 can be estimated using reservoir properties such as saturation, porosity and pressure. However, the objective here is to estimate reservoir properties using the seismic

attributes extracted from the reservoir model. Several authors proposed different seismic inversion techniques and stochastic inversion tools that aid the prediction of the intended properties (Taner, 1994; MacBeth, et al., 2005; Vasco, et al. 2004; Vasco, 1999).

This project used the statistical inversion approach proposed by MacBeth, et al., (2005) to estimate reservoir properties using the seismic attributes extracted from the reservoir model. This approach was derived using a two-phase reservoir in which the seismic attribute A, depends on the reservoir thickness (τ), lithology (L), porosity (ϕ), and reservoir pressure (P) and oil saturation (S_o):

$$A = A\left(x, y, \tau, L, \phi, P, S_o\right) \tag{2-11}$$

where A is a mapped function of x and y, defined on the picked horizon of interest. A relationship between 4D seismic and dynamic reservoir changes (pressure and saturation) was established through the formula:

$$\frac{\Delta A(x,y)}{\overline{A_b}} \approx C_S \frac{\Delta S_o(x,y)}{\overline{S_{oi}}} + C_P \frac{\Delta P(x,y)}{\overline{P_i}} \tag{2-12}$$

where ΔA, ΔS_o and ΔP represent changes in seismic attribute, oil saturation and reservoir pressure respectively; $\overline{A_b}$ represent average baseline response, $\overline{S_{oi}}$ and $\overline{P_i}$ are the average initial saturation and pressure in the reservoir. C_s and C_p represent dimensionless coefficients used to calibrate the production data to the 4D seismic signatures.

Equation (2-12) correlates attribute data with dynamic data, considering the initial and final times, this equation can be transformed into:

$$A_0(x,y) - A_1(x,y) \approx C_S \left[S_{n,0}(x,y) - S_{n,1}(x,y)\right] + C_P \left[P_0(x,y) - P_1(x,y)\right] \tag{2-13}$$

Because only initial saturation data was estimated from log, through pressure saturation inversion, the saturation at *T1* can be estimated using the expression:

$$S_{n,1}(x,y) \approx \frac{\left\{\left[A_0(x,y) - A_1(x,y)\right] + C_P \left[P_0(x,y) - P_1(x,y)\right]\right\}}{C_S} + S_{n,0}(x,y) \tag{2-14}$$

Equation 2-14 can be used to estimate the saturation of any fluid (S_{oil} or S_{water}) at a given time (in this case *T1*) given that attribute and pressure information are available at *T0* and *T1* in addition to the initial saturation information. Similar to the estimation of saturation, any parameter in (2-14) can be estimated given the initial distribution of the parameter is known and the other parameters to satisfy the equation are available or can be estimated.

CHAPTER 3   MATHEMATICAL MODEL

Overview

This chapter is dedicated to the derivation of the governing differential equations upon which the final permeability equation will be derived. The final equation follows the logic of the equations used to model the fluid flow within reservoirs.

3.1 Three-phase flow - reservoir producing oil, gas and water

This section outlines the permeability differential equation based on Dalia Field reservoirs (producing oil, gas and water) nevertheless the amount of water produced is considerably low compared to the hydrocarbons.

Estimation of reservoir permeability using numerical modelling thought the appropriate mathematical equations, can often become a complex problem because the equations have to characterize simultaneous fluid flow with different phases within the same reservoir (Gassman, 1977). A parameter such as permeability changes with pressure, which in turn has spatial variability in the reservoir, this reality was difficult to capture due to the non-linearity and spatial dependence of the parameters. The project used inversion techniques to derive differential equations that incorporate non-linear properties of the reservoir flow and their spatial distribution; these differential equations were used to describe the relevant physical processes that take place within the reservoir, to model fluid flow of the reservoir immiscible fluids (oil, water and gas) and describe mass transfer between the different phases; due to the complexity of the reservoir flow the differential equations were very long . The mathematical model took into account the geometry of the reservoir, its heterogeneity and the occurring physical processes within the reservoir.

Using the fluid flow equations proposed by Peaceman, (1977)*,* the equation for estimating the reservoir permeability was derived using an initial permeability map (fig 20), 4D seismic and production information. Two distinct times (*T0* and *T1*) were defined and these precisely coincide with the dates at which the seismic surveys were acquired. Because production data was limited to the 9 wells, the interwell space was populated using geostatistical extrapolation techniques. Adjustments to the model and some assumptions were necessary to optimize the production data as well as simplify the mathematical model without compromising reliability of the results.

The main assumptions for the derivation of the differential equations include: The reservoir is laterally extensive compared to small thickness (sheet-like reservoir in reservoir engineering terms), presented by two-dimensional equations for fluid flow where capillary pressure is neglected and changes in GOR are very small. The nomenclature specifies the units of the various symbols and their respective quantities, the individual constants and units are specified at the derivation.

The choice of fluid flow equation was based on the reservoir description and characterization (*chapter 2*), a detailed mathematical development of the method can be found in *appendix B*. *Chapter 2* establishes that the Dalia reservoirs are at under-saturated flow conditions between 2007 and 2008, therefore the only fluids present in the reservoir are oil, gas, and water (no gas cap). For this case the derivation of the differential equation for permeability estimation made use of the three-phase flow equation proposed by Peaceman, (1977) in the form:

$$\nabla \cdot \left[\frac{\alpha \rho_o K k_{ro}}{\mu_o} \left(\nabla P_o - \rho_o g \nabla D \right) \right] + \alpha q_o = \alpha \frac{\partial \left(\phi \rho_o S_o \right)}{\partial t} \qquad (3\text{-}1)$$

$$\frac{\partial}{\partial x} \left[R_{so} \frac{K k_{ro}}{\mu_o B_o} \frac{\partial P_o}{\partial x} \right] + q_g' - R_{so} q_o' = \frac{\partial}{\partial t} \left(R_{so} \frac{\phi S_o}{B_o} \right) \qquad (3\text{-}2)$$

$$\nabla \cdot \left[\frac{\alpha \rho_w K k_{rw}}{\mu_w} \left(\nabla P_w - \rho_w g \nabla D \right) \right] + \alpha q_w = \alpha \frac{\partial \left(\phi \rho_w S_w \right)}{\partial t} \qquad (3\text{-}3)$$

Equations (3-1 to 3-3) were used to characterize the fluid flow for the oil, gas from solution and water phases respectively. Using the detailed derivations depicted in *appendix B.2* the governing equation defined by the mathematical model (optimized to the Dalia Field data) is given by:

$$\nabla \cdot \left[K . \alpha . \nabla P \right] = q - Q \qquad (3\text{-}4)$$

Where:

$\alpha = GOR.M_o + M_o + M_w$ a variable used to simplify (3-4) from which

M_o is the oil mobility of the oil, a function of oil relative permeability K_{ro}, oil viscosity μ_o and oil formation volume factor B_0.

M_w is the water mobility, a function of water relative permeability K_{rw}, water viscosity μ_w and water formation volume factor B_w.

$q = GORq_o'$, rate of produced gas, a function of the gas-oil-ratio (GOR) and rate of produced oil q_0'.

$Q = q_g' + q_o' + q_w'$, is the total production rate resulting from the sum of water q_w', oil q_o' and gas q_g', production rates [m³/day].

$Q_\Delta = (q_0 - q_1) - (Q_0 - Q_1)$ is a parameter relating differences in rate [m³/day] between *T0 and T1* .

Using a numerical approach, equation (3-4) is used in the next chapter to isolate the absolute permeability where the parameter is made a function of the initial permeability, 4D seismic and the production data.

3.2   Two-phase flow - reservoir producing oil and water

This section outlines the permeability differential equation based on synthetic data from a UK field (producing oil and water) where the amount of water produced is high enough to impact hydrocarbon production, therefore saturation data in terms of phase mobility data and water breakthrough is considered to be important.

 Starting from the fluid flow equations for oil and water respectively (3-1 & 3-3) proposed by Peaceman, (1977) assuming incompressible flow (D, ρ_o and ρ_w are constant), also for simplicity ϕ is considered constant with pressure while α is considered constant with position, then single fluid flow *equations (3-1 & 3-3)* can be re-written as:

$$\nabla \cdot \left[\frac{Kk_{ro}}{\mu_o} \nabla P_o \right] + Q_o = \phi \frac{\partial S_o}{\partial t} \qquad (3-5)$$

$$\nabla \cdot \left[\frac{Kk_{rw}}{\mu_w} \nabla P_w \right] + Q_w = \phi \frac{\partial S_w}{\partial t} \qquad (3-6)$$

where $Q_o = \dfrac{q_o}{\rho_o}$ and $Q_w = \dfrac{q_w}{\rho_w}$ are respectively the volumetric rates of production

[m^3/day].

Following the derivations on *appendix B.3* the mathematical equation to estimate horizontal permeability based on the two-phase flow case is given by:

$$\nabla.\left[Kf_1\psi_1\nabla P_1 - Kf_0\psi_0\nabla P_0 \right] = Q_\Delta$$

(3-7)

Where *K* stands for permeability [mD]

f stands for fractional flow

∇P stands for change in reservoir pressure with position [bar, Pa or psi],

$$\psi_0 = \left(-M_t - \frac{M_o}{f_0} \right)$$

$$\psi_1 = \left(-M_t - \frac{M_o}{f_1} \right)$$

and $Q_\Delta = Q_1 - Q_0$ stands for differences in rate [m^3/day] between *T0 and T1.*

CHAPTER 4   NUMERICAL MODELLING

Overview

Within this chapter, the final equation to estimate the absolute permeability is derived. The absolute permeability equation was achieved by representing the partial differential equations (*3-4 & 3-7*) into a system of algebraic equations through finite difference methods by finite difference quotients. An approach to improve the visual characteristics of the results produced by the numerical model is also presented.

4.1   Equation optimization of the mathematical model

This section outlines the approximations and transformations applied to the differential equations in *chapter 3* to make it possible for these equations to be solved by computer codes written by the author. Here, the *non-linear* partial differential equations were rendered *pseudo-linear* so that computer programs could use them.

4.1.1   Three-phase flow - reservoir producing oil, gas and water

Using the approximation of the product rule for the ∇ operator, equation (3-4) is re-written as:

$$\nabla K \cdot \Phi_1 + K \nabla . \Phi_1 - \nabla K \cdot \Phi_0 + K \nabla . \Phi_0 = Q_\Delta \tag{4-1}$$

Complete derivation of equation (4-1) can be found in appendix B.2 (equations B-80 an B-81). For the finite approximations of the partial derivative the Newton's difference quotient is used. By manipulation of equation (4-1), *K* was isolated by considering that the properties of the reservoir vary in two prominent directions *x* and *y.* Using a conceptual reservoir model composed of a grid which considers the two space variables (fig 30), this grid was divided up the reservoir region into an x-y plane. The integer *i* represents the index in the *x*-direction, and the integer *j* represents the index in the *y*-direction.

Thus x_i is the ith value of x, and y_j is the jth value of *y*; double indexing was used to identify functions within the two-dimensional region. Thus: $K_{ij} = K (x_i, y_j)$
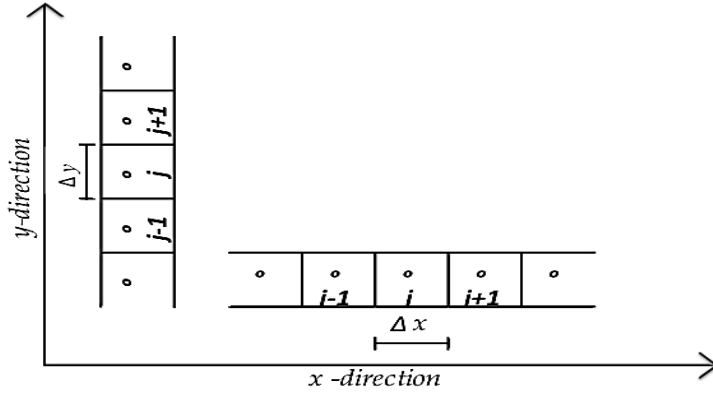
Figure 30: Representation of the block-cantered grid

Using simplifications and approximations in (*appendix B.2),* the permeability in (4-1) was isolated for i^{th} and j^{th} nodes in the *x and y*-directions, yielding:

$$
K_{i,j} = \left[Q_\Delta + \frac{\Phi_{1,i}}{\Delta x} K_{i-1,j} + \frac{\Phi_{1,j}}{\Delta y} K_{i,j-1} + \frac{\Phi_{0,i}}{\Delta x} K_{i-1,j} + \frac{\Phi_{0,j}}{\Delta y} K_{i,j-1} \right] \cdot
$$
$$
\left[\left(\nabla.\Phi_1 + \frac{\Phi_{1,i}}{\Delta x} + \frac{\Phi_{1,j}}{\Delta y} \right) - \left(\nabla.\Phi_0 + \frac{\Phi_{0,i}}{\Delta x} + \frac{\Phi_{0,j}}{\Delta y} \right) \right]^{-1}
$$

(4-2)

Equation (4-2) is the final equation for estimating the permeability; at initial saturation conditions, the estimated ($K_{i,j}$) depends on changes in the total flow rate (Q_Δ), spatial variability of the initial permeability estimates (K_{i-1} and K_{j-1}) and spatial variability of parameter Φ, defined in equations (B-19 and B-20).

At survey time *n*, $\Phi_n = \alpha_n \nabla P_n$ where ∇P_n is the pressure gradient at a given survey time and α_n is a function of fluid. Φ contains pressure and saturation data (mobility information in α), hence the identified relationship between the propagation of the saturation front and pressure field.

Parameter Φ does not correlate linearly with the updated permeability estimates and second-order differentials; the Laplace integral transform was used to characterize the spatial variations of this the parameter. Because Φ contains pressure changes and changes in α, the confidence of these two parameters in regions away from the wells is expected to be slightly lower than those closer to the well, therefore, the error associated to these estimates can be controlled with less confidence as the distance to the wells increases. To access the robustness of the method, the computer program built to solve equation 4-2 including ways to

calculate and visualise the Laplace terms so that the spatial variability of parameters in second-order differential can be assessed.

4.1.2 Two-phase flow - reservoir producing oil and water

The detailed derivation of the governing equation for estimation of permeability for the two-phase flow is described in *appendix B.3; u*sing these set of approximations and transformations the equation to estimate permeability for a reservoir producing oil and water where water production has impact on hydrocarbon production is given by:

$$
K_{i,j} = \left[Q_\Delta + \frac{\Phi_{1,i}}{\Delta x} K_{i-1,j} + \frac{\Phi_{1,j}}{\Delta y} K_{i,j-1} + \frac{\Phi_{0,i}}{\Delta x} K_{i-1,j} + \frac{\Phi_{0,j}}{\Delta y} K_{i,j-1} \right].
$$
$$
\left[\left(\nabla.\Phi_1 + \frac{\Phi_{1,i}}{\Delta x} + \frac{\Phi_{1,j}}{\Delta y} \right) - \left(\nabla.\Phi_0 + \frac{\Phi_{0,i}}{\Delta x} + \frac{\Phi_{0,j}}{\Delta y} \right) \right]^{-1}
$$

(4-3)

Equation (4-3) is the final equation for estimating the permeability for the two-phase flow; at initial saturation conditions, the estimated ($K_{i,j}$) depends on changes in the total flow rate (Q_Δ), spatial variability of the initial permeability estimates (K_{i-1} and K_{i-1}) and spatial variability of parameter Φ, defined in equations (B-76 and B-77).

At survey time *n*, $\Phi_n = f_n.\psi_n.\nabla P_n$ where ∇P_n is the pressure gradient at a given survey time, ψ is a variable that changes with mobility defined as $\psi_n = -\left(M_t + \frac{M_0}{f_n} \right)$. Φ Contains pressure and saturation data (mobility information and fractional flow data in ψ), hence the identified relationship between the propagation of the saturation front, fractional flow and pressure field.

Parameter Φ does not correlate linearly with the updated permeability estimates and second-order differentials; the Laplace is used to characterize the spatial variations of this the parameter. Because Φ contains changes in pressure, fractional flow and ψ, the confidence of these two parameters in regions away from the wells is expected to be slightly lower than those closer to the well, therefore, the error associated to these estimates can be controlled with less confidence as the distance to the wells increases. To access the robustness of the method, the computer program built to solve equation 4-3 includes ways to

calculate and visualise the Laplace terms so that the spatial variability of parameters in second-order differential can be assessed.

4.2   Regularization and smoothing

Within the mathematical model, due to the type input data, it was difficult to change the experimental system to generate a particular set of results suitable to the needs of the project, instead, manipulations of the updated results have been made to honour prior information of the field and visual requirements adequate for comparison with results obtained using the reservoir model. These adaptations involved the application of *smoothing or regularization techniques,* through which visually poor results were improved by considering results, obtained using the computer model.

The project used a *regularization technique* proposed by Gonzalez-Rodrighez, et al., (2005) in which the regularization tool is derived by means of propagation back-propagation algorithm to produce stable reconstruction processes by incorporation prior information into the reconstruction. This approach estimated the permeability distribution within a reservoir based on field data. Given a homogenous distribution of the permeability, using the approach, the difference between estimated permeability and that extracted directly from well data is calculated, the residuals are then back-propagated numerically into the reservoir by solving the proposed equations so that the corrections to the initial estimate could be obtained from the results. To reduce data misfit the approach used *smoothing with the heat kernel* (Gonzalez-Rodrighez, et al., 2005)*.*

The Gonzalez-Rodrighez regularization approach (*appendix F*) was used to smooth the edges and remove visual discontinuity inherent from the manipulation of matrices of data, the regularization equation takes the form:

$$\Delta K(i,j) = K^n + \theta \left[\beta. \left(K_{i+1,j}^n - 2K_{i,j}^n + K_{i-1,j}^n + K_{i,j+1}^n - 2K_{i,j}^n + K_{i,j-1}^n \right) + \alpha K^n - K_0 \right] \quad (4\text{-}4)$$

α and β are weighting parameters used to steer the regularization of the permeability (K) using initial permeability distribution (K_0) in a efficient and predictable way; the ratio $\gamma = \beta/\alpha$ is considered to be a regularization parameter

which provides indication for the smoothing properties of the approach; the number of iterations is given by parameter $n = 1, 2, 3, …, N$

The regularization procedure in (4-4) was applied to the permeability distribution in order to smooth the sharp discontinuities from the produced results.

CHAPTER 5   APPLICATION TO FIELD DATA

Overview

To estimate proposed permeability approaches that correlate dynamic data and 4D seismic, the author created computer programs. First the approach was tested with the Dalia Field data and then with synthetic data from a UK field.

5.1   Application to Dalia Field data

The permeability estimation approach produced by the project was tested in terms of effectiveness in producing new estimates, limitations and uncertainty. The optimized pseudo-linear equations outlined in *chapter 4* (section 4.1.1 and 4.1.2) together with numerical data extracted directly from the Dalia Field reservoir model were used to create computer programs (here interchangeably referred to as simulators) to estimate horizontal permeability as a single 2D map; the 2D simulator was built using numerical data extracted from average properties of the 3D model to allow a 2-dimensional analysis (fig 61-Hc). Permeability estimates were obtained through the use of algorithms that use equations (*3-4 & 3-7*) to correlate data output by the Dalia Field reservoir model, PVT & statistical analysis and field information. To describe the features and structure of the Dalia reservoir model the simulator consisting of a 64 by 74 grid was built using the numerical model described in *section 4.1.1* to test the proposed approach on a reservoir producing oil, gas and very small amounts of water; figures extracted from the reservoir simulator were used to illustrate similarities and differences between the reservoir model and simulator as well as test the efficiency of the approach.

The simulator tested the distribution of initial permeability using different theoretical models (2.3.2) and Fig 31 illustrates some of the results produced by the use of initial theoretical models to estimate the initial permeability.

Results from the figure below were compared with field data to determine the theoretical model that best honours the field data. Based on the degree of agreement between real data (table 3) and simulator results (fig 31) the project used the Timur approach to estimate the initial permeability (section 2.3.2). The reference model (fig 31a) shows permeability values higher at the centre of the field and close to the producer wells stretching to the north, south and southwest. Lower permeability values are seen mainly in the northeast part of the field, around water injectors and some northwest portions of the reservoir. The initial distribution of permeability produced by the simulator appears to be in more agreement with pressure distribution (fig 69) than that the initial permeability (fig 19a) this can be

interpreted as being a result of strong influence that the pressure exerts on the permeability.
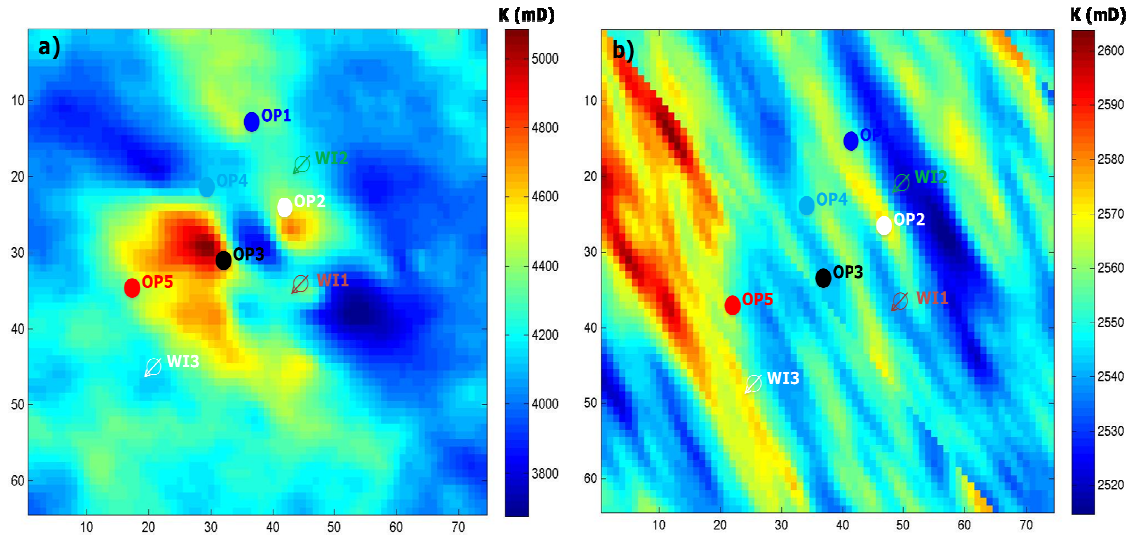
Figure 31: Permeability (mD) distribution estimated using different theoretical models and same variogram (note the different scale bars) **(a)** Timur theoretical model, producer wells are labelled OP and water injector, WI. **(b)** Permeability (mD) distribution estimated using Coates theoretical model, producer wells are labelled OP and water injector WI.

Figs 31a & 31b were generated using numerical data extracted respectively from Figs 19a & 19b, the numerical data these figures was input into a computer program from which Figs 31a & 31b were generated and the difference between these two figures is a reflection of the input data. The initial saturation was investigated using different saturation parameters, the suitable *m* and *m* parameters were chosen based on the level of agreement with the available field data, where case 3 (fig 17c) proved to be the best case scenario for the initial saturation (*table 8*).

From the 3D model, arithmetic average (2D) maps of the saturation were generated at *T0*. The computer program to illustrate the distribution of water saturation at T0 used the numerical data extracted from Fig 17c. Changes in water saturation between *T0* and *T1* were estimated using the pressure-saturation inversion model proposed by MacBeth, et al., (2005) though equation (4-4). Figure 32a shows the distribution of water saturation at *and* Fig 32b shows the distribution of water saturation at T1.
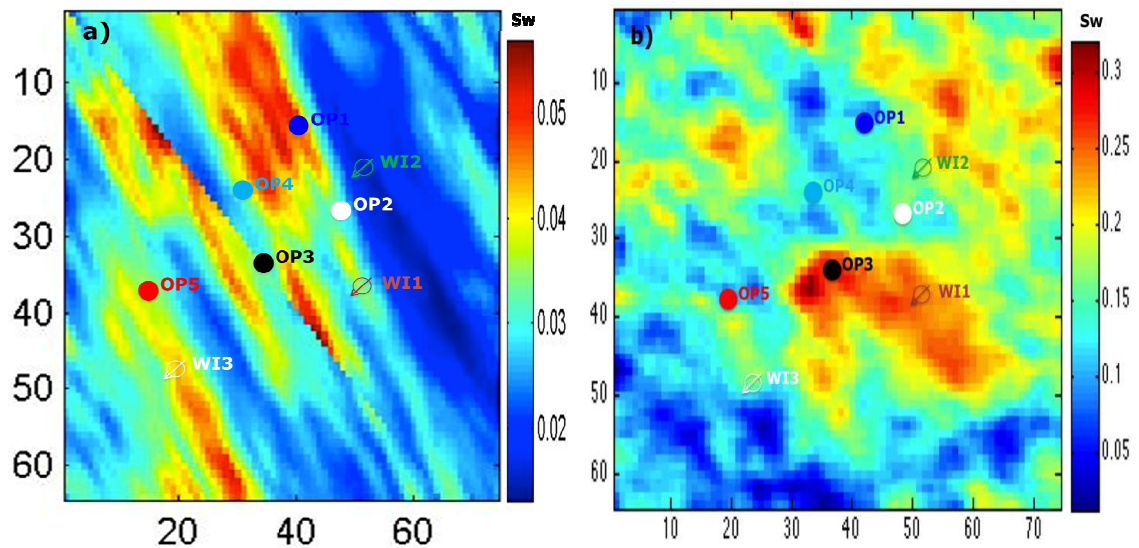
Figure 32: Comparison between the water saturation arithmetic average maps (note the different scale bars), producer wells are labelled OP and water injectors are labelled WI **(a)** Initial water saturation (*T0*) **(b)** Water saturation at *T1* after production.

From Figure 32a, the magnitudes of the initial water saturation (*T0*) displays very low saturation levels, at *T1* (fig 32b), the water appears to have migrated from the injectors towards the producer wells along areas of high permeability (particularly in the vicinity of OP3). At *T1* highest water saturation values appear more concentrated around the injectors and producer OP5 that can be interpreted as being a result of the implemented injection strategy used to maintain production pressure. Another reason for the high saturation could be the good connectivity between reservoirs penetrated by WI1 and OP3.

Average reservoir pressure was estimated using fluid gradient information obtained from the production data (appendix E). Through stochastic methods the reservoir pressure at well locations was populated across the field. Figure 33 shows results of the reservoir simulator for the initial pressure, the figure shows a varying reservoir pressure varies across the field; the highest pressure values are mainly concentrated at the central and northern parts of the field this is confirmed by statistical information showing a relatively narrow distribution with about 38% probability of pressure around 200 bar (3000 psi).
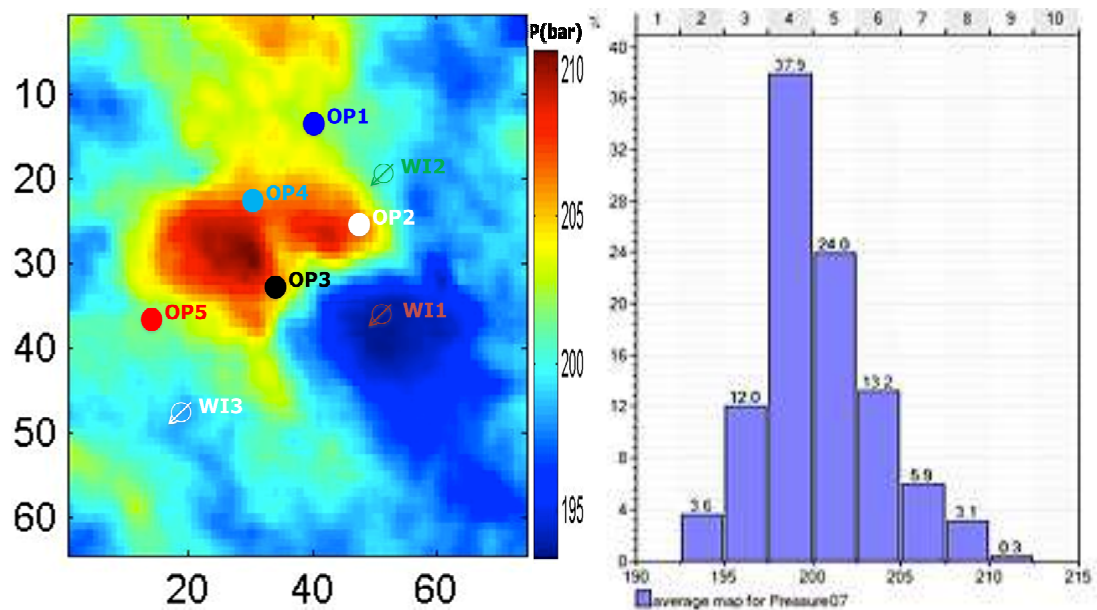
Figure 33: Simulator results of the initial distribution of the reservoir pressure at T0. The histogram of the pressure at T0 shows a relatively narrow distribution of the property. This information was used to estimate the new permeability distribution.

As a response to production, the average reservoir pressure at *T1* has declined (fig 34), now showing a relatively wider distribution with about 12% probability of pressure around 170 bar (2500 psi).
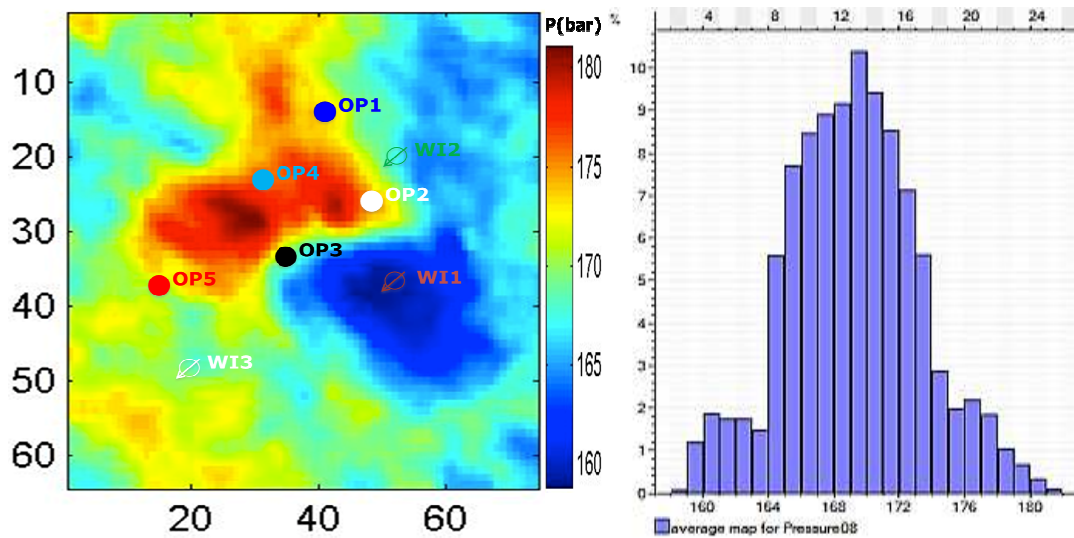
Figure 34: Simulator results for reservoir pressure at T1 (scale in bar). The histogram of the pressure at T0 shows a relatively wider distribution of the property.

The figure above shows highest pressure values at *T1* are no longer concentrated at the centre of the field. Instead they appear more spread on the N-W and SW parts of the field with a spread between 160 – 180 bars; pressure values at *T1* around

the water injectors also appear to have increased compared to *T0* when the injection strategy was not implemented.

Using the bicubic spline interpolation approach proposed (Salkauskas, 1984; Read & Cressie, 1988) the gradient and magnitude of the gradient for the pressure was estimated to access the degree of variability of the pressure; according to Fig 35c, the magnitude of the gradient of the initial pressure is constant, except to a small area in the centre of the field.

Analysis similar to fig 35 was performed with the pressure at *T1,* also revealing constant gradient of pressure after production start. The heterogeneity of the reservoir can be appreciated by the relative changes in pressure at the centre of the field that can be correlated to high permeability in the centre of the model as seen in (fig 31a). The changes in the reservoir pressure (∇P) between *T0* and *T1* were also estimated (fig 37, top) because they represent an important component of the equation used to estimate the new permeability with equation 3-4; these changes represent pressure changes with time due to depletion of the reservoir and they appear to more accentuated near the injectors due to the relationship between the water mobility and the changes in pressure caused by production/injection.
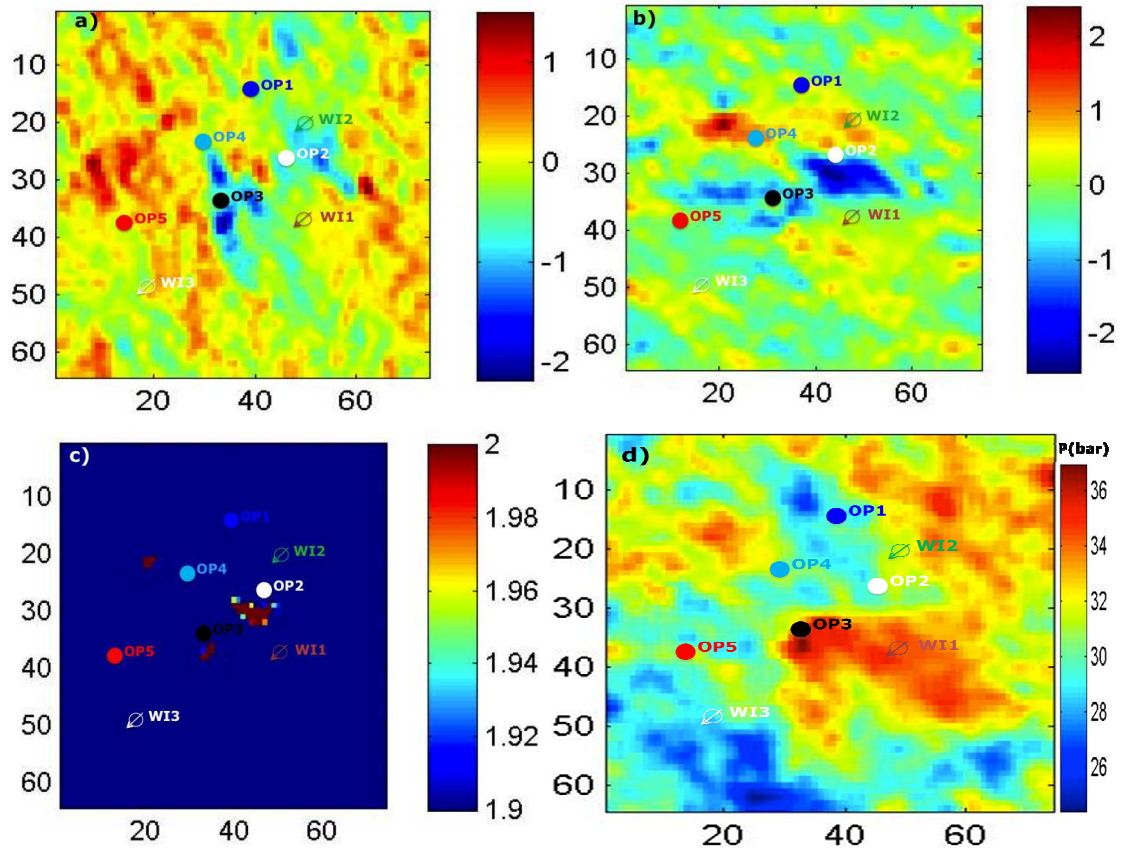
Figure 35: Gradient of the pressure at *T0* (different scales). **(a)** In the x-direction **(b)** In the y-direction; **(c)** Magnitude of the gradient at *T0*; **(d)** Change in pressure, ∇P between *T0* and *T1*.

Equation 4-2 was used to estimate permeability (K) though a relationship between the variable Φ and change in flow rate with time Q_Δ. Φ is a vector quantity defined in equations B-19 & B20 to relate total mobility information with changes in pressure with time (∇P).

The figure below shows that the magnitude of the gradient component Φ displays some similarity to the magnitude of the initial pressure. Q_Δ represents the change in flow rate between *T0* and *T1* obtained from the direct estimation of the difference in flow rate at wells (equation B-18) .
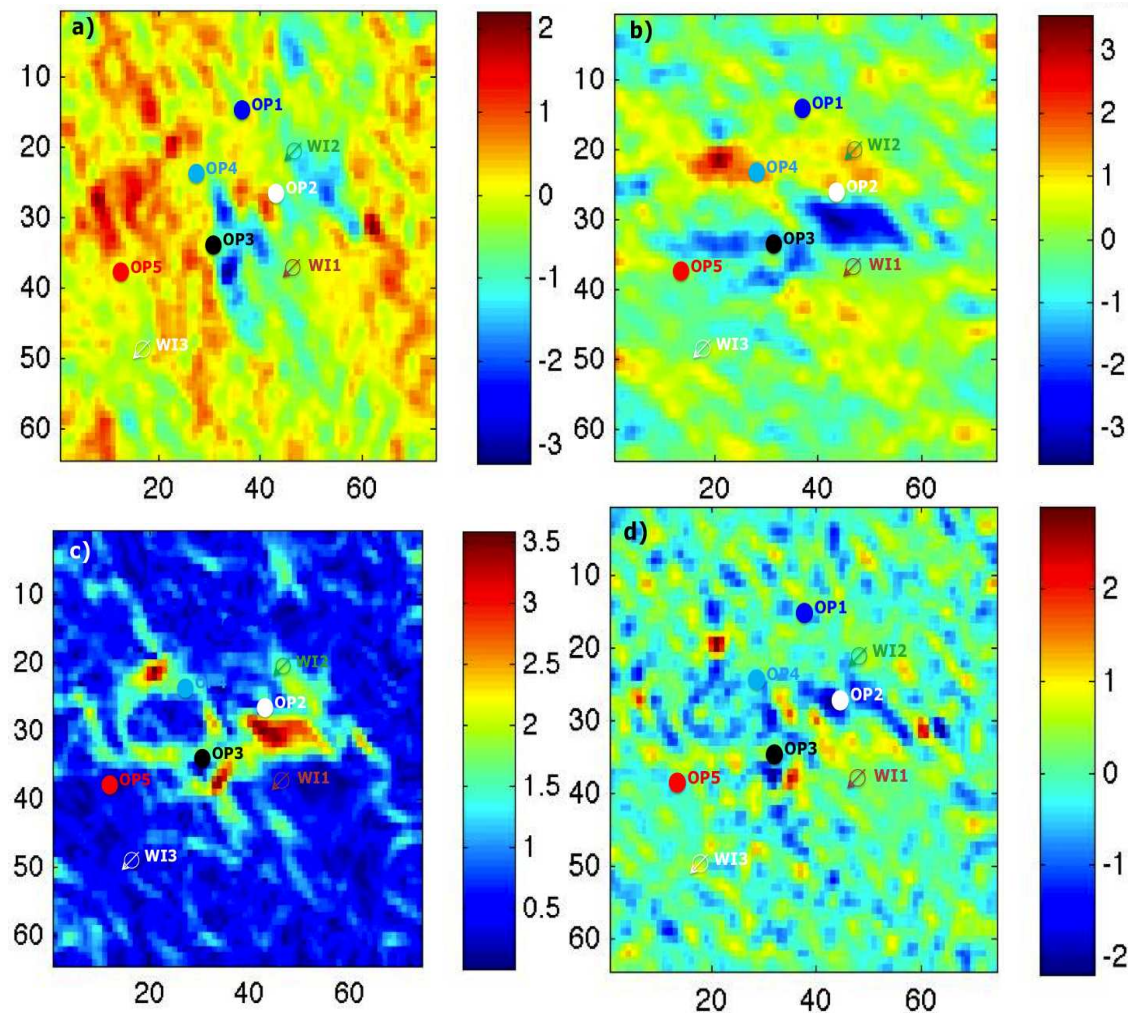
Figure 36: Component Φ **(a)** Spatial variability of the component at time 0, in x-direction. **(b)** Spatial variability of the component at time 0, in y-direction. **(c)** Magnitude of the gradient of the component. **(d)** Divergence of the Φ component.
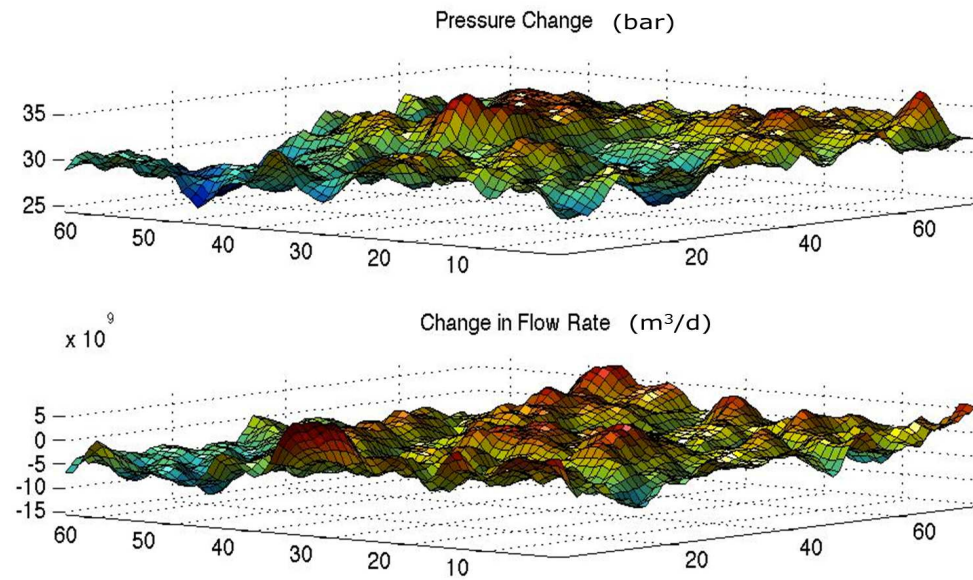
Figure 37: Surface plot of the changes in pressure (top) and flow rate (bottom)

For the estimation of permeability K, the initial permeability model (fig 31) was used as the initial estimate together with Newman boundary condition to solve the differential equation using the written computer program. The permeability was estimated using the computer designed to solve the optimized version of equation 4-2 in which matrix data of all the relevant parameters (extracted from the single layer 2D model of the Dalia reservoir model). The model dimensions and orientation of the computer program are the same as the 2D arithmetic average maps because the input data for the computer program was the numerical data extracted from these 2D average maps. The computer program efficiently correlated all the production parameters and results of the pressure saturation inversion to produce the final permeability estimates shown in the figure below.
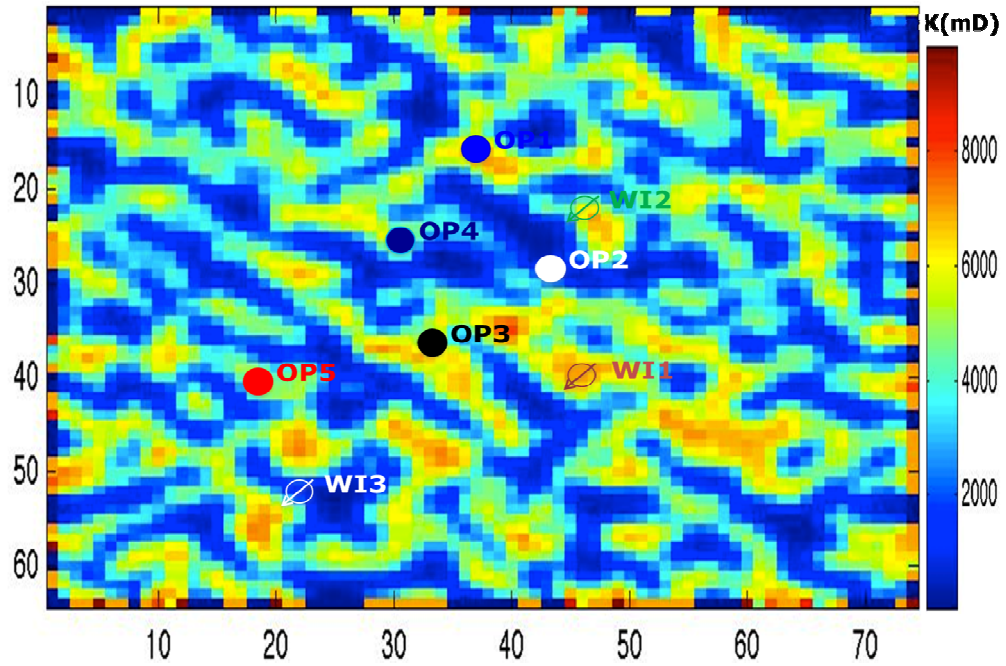
Figure 38: Permeability estimates obtained through the approach proposed by the project

The new permeability estimated in Fig 38 appear to have preserved some features of the initial model such as high permeability values around the producer wells; nevertheless, instead of high permeability concentrated at the centre of the field such as the initial model (fig 31), the new estimates appear to display permeability channels trending NW-SE and NE-SW of the field. Furthermore, the computed permeability displays patterns comparable to the behaviour of highly sinuous meandering rivers with avulsion features episodic sedimentation characteristic of the turbiditic deposits from Dalia Field.

5.2 Application to synthetic data

Using a synthetic dataset from a UK field, the approach proposed in *section 4.1.2* was used to test the methodology on a reservoir producing oil and water. The synthetic data includes a simplistic initial permeability distribution consisting of high values in the crest and low ones on the rest of the field (fig 39). To generate permeability results that incorporate 4D seismic data and production data, a computer program was created using the formulation in *equation 4-3*; the computer program used a Cartesian grid consisting of 100 x 100 x 1 cells, the initial permeability model, fluid flow information, average pressure information, mobility data and an initial saturation model (fig 40). The seismic base-line and monitor surveys are spaced 3 years apart being *T0* the time of the baseline survey, 2003 and *T1* time of the monitor survey, 2006. For these times of investigation

production data from the synthetic field was available and was used to update the initial permeability model, an attempt to check whether the new formulation could bring some detail information related to the field, in spite of the simplistic initial permeability model.

The production configuration consists of two producers (P1 and P2) and one injector (I) placed strategically to maintain the pressure and balance the production flow-rates. Through pressure-saturation inversion, changes in the 4D seismic signatures were related to changes in pressure/saturation of the reservoir fluids; the pressure-saturation inversion follows the model proposed by MacBeth *et al,* (2005).
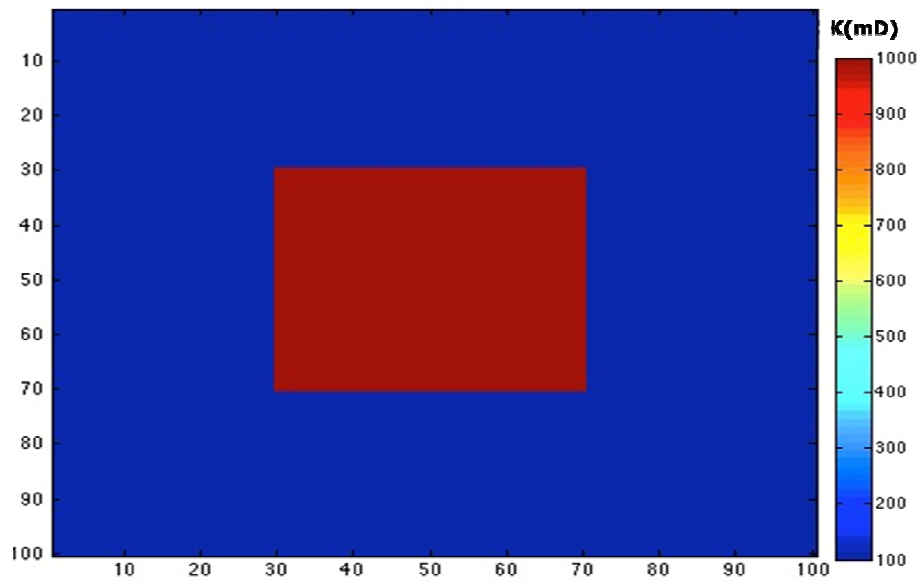
Figure 39: Initial distribution of permeability showing high permeability values in the centre of the field. The proposed approach was used to test whether incorporating seismic and production data can correct this un-realistic permeability distribution.

In Fig 39*,* the permeability at the centre of the field was set at 1000 mD and 100 mD in the rest of the field (matrix norm of 4.17×10^4 D). The combined production rate of oil and water was set at constant 744.03 bpd.

For the distribution of the initial saturation at T0, the irreducible water saturation was set at 15% while the irreducible oil saturation was set at 20%, the viscosity of the water was set at 0.4 Pa.s and 3.2 Pa.s for oil. Fig 40b shows the plot oil and water relative permeability as a function of water saturation at T1. The irreducible water saturation set by the project differ from those in fig 40 results because the process of converting 3D into 2D has the effect of lowering absolute values, an uncertainty considered (*tables 8 & 9*).

 Figs 40a & 40b, show that in response to production, after 3 years the waterfront moved diagonally towards the producer at the centre of the field, the differential

pressure between the reservoir and the surface, natural reservoir pressure and the water injection strategy in place causes the movement of the waterfront along the flow-lines. For this reservoir during the time of inspection the drive mechanisms include a combination rock compaction, and water drive.
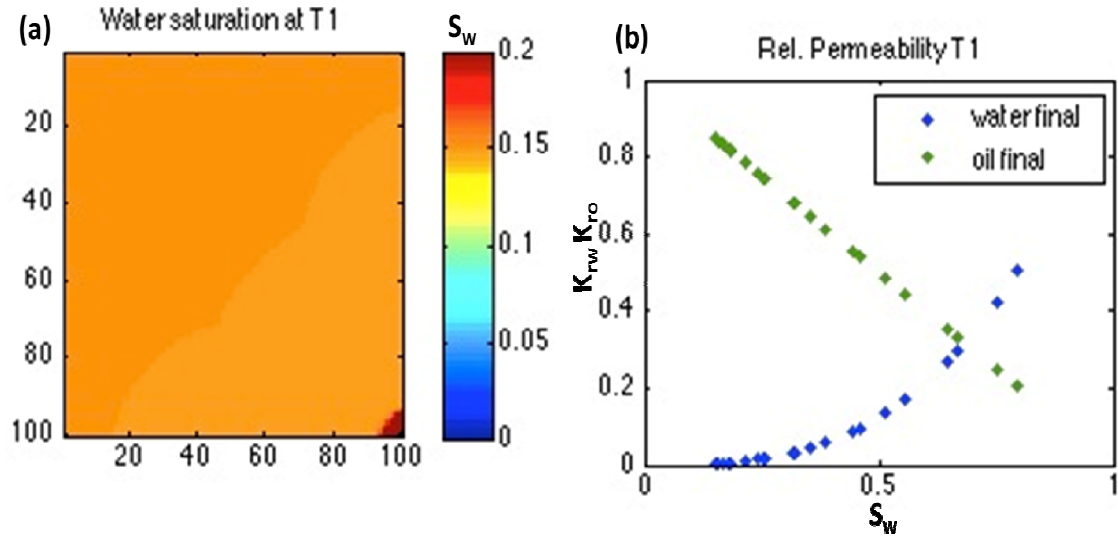
Figure 40: (a) Distribution of water saturation at time T1. **(b)** Oil & Water relative permeability vs. water saturation at time T1

From *T0* to *T1*, the difference in the norms of the water saturation is 1.76, this value implies that the water saturation has actually increased between *T0* to *T1*; production causes water to replace oil following the law $So = 1 - Sw$, this creates an inverse relationship between the saturation of oil and that of water, hence the oil saturation decreases in the magnitude of the increase in the water saturation.

The distribution of the reservoir pressure at time *T0* was constant with the matrix norm of 4.51×10^5 Pa, analysis of the Laplacian of the pressure was performed by investigating the partial variability of the reservoir pressure in the x and y directions respectively. Fig 41a shows the distribution of the reservoir pressure at time *T1* with the matrix norm of 4.50x105 Pa, from the figure, the pressure appears to be highest at the bottom-right corner of the field, gradually decreasing with a radial pattern reaching lowest values at the top-right corner of the field. Using the bicubic spline interpolation approach (Salkauskas, 1984) the gradient and magnitude of the gradient for the pressure at *T1* was estimated to access the degree of variability of the pressure in the x and y directions (figs 41b & 40c); according to (fig 41c), the magnitude of the pressure at *T1* is constant, being constant where the initial permeability is highest (centre of the field), and maximum at the bottom-right and top-left corners of the field; this information is useful establishing that the higher disturbances of pressure were mapped around

the producers, resulting from a good injector performance from the injector located at the centre of the field.
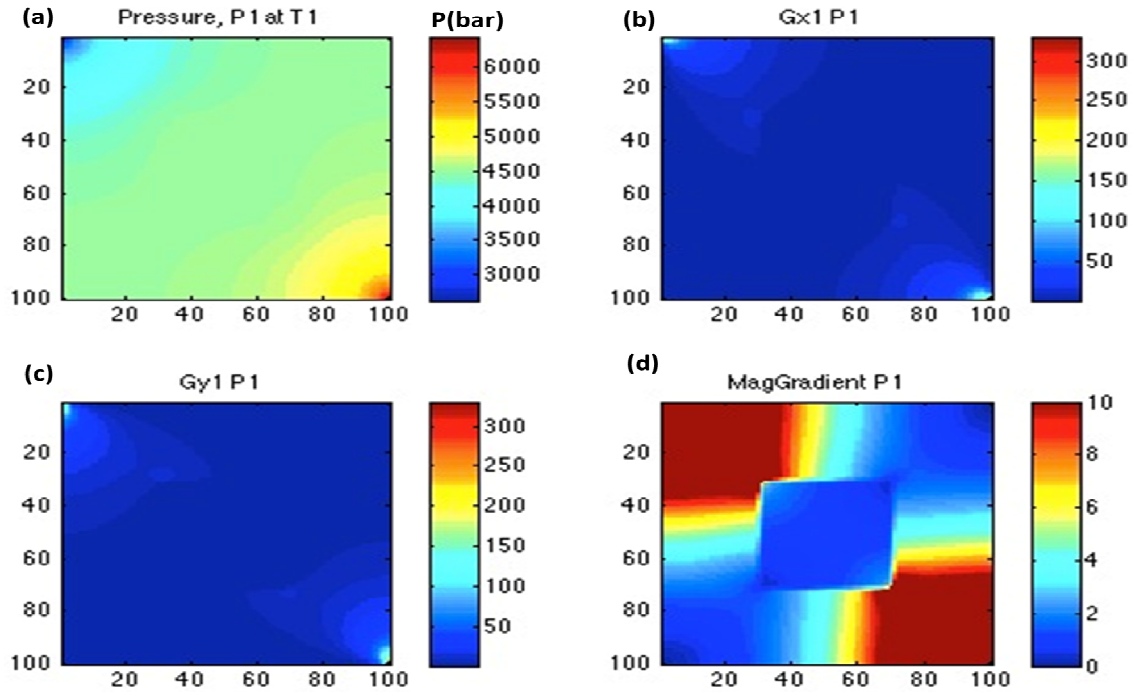
Figure 41: (a) Final reservoir pressure at time T0. **(b)** Distribution of final pressure in the x-direction. **(c)** Distribution of final pressure in the y-direction. **(d)** Laplace of the final pressure.

The changes in reservoir pressure (∇P) between *T0* and *T1* were estimated and they display a matrix norm of 2.07×10^4 Pa (fig 41a). Since the norm of a matrix can be used to denote the magnitude of such matrix (*appendix C*), it was assumed that the norm of this matrix is qualitative estimation of the differences between the two pressure distributions.

The distribution of ∇P in the *x* and *y* directions was estimated and (figs 41a & 41b) respectively, both distributions show that the pressure does not change at the centre of the field, being the main disturbances around the producers; the magnitude of the pressure gradient mapped in (fig 41c) shows similar behaviour to that of the pressure a *T1*. A relationship between the 4D seismic signature and production data shows that where the changes in pressure and saturation are high in response to production, dimming or brightening patterns of the seismic attributes are expected to agree at least with the seismic inversion technique.
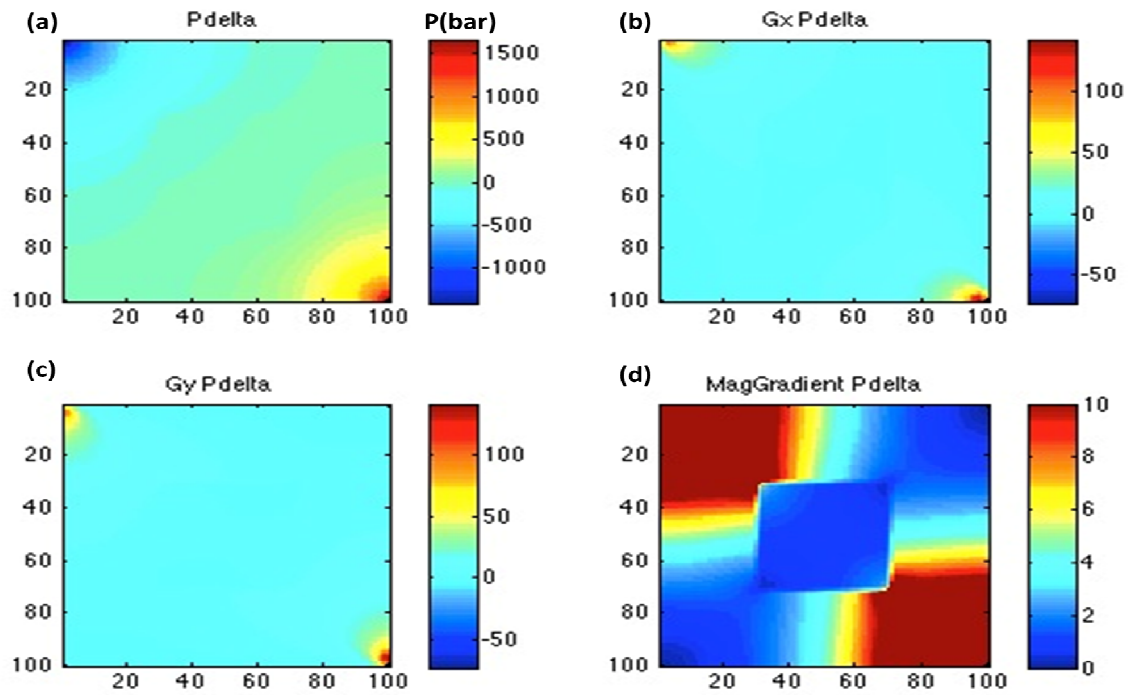
Figure 42: (a) Difference between initial pressure at T0 and final pressure at T1. **(b)** Distribution of the pressure difference in the x-direction. **(c)** Distribution of the pressure difference in the y-direction. **(d)** Laplace of the of the pressure difference.

The proposed approach was successfully used to estimate permeability using the 4D seismic and production data; the results produced by the approach (fig 43) show high permeability values that are no longer restricted to the centre of the field (fig 39), instead the new permeability stretches N-S in the western part of the field, also, the norm of the new estimates is 4.24×10^4 opposed to 4.16×10^4 of the initial permeability.
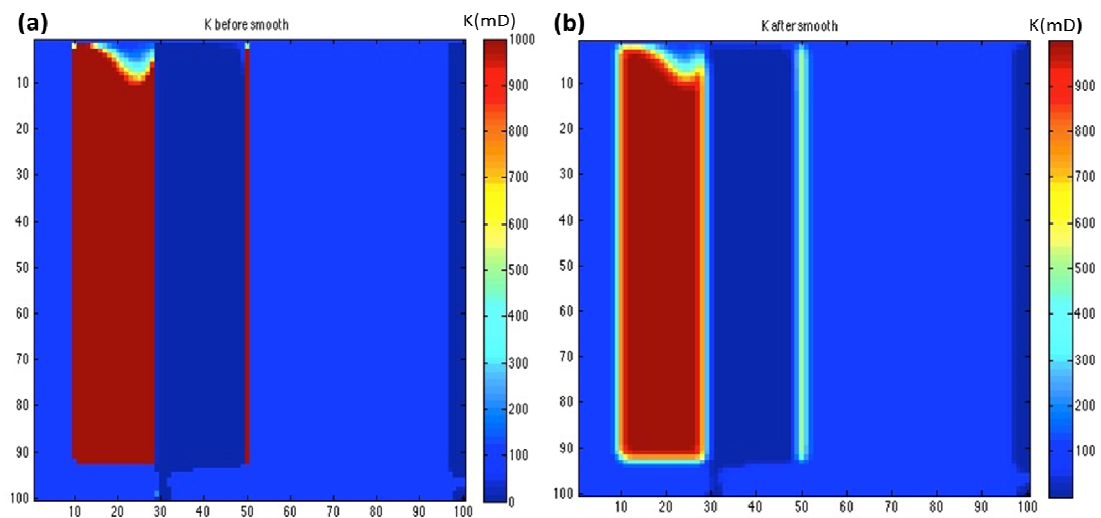
Figure 43: (a) Updated permeability map before regularization. **(b)** Updated permeability map after using the regularization technique proposed in 4.2.

85

The results provided by the synthetic approach in Figs 43a and 43b do not appear to provide a very realistic scenario; however, the elongated shape of the permeability estimated by the approach can be more easily linked to geological features that than the initial permeability distribution with high results in the centre. Despite the fact that easy comparison cannot be made between the initial and the updated permeability estimates, the distribution of the new estimates incorporates changes in 4D seismic signatures encapsulated in the distribution of the pressure and saturation.

Therefore, considering that production data and seismic data from a field are available the approach can be used to reflect that information regardless of the initial distribution of the permeability.

CHAPTER 6   CONCLUSIONS, UNCERTAINTY AND RECCOMENDATIONS

Overview

This thesis investigates the development and implementation of an alternative approach to estimate permeability using 4D seismic and time-lapse production data. The complete approach resulted from an effective integration of investigation of mathematical, simulation, computer and reservoir modelling techniques. This chapter summarizes the findings of the project with relevant conclusion of the study.

Uncertainty is analysed and potential improvements of the work are outlined by the recommendations.

6.1 Conclusions

The 3D reservoir model that was built successfully integrated field data from the Dalia Field to investigate the behaviour of reservoir rock properties/parameters, using 4D seismic, well log data and production information. The model was effectively used to produce spatial and temporal distribution of the reservoir rock properties relevant to the numerical approach (pressure, saturation, GOR, porosity, fluid flow rate, initial saturation and initial permeability). The mathematical and numerical approach here developed were successfully used to estimate the horizontal permeability using 4D seismic and production data from the Dalia Field, however the choice of probabilistic approach provided little means to quantitatively estimate uncertainty. Results produced by the approach display features correlatable to the nature of the Dalia Field reservoir in addition to a producing more detailed distribution of the permeability and better estimates.

Thorough the course of the project some lessons were learnt, among these lessons the most important include:

- Attributes can be used to show fluid substitution, increase in water content was directly proportional to P-wave velocity, while increase in pore pressure was inversely proportional to P-wave velocity; changes in the P-wave velocity can be computed through pressure-saturation inversion through which final saturation may be estimated.

- Stochastic modelling proved to be an invaluable tool to estimate the inter-well property distribution and one of the few ways for controlling the

uncertainty through equiprobable realizations of data using variogram, anisotropy range and orientation.

- Difficulties associated with the estimation of initial permeability and saturation models can be minimized by using reservoir engineering standards and available theoretical models such as equations that estimate permeability using well log data and measurable rock properties. The uncertainty associated with the choice of saturation parameters and permeability were accessed and reduced by establishing *best, worst and most likely scenarios.*

- The interpretations based on the 3D model are deeply constrained by the seismic data; using well log data to calibrate the interpretations reduced such limitations. Prior to 3D modelling or performing any numerical simulations time was spent using statistical, analytical and research techniques to gain an understanding of the most sensitive parameters/factors influencing the model; once this was done it was remarkable the extent to which the modelling process became an intuitive process.

- The 3D model of the Dalia Field, numerical data and interpretations within the project agrees with information found in the published literature (Caie, et al., 2007; Vemba, et al., 2011; Prat, et al., 2010). Most attention was dedicated to describing the steps involved with the extraction of numerical information from the 3D model and 2D average properties; much less information was given to the intricate mathematical operations and processes involved in building the 3D model.

In conclusion, *successful integration of reservoir parameters into the Dalia Field 3D model combined with the advanced inversion techniques applied to 4D seismic enabled the extraction of numerical data with which an initial permeability model was improved through 4D seismic reservoir simulation. The detailed information contained in the distribution of the horizontal permeability results obtained by the approach here proposed proved that the information encapsulated into seismic can be successfully used for quantitative purposes.*

The added value of the current approach is the fact that the methodologies here developed can adapt to different reservoir scenarios and within the inversion techniques, the pressure and saturation are not dealt with separately. Furthermore,

the same way the differential equations were manipulated to isolate the permeability in the numerical model (*chapter 4*), these equations can be used to estimate any other parameter or reservoir property of interest.

6.2 Uncertainty and limitations

The limitations, uncertainty and errors associated with modelling the physical reality make the theoretical equations less reliable. Nevertheless, reservoir engineers should take the opportunity of applying the useful technique of simulation followed-up by simple analytical procedures for saving time, without sacrificing accuracy in generating useful results (Dake, 2001).

The results produced by the proposed approach using Dalia Field data and the 3D model are heavily constrained by the initial permeability and saturation models in addition to the reservoir and petrophysical parameters; uncertainty and limitations associated with these are undoubtedly reflected on the estimates produced by the approach. Accurate estimation of the reservoir parameters involved in the equation is crucial for building a realistic 3D model because their spatial and temporal variation ultimately affects the outcome of permeability estimation; therefore, the approach proposed here is limited by the choice of reservoir modelling and fluid characterization techniques, be it the 3D reservoir model or the choice of the stochastic approach used to populate data across the field to fill the inter-well spacing. The uncertainty associated with initial permeability and saturation models was minimized by the used of 3 scenarios for each from where the *best case, more likely and worst case scenario* were defined (*tables 8 & 9*).

Table 8: statistical information of saturation extracted from the reservoir model using different petrophysical parameters

Case	Value	Saturation (%)		Saturation parameter
		3D	2D	
1	Max	40.0	9	m = 1.7
	Min	5.0	0.5	n = 1.3
2	Max	30	100	m = 2
	Min	2.5	15.0	n = 2
3	Max	30	100	m = 3.2
	Min	2.5	15.0	n = 2.6

Table 8 only shows the maximum and minimum values of saturation, spatial variability of the property is illustrated by Figs 17a to 17c; the table also show high variability between 3D and 2D domains, this is due to the fact that the 2D domain was achieved by the arithmetic average of all the reservoir layers.

Table 9: Maximum and minimum numerical information of permeability estimated using different empirical models. True distribution of the property is illustrated by Figs 19a to 19c

Case	Value	Permeability (mD)		Theoretical Model
		3D	2D	
1	Max	7422	5500	Timur
	Min	4384	4700	
2	Max	2805	2604	Coates
	Min	2479	2515	
3	Max	5139	4559	Tixier
	Min	4228	4324	

Tables 8 and 9 respectively illustrate the uncertainty derived from the use of different saturation parameters and uncertainty from the use of different models to estimate the initial permeability. Both Tables 8 and 9 show a large difference between the 2D and 3D values, this is explained by the fact that the 3D values in each case represent the true distribution of the mapped property in the 3D model while the 2D values account for the arithmetic average of the 3D distribution of those properties. Table 9 allows some appreciation of the uncertainty using the 3D domain and 2D domain; values in the 3D domain are about 26% greater than those on the 2D (*table 9, case 1*). Furthermore the deviation from the field reported permeability and the one estimated using Timur approach ranges -2% to 8 %, minimization of this deviation is still required. For saturation the uncertainty in much higher between the different cases, and the lack of core data and saturation information made it difficult to minimize this uncertainty.

Pressure saturation inversion techniques were used to extract numerical data from seismic; however, these procedures are not straightforward due to non-uniqueness problems. The uncertainty associated with the noise on the seismic data is transferred to the interpretations and the numerical data obtained from it. Therefore, it important to analyse the impact of the uncertainty inherent from seismic inversion tools on the reservoir properties and decide on the range of risk acceptable for the numerical information obtained through these techniques.

A probabilistic approach (stochastic) was used to incorporate production and petrophysical data into the 3D model. The approach allowed the generation of equiprobable realizations of the data to control the uncertainty (fig 15). Several stochastic algorithms exist and in theory they can be used to produce distribution of any parameter by relating model parameters to observable ones; however, in reality the choice of appropriate stochastic algorithm can only be defined through

stochastic analysis to investigate the impact of structural uncertainties associated with the stochastically populated reservoir and petrophysical parameters.

To minimize uncertainty several stochastic algorithms were used and the one that best represents the field data was chosen (fig 13); furthermore, the project used multi-point statistics to generate training images (fig 14) used to incorporate geological continuity information to the 3D model by means of variogram information, therefore minimizing the uncertainty.

With limited well control, the structural uncertainty derived from the seismic interpretations, uncertainty with respect to fault geometry and well locations can have the most impact on the flow performance for turbidite reservoirs such as Dalia Field, fault interpretations were not produced because of the time-frame of the project and the fact that the model did not require flow simulation. Nevertheless, it is always important to consider faults in any model because their interpretation affects the analysis of reservoir heterogeneity and connectivity.

The resolution of the 3D grid (100x100) and the difference between the well log data and the up-scaled well log data imposed visualizations and interpretation limitations; these were limitations in terms of software and computational power that potentially add uncertainty to the model however, this was the only way to produce faster simulation given the time and available computational power.

Due to the nature of seismic data acquisition, where a set of post-processing techniques are used before its final product, reservoir descriptions and model-derived geological interpretations of this project are constrained by the quality of seismic data and input data for the model. Although the amount of data collected using the latest and greatest high-tech equipment in each well might not the best, it might be the lowest quality data that will ever be acquired during the lifetime of the field because this data could have been collected under purely static conditions.

6.3 Recommendations and further considerations for improvement of the proposed approach

The approach proposed by the project was initially designed to be tested with the Horn mountain field in the Gulf of Mexico; however the lack of a monitor seismic survey made it impossible to fully implement the approach and led to the acquisition of Dalia data-set. The amount of data available for the two fields is incomparable considering that the Horn Mountain Field has more available core data whilst the Dalia Field has seismic data of superior quality. The change in the data set changed some of the initial objectives of the project and consequently, particular problems could not be explored as initially intended. Based on the initial plan the project recommends the following aspect to complement this project:

6.3.1 Reservoir modelling and simulation

The outcome of the results produced by the proposed approach is heavily dependent on the 3D reservoir model built during the course of the project. This model used seismic data and well log and PVT data with the primary objective of mapping the distribution of the reservoir parameters necessary for the numerical approach; accurate interpretation of the time-lapse seismic signature data could improve understanding of these parameters, therefore appropriate 3D modelling should be performed by a multi-disciplinary team involving geoscientists, reservoir engineers, geologists and geophysicists.

6.3.2 Property modelling using 4D seismic

The new approach proposed by the project to estimate reservoir permeability using 4D seismic and production data produced encouraging results when applied to real data; however as all new discoveries the approach needs to consider the factors that might affect its robustness and reliability of the results, such factors include: Development of techniques to reduce noise from seismic and 4D seismic attributes as these affect the permeability results; the use of more than 2 seismic surveys for the attribute analysis as it could potentially help creating mechanisms of accessing and reducing the error in the amplitude shifts

6.3.3 Economic considerations

The economic implications of the approach should be analysed through history matching, reservoir flow simulation and economic projections; doing so will assess the potential value of the information produced by the approach and explore gateways to reduce its limitations. The project economics could be performed through decision trees where the risk, cost and revenue associated with the project results would be appreciated.
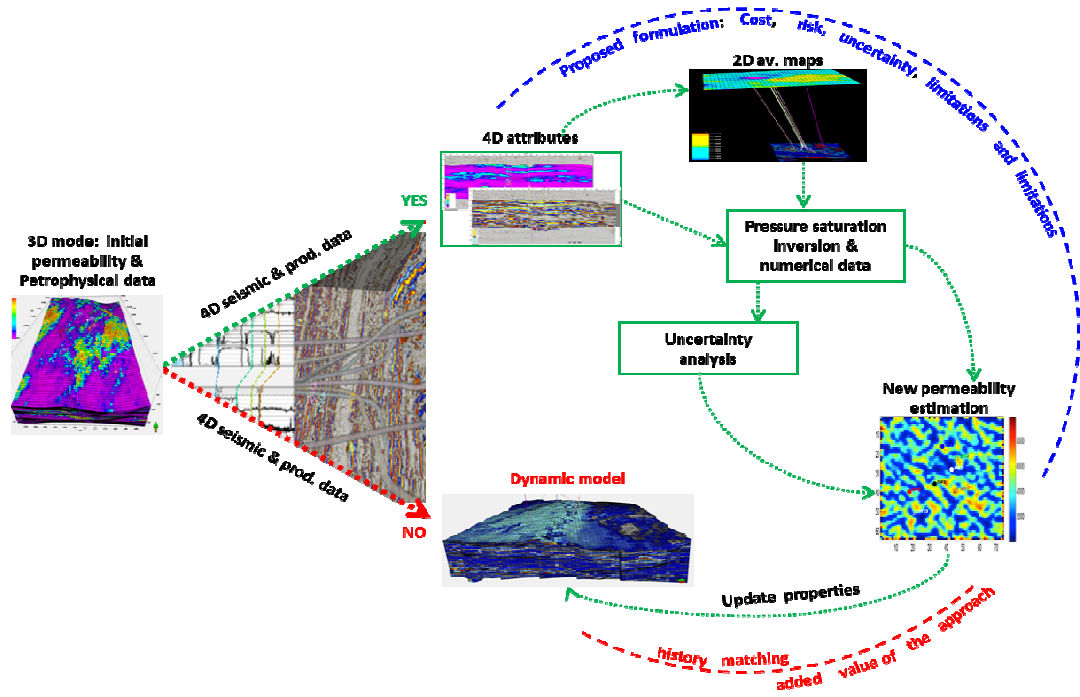
Figure 44: Economic considerations of the potential value that can be added by using the results produced by the proposed methodology with reservoir simulation and history matching.

6.3.4   Integration of results produced by the approach into 3D models

The robustness of the proposed approach could be improved though integration of the 2D permeability maps into 3D static or dynamic models. An extension of the present work would include the development of techniques that effectively integrate the 2D results produced by the approach into 3D models. These techniques should provide mechanisms for extracting the detailed information within the permeability results and input the information into the 3D models to produce vertical estimates in addition to the horizontal ones.

6.3.5   Use of the results produced for reservoir simulation and history matching

One of the ways to inspect whether the proposed approach can potentially add value to conventional techniques would consist of using the results produced by the approach and feeding them into a simulation model together with the production data (PVT and petrophysical data) and the 3D geocellular model. Through history matching the results of the simulations would be compared with observed data to inspect whether the proposed approach can be used to improve the recovery factor, which in turn could improve the amount of hydrocarbons and revenues associated with the increase in recovery factor.

CHAPTER 7   REFERENCES

Abou-Kassem, J., Ali, S., & Islam, M. (2006). *Petroleum Reservoir Simulation - A Basic Approach.* Houston: Gulf Publishing Company.

Ahmed, T. (2010). *Reswervoir Engineering handbook* (4 ed.). Elsevier.

Ahmed, U., Crary, S., & Coates, G. (1989). Permeability estimation: various sources and their interrelationships. *SPE Annual Technical Conference and Exhibition*, *SPE 19604.* San Antonio, Texas USA.

Ali, S., & Thomas, S. (2000). Enhanced Oil Recovery - What We Have Learned. *Society of Petroleum Engineers , 39* (2), 7-10.

Archie, G., & Shell Oil, C. (1942). The Electrical Resistivity Log as an Aid in Determining Some Reservoir Characteristics. *146* (1), 54-62.

Aremu, M. (2000). *Oil and Gas Online*. Retrieved Mrch 1, 2012 from http://www.oilandgasonline.com/article.mvc/Deepwater-Fields-Define-Angolas-Oil-Wealth-in-0001

Aziz, K., & Settari, A. (1979). *Petroleum Reservoir Simulation.* New York: Elsevier.

Aziz, K., & Settari, A. (1990). *Petroleum Reservoir Simulation.* Elsevier: Science Publishing Co.

Barsky, B. (1984). Exponential and polynomial methods for applying tension to a interpolation spline curve. *27* (1), 1-18.

Benerjee, S., Gelfand, A. E., & Carlin, B. P. (2004). *Hierarchical Modeling and Analysis for Spatial Data.* Chapmann & Hall/CRC.

Biot, M. (1956). Theory of propagation of elastic waves in a fluid saturated porous solid. I. Low frequency range and II. Higher-frequency range. *Journal of Acoustical Society of America* , Vol 28, 168-191.

Brooks, R., & Corey, A. (1964). Hydraulic properties of porous media: Hydrology Papers.

Buckley, S. E., & Leverett, M. C. (1942). Mechanism of fluid displacement in sands. *146, 107-116*.

Caie, D., Casse, E., & Elias, B. (2007). *Dalia Development - Subsurface and well completions engineering* (18539 ed., Vol. OTC 18539). Houston, Texas: Offshore technology conference.

Cheng, A., & Cheng, D. T. (2005). Heritage and early history of bounday element method. Engineering asnalysis with boundary elemen. 268-302.

Clark, I. (1979). *Practical Geostatistics.* Applied Science Publishers Ltd.

Coates, G., & Dumanoir, J. (1974). A new approach to improve log-derived permeability. *The log analyst , 15* (1), 17-31.

Coats, G., & Dumanoir, J. (1947). A New Approach to Improved Log-Derived Permeability. 17.

Craft, B., & Hawkins, M. (1959). *Applied Petroleum Reservoir Engineering.* Englewood Cliffs, N.J: Prentice-Hall.

Cressie, N. (1993). *Statistics for Spatial Data.* New York: Wiley.

Dahlquist, G., & Bjрck, A. (2003). *Numerical Methods.* New Jersey: Prentice_Hall.

Dake, L. (1978). *Fundamentals of reservoir simulation.* Amsterdam, The Netherlands: Elsevier.

Dake, L. (2001). *The practice of reservoir engineering* (2 (revised) ed.). Amsterdam: Elsevier.

Djebbar, T., & Donaldson, E. (2003). *Petrophysics theory and oractice of measuring reservoir rock and fluid transport properties* (2 ed.). Elsevier.

Engl, H. W., Hanke, M., & Neubauer, A. (1996). *Regularization of Inverse problems (* (Vol. Series No. 375). Dordrecht, Boston, London: Kluver Academic Publishers: Mathematicas and Applications .

Fanchi, J. (2001). *Principles of Applied Reservoir Simulation 2 ed.* Houston, Texas, USA: Gulf Professional Publishing.

Fanchi, J. (2001). Time-lapse seismic monitoring in reservoir managemen. *The Leading Edge* , Vol 20, No. 10, 1140-1147.

Fang, S., & Tsao, J. (1996). A Dual Perturbation View of Linear Programming. Mathematical Methods of Operations Research. *Mathematical methods of operations research* , Vol 44, 1, 1-9.

Gassman, D. (1977). *Fundamentals of numerical reservoir simulation.* Amsterdam: Elsevier.

Golub, G. H., & Van Loan, C. F. (1996). *Matrix computations 3rd ed.* Bartimore and London: The Johns Hopkings University Press.

Gonzalez-Rodrighez, P., Kindelan, M., Moscoso, M., & Dorn, O. (2005). History matching problem in reservoir engineering using the propagation back-propagation method. (21 565-590).

Gordon, W. (1969). Spline-blended surface interpolation through curve networks. *18* (10), 931-952.

Gouveia, W., Johnston, D., Solberg, A., & Lauritzen, M. (2004). Jotun 4D: Characterization of fluid contact movement. *The Leading Edge* , Vol 23, No. 11, 1187-1194.

Groetsch, C. W. (1993). *Inverse Problems in the mathematical sciences.* Braunschweig: Vieweg.

Hanna, C., Gray, D., Fink, T., Mitchell, D., Jose, B., & Willott, D. (2011). Geophysical Applications – Using Geophysics for Hydrocarbon Reserves and Resources Classification and Assessment. *Canadian Society of Exploration Geophysicists* , 2-44.

Harting, J., Chin, J., & Coveney, P. (2005). *Large-scale lattice Boltzmann simulations of complex fluids: advances through the advent of computational grids*. Retrieved March 28, 2012 from

http://www.google.co.uk/imgres?q=immiscible+fluids&start=297&hl=en&sa=X&biw=1920&bih=976&tbm=isch&prmd=imvns&tbnid=wJTENO6t_VUWWM:&imgrefurl=http://www.ica1.uni-stuttgart.de/~jens/pub/05/05-PhilTransReview.html&docid=547N5AteaX9JSM&imgurl=http://www.icp.u

Huang, X. (2001). Integrating time-lapse seismic with production data: A tool for reservoir engineering. *The Leading Edge* , Vol 20, No. 10, 1148-1153.

John, A. K., Lake, L. W., Torres-Verdin, C., & Srinivasan, S. (2008). Seismic Facies Identification and Classification Using Simple Statistics. *SPE Reservoir Evaluation & Engineering , 11* (6), 984-990.

Kearey, P., Brooks, M., & Hill, I. (2002). *An introduction to geophysical exploration 3rd ed.* Oxford: Blackwell Science.

Kellkar, M., & Perez, G. (2002). *Applied Geostatistics for Reservoir Characterization.* Texas: Society of Petroleum Engineers.

Kozeny, J. (1927). Soil permeability. 136-306.

Landro, M. (2001). Discrimination between pressure and fluid saturation changes from time-lapse seismic data. *Geophysics, Soc. of Expl. Geophys* , Vol 66, 836-844.

Lapeyrouse, N. (2002). *Formulas and Calculations for Drilling, Production and Workover, 2nd Ed.* Elsevier.

Lopez, M. (2001). Architecture and depositional pattern of the quaternary deep-sea fan of the amazon. *Marine and Petroleum Geology* (18), 479-486.

MacBeth, C., & Al-Maskeri, Y. (2006). Extraction of permeability from time-lapse seismic data. *Geophisical prospecting* , Vol 54, 333-349.

Marsh, M., Parr, R., & Griffin, T. (2000). Interpretation And Integration of 4-D Results Into Reservoir Management, Schiehallion Field, UKCS. *Society of Exploration Geophysicists* , 1-4.

Mattax, C., & Dalton, R. (1990). *Reservoir simulation, SPE Monograph.* Texas: Society of Petroleum Engineering.

Mavko, G., Mukerji, T., & Dvorkin, J. (1998). *The Rock Physics Handbook: Tools for seismic analysis in porous media:.* New York: Cambridge University Press.

Mindlin, R. D., & Deresiewicz, H. (1953). Elastic spheres in contact undervarying oblique forces. *Journal of Applied Mechanics-Transactions of the ASME , 20* (3), 327-344.

Molnar, D., Aminian, K., & Ameri, S. (1994). The use of well log data for permeability estimation in a heterogeneous reservoir. (29175).

Natterer, F. (2001). *The mathematics of computerized tomography (Classics in Applied Mathematics)* (Vol. 32). Philadelphia: Society for Industrial and Applied Mathematics.

Oil&Gas, A. (2012). *Angola Oil and Gas Map Concessions Blocks - Soft Edition*. Retrieved March 08, 2012 from http://africa-oil-gas.com/angola_oil_and_gas_map_concessions_blocks_soft_edition-1448-1-2-c.html

Peaceman, D. (1977). *Fundamentals of numerical reservoir simulation.* Amsterdam, The Netherlands: Elsevier.

Peaceman, D. (1978). Interpretation of Well-Block Pressure in Numerical Reservoir Simulation. *SPE paper 6893* , 183-194.

Picard, D., Thebault, J., Goncalves, F., & Costa, R. (2007). *The Dalia Development Challenges and Achievements* (18538 ed.). Texas: Offshore Technology Conference.

Prat, P., Clark, S., Lescanne, H., Manivit, T., Turpin, P., Vert, M., et al. (2010). 4D added value in reservoir model construction – A case study offshore Angola. *SEG* (1332), 1-4.

Read, T., & Cressie, N. (1988). *Goodness-of-Fit Statistics for Discrete Multivariate Data.* New York: Springer.

Salkauskas, K. (1984). C1 splines for interpolation of rapidly varying data. *14* (1), 239-250.

Schatzinger, R., & Jordan, J. (1999). *Reservoir characterization: recent advances.* AAPG.

Schlumberger. (2009). Petrel 2010 Software reference manual. Schlumberger.

Schlumberger. (2009). *Petrel Introduction course manual.* Schlumberger.

Seba, R. (1998). *Economics of worldwide petroleum production.* ulsa, Oklahoma: Oil and Gas Consultants International Publications.

Sheldon, J. W., Harris, C. D., & Bavly, D. (1960). A method for general reservoir behavior simulation on digital computers. *SPE 1521-G* , 2-5.

Stephen, K., Soldo, J., MacBeth, C., & Christie, M. (2006). Multiple-Model Seismic and Production History Matching: A Case Study. *Society of Petroleum Engineers* , *11* (4), 418-430.

Strebelle, S. B. (2002). Conditional simulation of complex geological structures using multiple point statistics. *1-22* (34).

Strebelle, S. B., & Jounel, A. G. (2001). Reservoir modelling using Multi-Point Statistics. (71324).

Stroud, K., & Booth, D. (2007). *Advanced Engineering Mathematics* (7 ed.). Palgrave Macmillan.

Taner, M. (1994). Seismic Attributes Revisited.

Taner, M. T. (1992). Seismic attributes revisited.

Thomas, G. W. (1982). *Principles of Hydrocarbon Reservoir Simulation,.* Prentice-Hall.

Timur, A. (1968). An Investigation of Permeability, Porosity, and Residual Water Saturation Relationship for Sandstone Reservoirs,. *9* (4), 8.

Timur, A. (1969). Pulsed NMR studies of porosity, movable fluids and permeability of sandstones. *Journal of Petroleum Technology* , VOl 21, 775-786.

Tixier, M. (1949). Evaluation of permeability from electric - log resistivity gradients. *48* (6), 113.

Vasco, D. M., Yoon, S., & Datta-Gupta, A. (1999). Integrating Dynamic Data Into High-Resolution Reservoir Models Using Streamline-Based Analytic Sensitivity Coefficients. *SPE* , 4 389-399.

Vasco, D. W. (2000). An algebraic formulation of geophysical inverse problems. *Geophysics* , Vol 142, 970-990.

Vasco, D., Datta-Gupta, A., Behrens, R., Condon, P., & Rickett, J. (2004). Seismic imaging of reservoir flow properties: Time-lapse amplitude changes. *Geophysics* , Vol 69, 1425-1442.

Vemba, J., Cunha, F., Brechet, E., France, P., Maultsch, S., & Toinet, S. (2011). *4D Monitoring: Example of 4D Interpretation in Lower Flanks systems, Dalia - Angola* (81 annual meeting conference ed.). Texas: SEG.

Vesnaver, A., Accaino, F., Bohm, G., Madrussani, G., Pajchel, J., & Rossi, G. a. (2003). Time-lapse tomography. *Geophysics* , Vol 68, 815-823.

Vogel, C. R. (2002). *Computational Methods for Inverse Problems.* Philadelphia: Society of Industrial and Applied Mathematics.

Willhite, G. (1986). *Waterflooding* (Vol. 3). Texas: SPE.

Wyllie, M., & Rose, W. (1950). Some theoretical considerations related to the quantitative evaluation of the physical characteristics of reservoir rock from electrical log data. *Petroleum Transactions* , Vol. 189.

Wyllie, M., & Rose, W. (1950). Some Theoretical Considerations Related To The Quantitative Evaluation Of The Physical Characteristics Of Reservoir Rock From Electrical Log Data. *189*, 105.

CHAPTER 8   APPENDICES

A. Derivation of diffusivity equation one-phase, one-dimensional, linear horizontal flow

Considering a control box of volume AΔx
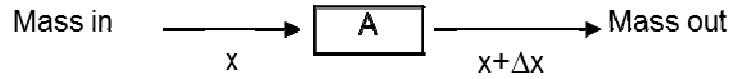
Figure 45-A: Diagram showing fluid displacement over a controlled volume

To derive the diffusivity equation we combine *mass conservation, rate equation and the equation of state.*

1) Conservation of mass:

Mass rate in $_x$ – Mass rate out $_{x + \Delta x}$ = Accumulation of mass

- Mass per unit volume = ρ
- Flux of mass per unit volume = ρv where v is the velocity
- Mass of fluid inside the box = $A\Delta x \phi \rho$

$$\rho v A \big|_x - \rho v A \big|_{x+\Delta x} = A\Delta x \phi \left(\frac{\rho_{t+\Delta t} - \rho_t}{\Delta t} \right)$$ (A-1)

Dividing by the volume (AΔx) and taking $\lim_{\Delta x \to 0, \Delta t \to 0}$

$$-\frac{\partial}{\partial x}(\rho v) = \phi \frac{\partial \rho}{\partial t}$$ (A-2)

2) Rate Equation:

Darcy's law is used to relate velocity to pressure gradient

$$v = -\frac{k}{\mu}\frac{\partial p}{\partial x}$$ (A-3)

 In case of non-horizontal flow, Darcy's equation takes the form

$$v_n = -\frac{k_n}{\mu_n}\left(\nabla p_n - \rho_n \nabla D \right)$$ (A-3a)

where n denotes the *oil* or *water phase*

Substitute (A-3) into (A-2) we get:

$$-\frac{\partial}{\partial x}\left(\frac{-k\rho}{\mu}\frac{\partial p}{\partial x}\right) = \phi\frac{\partial \rho}{\partial t}$$

(A-4)

3) Equation of state:

Since the fluids dealt with are compressible, the definition of isothermal compressibility is used to relate pressure with density.

$$c = -\frac{1}{V}\frac{\partial V}{\partial p}$$

(A-5)

where c is the compressibility, V is the volume and p is the pressure

It is known that $V = \frac{1}{\rho}$, substitute into (A-5):

$$c = -\rho\frac{d\left(\frac{1}{\rho}\right)}{d\rho} = \frac{\rho}{\rho^2}\frac{d\rho}{dp} = \frac{1}{\rho}\frac{d\rho}{dp}$$
    Hence:

$$c = \frac{1}{\rho}\frac{d\rho}{dp}$$

(A-6)

B. Reservoir engineering fundamental equations

B.1   Fluid flow equations

Reservoir simulation is used deduce the behaviour of real reservoirs by building theoretical models from which the performance those real reservoirs can be deduced and investigated. Within the reservoir immiscible fluids such as water, oil and gas co-exist together and mass transfer can be mathematically modelled (Dake, 2001). Model equations take into consideration all the forces acting in a reservoir, its heterogeneity and geometry. Using the Darcy's law and a simple material balance, a set of differential equations that describe the most complicated case of multidimensional, multicomponent, three-phase flow to model the displacement within porous medium were proposed by (Peaceman, 1997). These equations take the form

$$\nabla \cdot \left[\frac{\alpha \rho_o K k_{ro}}{\mu_o} \left(\nabla P_o - \rho_o g \nabla D \right) \right] + \alpha q_o = \alpha \frac{\partial \left(\phi \rho_o S_o \right)}{\partial t} \qquad \text{(B-1)}$$

$$\nabla \cdot \left[\frac{\alpha \rho_g K k_{rg}}{\mu_g} \left(\nabla P_g - \rho_g g \nabla D \right) \right] + \alpha q_g = \alpha \frac{\partial \left(\phi \rho_g S_g \right)}{\partial t} \qquad \text{(B-2)}$$

$$\nabla \cdot \left[\frac{\alpha \rho_w K k_{rw}}{\mu_w} \left(\nabla P_w - \rho_w g \nabla D \right) \right] + \alpha q_w = \alpha \frac{\partial \left(\phi \rho_w S_w \right)}{\partial t} \qquad \text{(B-3)}$$

The individual terms of the equations above are defined as:

$\nabla \cdot \left[\frac{\alpha \rho_o K k_{ro}}{\mu_o} \left(\nabla P_o - \rho_o g \nabla D \right) \right]$ rate of change of the oil flux with position

αq_o volumetric flow rate of oil produced, per unit reservoir volume [STB/BBL/S]

$\alpha \frac{\partial \left(\phi \rho_o S_o \right)}{\partial t}$ rate of change of the oil concentration with time

$\nabla \cdot \left[\frac{\alpha \rho_g K k_{rg}}{\mu_g} \left(\nabla P_g - \rho_g g \nabla D \right) \right]$ rate of change of the gas flux with position

αq_g volumetric flow rate of gas produced per unit reservoir volume [STB/BBL/S]

$\alpha \frac{\partial \left(\phi \rho_g S_g \right)}{\partial t}$ rate of change of the gas concentration with time

$\nabla \cdot \left[\frac{\alpha \rho_w K k_{rw}}{\mu_w} \left(\nabla P_w - \rho_w g \nabla D \right) \right]$ rate of change of the water flux with position

αq_w volumetric flow rate of water produced per unit reservoir volume [STB/BBL/S]

$\alpha \frac{\partial \left(\phi \rho_w S_w \right)}{\partial t}$ rate of change of the water concentration with time.

For convenience, the same o number of differential equation was used for flow with any number of dimensions, for that it was necessary to define as *geometric factor* here represented by the function α , which denotes:

one dimension: $\alpha(x, y, z) = A(x)$

two dimensions: $\alpha(x, y, z) = H(x, y)$

three dimensions: $\alpha\left(x,y,z\right)\equiv 1$

Equations (B-1 to B-3) were starting point for deriving the differential equations upon which the mathematical and numerical models of this project were based.

For a one-dimensional, horizontal, 3-phase oil, water and gas system, different versions of the above equations can be defined, in the form:

$$\frac{\partial}{\partial x}\left[\frac{Kk_{ro}}{\mu_o B_o}\frac{\partial P_o}{\partial x}\right]+q_o^{'}=\frac{\partial}{\partial t}\left(\frac{\phi S_o}{B_o}\right)\tag{B-4}$$

$$\frac{\partial}{\partial x}\left[\frac{Kk_{rg}}{\mu_g B_g}\frac{\partial P_g}{\partial x}+R_{so}\frac{Kk_{ro}}{\mu_o B_o}\frac{\partial P_o}{\partial x}\right]+q_g^{'}-R_{so}q_o^{'}=\frac{\partial}{\partial t}\left(\frac{\phi S_g}{B_g}+R_{so}\frac{\phi S_o}{B_o}\right)\tag{B-5}$$

$$\frac{\partial}{\partial x}\left[\frac{Kk_{rw}}{\mu_w B_w}\frac{\partial P_w}{\partial x}\right]+q_w^{'}=\frac{\partial}{\partial t}\left(\frac{\phi S_w}{B_w}\right)\tag{B-6}$$

The set of three equations above will be used interchangeably and with other industry equivalent for the derivation of the permeability equation.

B.2   Permeability estimation using real data

Based on the reservoir description and characterization in chapter 2, the reservoir fluids of the Dalia Field are under under-saturated flow conditions, in which case the free gas term in equation B-5 disappears so that the gas from solution can be re-written as:

$$\frac{\partial}{\partial x}\left[R_{so}\frac{Kk_{ro}}{\mu_o B_o}\frac{\partial P_o}{\partial x}\right]+q_g^{'}-R_{so}q_o^{'}=\frac{\partial}{\partial t}\left(R_{so}\frac{\phi S_o}{B_o}\right)\tag{B-7}$$

Adding equations B-4 & B-6 to equation B-7 it is obtained that:

$$\frac{\partial}{\partial x}\left[R_{so}\frac{Kk_{ro}}{\mu_o B_o}\frac{\partial P_o}{\partial x}+\frac{Kk_{ro}}{\mu_o B_o}\frac{\partial P_o}{\partial x}+\frac{Kk_{rw}}{\mu_w B_w}\frac{\partial P_w}{\partial x}\right]+q_g^{'}+q_o^{'}+q_w^{'}-R_{so}q_o^{'}=\frac{\partial}{\partial t}\left(R_{so}\frac{\phi S_o}{B_o}+\frac{\phi S_o}{B_o}+\frac{\phi S_w}{B_w}\right)$$
(B-8)

Rearranging and letting $Q=q_g^{'}+q_o^{'}+q_w^{'}$

$$\frac{\partial}{\partial x}K\left[R_{so}\frac{k_{ro}}{\mu_o B_o}\frac{\partial P_o}{\partial x}+\frac{k_{ro}}{\mu_o B_o}\frac{\partial P_o}{\partial x}+\frac{k_{rw}}{\mu_w B_w}\frac{\partial P_w}{\partial x}\right]+Q-R_{so}q_o^{'}=\frac{\partial}{\partial t}\left(R_{so}\frac{\phi S_o}{B_o}+\frac{\phi S_o}{B_o}+\frac{\phi S_w}{B_w}\right)$$
(B-9)

assuming that capillary pressure is neglected, $P_o = P_g = P_w = P$, and assuming that

$R_{so} = GOR$ then

$$\frac{\partial}{\partial x}\left[K\left(GOR\frac{k_{ro}}{\mu_o B_o} + \frac{k_{ro}}{\mu_o B_o} + \frac{k_{rw}}{\mu_w B_w} \right)\frac{\partial P}{\partial x} \right] + Q - GORq_o' = \frac{\partial}{\partial t}\left(GOR\frac{\phi S_o}{B_o} + \frac{\phi S_o}{B_o} + \frac{\phi S_w}{B_w} \right)$$

(B-10)

if we define $M_o = \dfrac{k_{ro}}{\mu_o B_o}$, $M_w = \dfrac{k_{rw}}{\mu_w B_w}$ and $q = GORq_o'$ then

$$\frac{\partial}{\partial x}\left[K\left(GOR.M_o + M_o + M_w \right)\frac{\partial P}{\partial x} \right] + Q - q = \frac{\partial}{\partial t}\left(GOR\frac{\phi S_o}{B_o} + \frac{\phi S_o}{B_o} + \frac{\phi S_w}{B_w} \right)$$

(B-11)

the equation above can be written in a more compact form

$$\nabla.\left[K\left(GOR.M_o + M_o + M_w \right)\nabla P \right] + Q - q = \frac{\partial}{\partial t}\left(GOR\frac{\phi S_o}{B_o} + \frac{\phi S_o}{B_o} + \frac{\phi S_w}{B_w} \right)$$

(B-12)

According to Fig 8, changes in GOR are relatively small and are assumed to be constant for simplicity, also considering that $\phi S_o + \phi S_w = 1$, equation (B-12) can be re-written as

$$\nabla.\left[K\left(GOR.M_o + M_o + M_w \right)\nabla P \right] + Q - q = 0$$

(B-13)

defining $\alpha = GOR.M_o + M_o + M_w$ we get

$$\nabla.\left[K.\alpha.\nabla P \right] = q - Q$$

(B-14)

In order to estimate the reservoir permeability using time-lapse changes, the above equation is considered in two distinct times, T_0 and T_1 subject to two boundary conditions Q_0 and Q_1, respectively, becoming:

$$\nabla.\left[K.\alpha_0.\nabla P_0 \right] = q_0 - Q_0$$

(B-15)

$$\nabla.\left[K.\alpha_1.\nabla P_1 \right] = q_1 - Q_1$$

(B-16)

Subtracting *equation (B-16)* from *(B-15)* it is obtained that:

$$\nabla.\left[K.\alpha_1.\nabla P_1 - K.\alpha_0.\nabla P_0 \right] = \left(q_0 - q_1 \right) - \left(Q_0 - Q_1 \right)$$

(B-17)

104

if we define

$$Q_\Delta = (q_0 - q_1) - (Q_0 - Q_1) \tag{B-18}$$

$$\Phi_0 = \alpha_0 . \nabla P_0 \tag{B-19}$$

$$\Phi_1 = \alpha_1 . \nabla P_1 \tag{B-20}$$

Using the 3 set of equation above, the *equation (B-17)* can be re-written as

$$\nabla . [K.\Phi_1 - K.\Phi_0] = Q_\Delta \tag{B-21}$$

using the approximation of the product rule for the ∇ operator, the equation above can be re-written as

$$\nabla K \cdot \Phi_1 + K \nabla . \Phi_1 - \nabla K \cdot \Phi_0 + K \nabla . \Phi_0 = Q_\Delta \tag{B-22}$$

for the finite approximations of the partial we will make use of the Newton's difference quotient in the form:

$$m = \frac{\Delta f(x)}{\Delta x} = \frac{f(x+h) - f(x)}{h} \tag{B-23}$$

where *h* is a small value that represents an approximation to the slope so that the derivative *f* at *a* is a function of the limit

$$f`(a) \lim_{h \to 0} = \frac{f(a+h) - f(a)}{h} \tag{B-24}$$

f'(a) represents one of the notations of the derivative to produce a linear approximation of the kind

$$f'(a) = \frac{f(a+h) - f(a)}{h} \tag{B-25}$$

for the second derivative we will make use of the Taylor expansion

$$f''(a) = \frac{f(a-h) - 2f(a) + f(a+h)}{h^2} \tag{B-26}$$

Using this concept, the discretized version of *equation (B-22)* is

$$\Phi_{1,i}\left(\frac{K_{i,j}-K_{i-1,j}}{\Delta x}\right)+\Phi_{1,j}\left(\frac{K_{i,j}-K_{i,j-1}}{\Delta y}\right)+K_{i,j}\nabla.\Phi_1 -$$

$$\Phi_{0,i}\left(\frac{K_{i,j}-K_{i-1,j}}{\Delta x}\right)+\Phi_{0,j}\left(\frac{K_{i,j}-K_{i,j-1}}{\Delta y}\right)+K_{i,j}\nabla.\Phi_0 = Q_\Delta$$

(B-27)

the aim here is to manipulate equation (2-30) in order to isolate $K_{i,j}$, hence

$$K_{i,j}\left(\nabla.\Phi_1+\frac{\Phi_{1,i}}{\Delta x}+\frac{\Phi_{1,j}}{\Delta y}\right)-\frac{\Phi_{1,i}}{\Delta x}K_{i-1,j}-\frac{\Phi_{1,j}}{\Delta y}K_{i,j-1}-$$

$$K_{i,j}\left(\nabla.\Phi_0+\frac{\Phi_{0,i}}{\Delta x}+\frac{\Phi_{0,j}}{\Delta y}\right)-\frac{\Phi_{0,i}}{\Delta x}K_{i-1,j}-\frac{\Phi_{0,j}}{\Delta y}K_{i,j-1}=Q_\Delta$$

(B-28)

$$K_{i,j}\left[\left(\nabla.\Phi_1+\frac{\Phi_{1,i}}{\Delta x}+\frac{\Phi_{1,j}}{\Delta y}\right)-\left(\nabla.\Phi_0+\frac{\Phi_{0,i}}{\Delta x}+\frac{\Phi_{0,j}}{\Delta y}\right)\right]=$$

$$Q_\Delta+\frac{\Phi_{1,i}}{\Delta x}K_{i-1,j}+\frac{\Phi_{1,j}}{\Delta y}K_{i,j-1}+\frac{\Phi_{0,i}}{\Delta x}K_{i-1,j}+\frac{\Phi_{0,j}}{\Delta y}K_{i,j-1}$$

(B-29)

$$K_{i,j}=\left[Q_\Delta+\frac{\Phi_{1,i}}{\Delta x}K_{i-1,j}+\frac{\Phi_{1,j}}{\Delta y}K_{i,j-1}+\frac{\Phi_{0,i}}{\Delta x}K_{i-1,j}+\frac{\Phi_{0,j}}{\Delta y}K_{i,j-1}\right].$$

$$\left[\left(\nabla.\Phi_1+\frac{\Phi_{1,i}}{\Delta x}+\frac{\Phi_{1,j}}{\Delta y}\right)-\left(\nabla.\Phi_0+\frac{\Phi_{0,i}}{\Delta x}+\frac{\Phi_{0,j}}{\Delta y}\right)\right]^{-1}$$

(B-30)

B.3 Permeability estimation using synthetic data

An alternative additional formulation was derived following the rationale of section B2, with the intent of presenting an innovative tool for permeability estimation. The formulation here proposed intends to use saturation data in terms of phase mobility data and water breakthrough, which will then be used to aid the estimation of the absolute permeability of the reservoir.

 Starting from Peaceman's single phase fluid flow equations (section B1) for oil and water only assuming incompressible flow (D, ρ_o, ρ_w, are constant), also for simplicity ϕ is considered constant with pressure while α is considered constant with position, then *equations (B-1 & B-2)* can be re-written as:

$$\nabla\cdot\left[\frac{Kk_{ro}}{\mu_o}\nabla P_o\right]+Q_o=\phi\frac{\partial S_o}{\partial t}$$

(B-31)

106

$$\nabla \cdot \left[\frac{Kk_{rw}}{\mu_w} \nabla P_w \right] + Q_w = \phi \frac{\partial S_w}{\partial t} \tag{B-32}$$

where $Q_o = \dfrac{q_o}{\rho_o}$ and $Q_w = \dfrac{q_w}{\rho_w}$ are the volumetric rates of injection per reservoir volume.

Considering the concepts of oil, water and total mobility respectively we obtain:

$$\lambda_o = \frac{Kk_{ro}}{\mu_o} \tag{B-33}$$

$$\lambda_w = \frac{Kk_{rw}}{\mu_w} \tag{B-34}$$

$$\lambda_t = \lambda_o + \lambda_w \tag{B-35}$$

Equations (B-31) & *(B-32)* can then be written as:

$$\nabla \cdot \left(\lambda_o \nabla P_o \right) + Q_o = \phi \frac{\partial S_o}{\partial t} \tag{B-36}$$

$$\nabla \cdot \left(\lambda_w \nabla P_w \right) + Q_w = \phi \frac{\partial S_w}{\partial t} \tag{B-37}$$

The concepts of average and capillary pressures are respectively introduced as:

$$p_{avg} = \left(p_o + p_w \right) \Big/ 2 \tag{B-38}$$

$$p_c = p_o - p_w \tag{B-39}$$

and the concepts of individual phase velocities (oil, water) together with the concept of total velocity are respectively introduced, being the phase nobilities from *equation (B-33 to B-35)* considering horizontal flow:

$$\vec{v}_o = -\lambda_o \nabla P_o \tag{B-40}$$

$$\vec{v}_w = -\lambda_w \nabla P_w \tag{B-41}$$

$$\vec{v}_t = \vec{v}_o + \vec{v}_w \tag{B-42}$$

For the definition of the *differential saturation equation* for non-horizontal flow the equations above take the form:

$$\nabla p_c = \nabla p_o - \nabla p_w \tag{B-43}$$

$$\vec{v}_o = -\lambda_o \left(\nabla P_o - \rho_o g \nabla D \right) \tag{B-44}$$

$$\vec{\upsilon}_w = -\lambda_w \left(\nabla P_w - \rho_w g \nabla D \right) \tag{B-45}$$

The 3 equations above after combined and rearranged yield:

$$\lambda_o \lambda_w \nabla P_c = \lambda_w \vec{\upsilon}_o + \lambda_o \vec{\upsilon}_w + \lambda_o \lambda_w \left(\rho_o - \rho_w \right) g \nabla D \tag{B-45a}$$

Where $\vec{\upsilon}_o$ can be eliminated using *equation (B-42)*, producing:

$$\left(\lambda_o + \lambda_w \right) \vec{\upsilon}_w = \lambda_w \vec{\upsilon}_t + \lambda_o \lambda_w \left[\nabla P_c + \left(\rho_w - \rho_o \right) g \nabla D \right]$$
(B-46)

Using Figure 50-C1 that can be found in the *appendix D,* Buckley-Leverett theory illustrates a typical curve of f_w vs. $S_{w.}$ (Peaceman, 1977), used the Figure 50-C1 to derive the expressions f_w and h_w in *equations* bellow these expressions are functions of saturation, defined as:

$$f_w = \frac{\lambda_w}{\lambda_o + \lambda_w} \tag{B-47}$$

$$\left(\lambda_o + \lambda_w \right) = \lambda_w / f_w \tag{B-47a}$$

$$h_w = -\frac{\lambda_o \lambda_w}{\lambda_o + \lambda_w} \frac{dp_c}{dS_w} \tag{B-48}$$

$$-\left(h_w \frac{dS_w}{dp_c} \right) \left(\lambda_o + \lambda_w \right) = \lambda_o \lambda_w \tag{B-48a}$$

$$\lambda_w = -\frac{\lambda_o}{\left(h_w \dfrac{dS_w}{dp_c} \right) \left(\lambda_o + \lambda_w \right)} \tag{B-48b}$$

f_w can be defined as fractional flow of water while h_w is function of saturation involving mobility and capillarity.

Introducing *equations (B-47a)* & *(B-48a)* into the *equation (B-46)* we obtain:

$$\frac{\lambda_w}{f_w} \vec{\upsilon}_w = \lambda_w \vec{\upsilon}_t + \left[-\left(h_w \frac{dS_w}{dp_c} \right) \left(\lambda_o + \lambda_w \right) \right] \left[\nabla P_c + \left(\rho_w - \rho_o \right) g \nabla D \right] \tag{B-48c}$$

Simplifying, the equation above:

$$\vec{\upsilon}_w = f_w \vec{\upsilon}_t + \left\{ -\left[\left(h_w \frac{dS_w}{dp_c} \right) \left(\lambda_o + \lambda_w \right) \right] \left[\nabla P_c + \left(\rho_w - \rho_o \right) g \nabla D \right] \right\} \frac{f_w}{\lambda_w} \tag{B-48d}$$

$$\vec{\upsilon}_w = f_w \vec{\upsilon}_t + \left\{ -\left[\left(h_w \frac{dS_w}{dp_c} \right) \left(\lambda_o + \lambda_w \right) \right] \nabla P_c - \left[\left(h_w \frac{dS_w}{dp_c} \right) \left(\lambda_o + \lambda_w \right) \right] \left(\rho_w - \rho_o \right) g \nabla D \right\} \frac{f_w}{\lambda_w}$$

(B-48e)

$$\vec{\upsilon}_w = f_w \vec{\upsilon}_t - \left[\left(h_w \frac{dS_w}{dp_c} \right) \nabla P_c \left(\frac{\lambda_o + \lambda_w}{\lambda_w} \right) f_w \right] - \left[\left(h_w \frac{dS_w}{dp_c} \right) (\lambda_o + \lambda_w) \frac{f_w}{\lambda_w} (\rho_w - \rho_o) g \nabla D \right]$$

(B-48f)

From *equation (B-47)* $\dfrac{1}{f_w} = \dfrac{\lambda_o + \lambda_w}{\lambda_w}$ then equation (B-48) becomes:

$$\vec{\upsilon}_w = f_w \vec{\upsilon}_t - \left[\left(h_w \frac{dS_w}{dp_c} \right) \nabla P_c \right] - \left[\left(h_w \frac{dS_w}{dp_c} \right) (\lambda_o + \lambda_w) \frac{f_w}{\lambda_w} (\rho_w - \rho_o) g \nabla D \right] \qquad \text{(B-48g)}$$

Using *equation (B-48b)* to eliminate λ_w from the previous equation we obtain:

$$\vec{\upsilon}_w = f_w \vec{\upsilon}_t - \left\{ \left[\left(h_w \frac{dS_w}{dp_c} \right) \nabla P_c \right] + \left[\frac{\left(h_w \frac{dS_w}{dp_c} \right) (\lambda_o + \lambda_w) \lambda_o}{\left(h_w \frac{dS_w}{dp_c} \right) (\lambda_o + \lambda_w)} f_w (\rho_w - \rho_o) g \nabla D \right] \right\} \qquad \text{(B-48h)}$$

Simplifying (B-48h) we obtain:

$$\vec{\upsilon}_w = f_w \vec{\upsilon}_t - h_w \nabla S_w + \lambda_o f_w (\rho_w - \rho_o) g \nabla D \qquad \text{(B-49)}$$

According to (Peaceman, 1977) the continuity equations for single-phase flow can be defined as:

$$-\nabla \cdot \left(\alpha \rho_o \vec{\upsilon}_o \right) + \alpha q_o = \alpha \frac{\partial (\phi \rho_o S_o)}{\partial t} \qquad \text{(B-50)}$$

$$-\nabla \cdot \left(\alpha \rho_w \vec{\upsilon}_w \right) + \alpha q_w = \alpha \frac{\partial (\phi \rho_w S_w)}{\partial t} \qquad \text{(B-51)}$$

by introducing *equation (B-49)* into the continuity equation for single flow of water (B-51) for the saturation may be written as:

$$\nabla \cdot \alpha \rho_w \left[f_w \vec{\upsilon}_t - h_w \nabla S_w + \lambda_o f_w (\rho_w - \rho_o) g \nabla D \right] + \alpha q_w = \alpha \frac{\partial (\phi \rho_w S_w)}{\partial t} \qquad \text{(B-52)}$$

simplifying:

$$\nabla . \left(\alpha \rho_w h_w \nabla S_w \right) - \nabla . \left(\alpha \rho_w f_w \right) \left[\vec{\upsilon}_t + \lambda_o (\rho_w - \rho_o) g \nabla D \right] + \alpha q_w = \alpha \frac{\partial (\phi \rho_w S_w)}{\partial t} \qquad \text{(B-53)}$$

assuming that $D, \rho_o, \rho_w, \alpha$ and ϕ do not change, *equation (B-53)* becomes:

$$\nabla . \left(h_w \nabla S_w \right) - \nabla . \left(f_w \right) \left[\vec{\upsilon}_t + \lambda_o \right] + Q_w = \phi \frac{\partial S_w}{\partial t} \qquad \text{(B-54)}$$

$$\nabla.\left(h_w \nabla S_w\right) - \nabla.\left(f_w \vec{\upsilon}_t\right) - \nabla.\left(f_w \lambda_o\right) + Q_w = \phi \frac{\partial S_w}{\partial t} \qquad \text{(B-55)}$$

Expression $\nabla.\left(f_w \vec{\upsilon}_t\right)$ from *equation (B-55)* can be expanded using the chain rule, hence:

$$\nabla.\left(f_w \vec{\upsilon}_t\right) = f_w \nabla.\vec{\upsilon}_t + \vec{\upsilon}_t.\nabla f_w \qquad \text{(B-55a)}$$

to solve the expression $\vec{\upsilon}_t.\nabla f_w$ on *equation (B-55)* we use the solution for the product of two vectors as:

$$\vec{\upsilon}\cdot\vec{u} = u_x \upsilon_x + u_y \upsilon_y + u_z \upsilon_z \qquad \text{(B-56)}$$

so that

$$\nabla.f_w = \frac{df_w}{dS_w}\nabla S_w \qquad \text{(B-57)}$$

and considering *equations (B-55a)* to *(B-57)*, *equation (B-55)* can be re-written as:

$$\nabla.\left(h_w \nabla S_w\right) - \nabla.\vec{\upsilon}_t - \frac{df_w}{dS_w}\vec{\upsilon}_t.\nabla S_w - \nabla.\left(f_w \lambda_o\right) + Q_w = \phi \frac{\partial S_w}{\partial t} \qquad \text{(B-58)}$$

because it is assumed that the fluid is incompressible, then

$$\nabla.\vec{\upsilon}_t = 0 \qquad \text{(B-59)}$$

and *equation (B-58)* becomes:

$$\nabla.\left(h_w \nabla S_w\right) - \frac{df_w}{dS_w}\vec{\upsilon}_t.\nabla S_w - \nabla.\left(f_w \lambda_o\right) + Q_w = \phi \frac{\partial S_w}{\partial t} \qquad \text{(B-60)}$$

by considering *equation (B-48)* to eliminate h_w, *equation (B-60)* becomes:

$$\nabla.\left(-\frac{\lambda_o \lambda_w}{\lambda_o + \lambda_w}\frac{dp_c}{dS_w}\nabla S_w\right) - \frac{df_w}{dS_w}\vec{\upsilon}_t.\nabla S_w - \nabla.\left(f_w \lambda_o\right) + Q_w = \phi \frac{\partial S_w}{\partial t} \qquad \text{(B-61)}$$

using *equation (B-47)* it can be obtained that:

$$-\nabla.\left(\lambda_o f_w \frac{dp_c}{dS_w}\nabla S_w\right) - \frac{df_w}{dS_w}\vec{\upsilon}_t.\nabla S_w - \nabla.\left(f_w \lambda_o\right) + Q_w = \phi \frac{\partial S_w}{\partial t} \qquad \text{(B-62)}$$

If for simplicity it is assumed that υ_{t_x} is constant based on fact that the flow is incompressible, and the multidimensional equation in (Buckley & Leverett, 1942)

$$\left(\frac{dx}{dt_w}\right)_{S_w} = \frac{\upsilon_{t_x}}{\phi}\frac{df_w}{dS_w}$$

(B-63)

It can be obtained that:

$$-\nabla\cdot\left(f_w\lambda_o\nabla P_c\right)-\nabla\cdot\left(f_w\vec{\upsilon}_t\right)+Q_w = \phi\frac{\partial S_w}{\partial t}$$

(B-64)

Equation (B-64) is to be used by the project with the primary aim of estimating permeability from an equation that incorporates fractional flow, capillary data, total velocity data and saturation data.

In order to estimate permeability however, some assumptions have to made to allow mathematical simplifications and isolation of the target variable, we shall start by assuming that capillary pressure in (B-64) can be neglected, turning the equation into:

$$-\nabla\cdot\left(f_w\vec{\upsilon}_t\right)+Q_w = \phi\frac{\partial S_w}{\partial t}$$

(B-65)

In equation (B-64), the rate of change of the water flux with position accounts for the fraction of water in a reservoir, coupled with total fluid flux data, fractional flow data can be useful for estimation of position of the fluid front, time of water breakthrough water-cut at breakthrough or even recovery after breakthrough. In order to characterize the interaction of two fluids (oil and water), such as in the case of a black oil reservoir, a new equation has to emerge containing the oil, this is done by simply adding the oil-phase in *equation (B-50)* to the *equation (B-64)*, yielding:

$$-\nabla\cdot\left[\left(f_w\vec{\upsilon}_t\right)+\left(\vec{\upsilon}_o\right)\right]+\left(Q_w+Q_o\right) = \phi\frac{\partial}{\partial t}\left(S_w+S_o\right)$$

(B-66)

considering that $Q_o = \dfrac{q_o}{\rho_o}$

If total rate, Q is $Q = Q_w + Q_o$, then

$$-\nabla\cdot\left(f_w\vec{\upsilon}_t+\vec{\upsilon}_o\right)+Q = 0$$

(B-66a)

using *equations (B-40) to (B-42) into (B-66a)* to replace $\vec{\upsilon}_o$, $\vec{\upsilon}_w$ and $\vec{\upsilon}_t$ we obtain:

$$\nabla\cdot\left[f_w\left(-\lambda_o\nabla P_o-\lambda_w\nabla P_w\right)-\lambda_o\nabla P_o\right] = Q$$
(B-67)

if capillary pressure is neglected then, $P_o = P_w = P$, by replacing λ_o and λ_w according to *equations (B-33) & (B-34)* respectively, we obtain:

$$\nabla \cdot \left[f_w \left(-\frac{K k_{ro}}{\mu_o} \nabla P - \frac{K k_{rw}}{\mu_w} \nabla P \right) - \frac{K k_{ro}}{\mu_o} \nabla P \right] = Q \tag{B-68}$$

simplifying

$$\nabla \cdot \left[K f_w \nabla P \left(-\frac{k_{ro}}{\mu_o} - \frac{k_{rw}}{\mu_w} \right) - \frac{K k_{ro}}{\mu_o} \nabla P \right] = Q \tag{B-69}$$

If $M_o = \dfrac{k_{ro}}{\mu_o}$, $M_w = \dfrac{k_{rw}}{\mu_w}$ and $M_t = \dfrac{k_{ro}}{\mu_o} + \dfrac{k_{rw}}{\mu_w}$ then *equation (B-68)* becomes

$$\nabla \cdot \left[K f_w \nabla P \left(-M_t - \frac{M_o}{f_w} \right) \right] = Q \tag{B-69a}$$

For simplicity $f_w=f$, and $\psi = \left(-M_t - \dfrac{M_o}{f_w} \right)$ then

$$\nabla \cdot \left[K f \psi \nabla P \right] = Q \tag{B-70}$$

In presence of saturation plots such as those in Figure 27, mobility and relative permeability data can be read as a function of saturation. Using *equation (B-69a)*, a relationship between permeability can be established provided that saturation related data is available and the assumptions used to derive it apply.
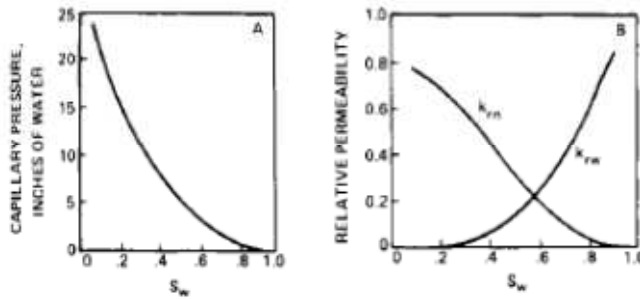
Figure 46-B3: Typical curves for two-phase data. A. Capilary pressure. B. Relative permeabilities. After (Peaceman,1977)

In order to extract the reservoir permeability using time-lapse changes, the variable parameters in (B-70) are considered in two distinct times, T_0 and T_1 subject to two boundary conditions Q_0 and Q_1, respectively, the governing equations become:

$$\nabla \cdot \left[K f_0 \psi_0 \nabla P_0 \right] = Q_0 \tag{B-71}$$

where $\psi_0 = \left(-M_t - \dfrac{M_o}{f_0} \right)$

$$\nabla \cdot \left[Kf_1 \psi_0 \nabla P_1 \right] = Q_1 \qquad \text{(B-72)}$$

where $\psi_1 = \left(-M_t - \dfrac{M_o}{f_1} \right)$

Subtracting *equation (B-72)* from *equation (B-71)*

then

$$\nabla \cdot \left[Kf_1 \psi_1 \nabla P_1 - Kf_0 \psi_0 \nabla P_0 \right] = Q_1 - Q_0 \qquad \text{(B-73)}$$

if

$$Q_\Delta = Q_1 - Q_0 \qquad \text{(B-74)}$$

$$\nabla \cdot \left[Kf_1 \psi_1 \nabla P_1 - Kf_0 \psi_0 \nabla P_0 \right] = Q_\Delta \qquad \text{(B-75)}$$

if we define

$$\Phi_0 = f_0 . \psi_0 . \nabla P_0 \qquad \text{(B-76)}$$

$$\Phi_1 = f_1 . \psi_1 . \nabla P_1 \qquad \text{(B-77)}$$

$$P_\Delta = P_1 - P_0 \qquad \text{(B-78)}$$

then

$$P_1 = P_\Delta + P_0 \qquad \text{(B-79)}$$

To establish a link with 4D seismic a function must be created to link pressure-saturation changes to changes in the mapped seismic attribute, a function of the kind $\Delta A = f(\Delta P, \Delta S)$ from which P_Δ will be estimated.

Using *equation (B-79)* the *equation (B-75)* can be re-written as

$$\nabla \cdot \left[K . \Phi_1 - K . \Phi_0 \right] = Q_\Delta \qquad \text{(B-80)}$$

using the approximation of the product rule for the ∇ operator, the equation above can be re-written as

$$\nabla K \cdot \Phi_1 + K \nabla . \Phi_1 - \nabla K \cdot \Phi_0 + K \nabla . \Phi_0 = Q_\Delta \qquad \text{(B-81)}$$

for the finite approximations of the partial we will make use of the Newton's difference quotient in the form:

$$m = \frac{\Delta f(x)}{\Delta x} = \frac{f(x+h) - f(x)}{h} \qquad \text{(B-82)}$$

where *h* is a small value that represents an approximation to the slope so that the derivative *f* at *a* is a function of the limit

$$f`(a)\lim_{h \to 0} = \frac{f(a+h) - f(a)}{h}$$

(B-83)

$f'(a)$ represents one of the notations of the derivative to produce a linear approximation of the kind

$$f'(a) = \frac{f(a+h) - f(a)}{h}$$

(B-84)

for the second derivative we will make use of the Taylor expansion

$$f''(a) = \frac{f(a-h) - 2f(a) + f(a+h)}{h^2}$$

(B-85)

Using this concept, the discretized version of *equation (B-81)* is

$$\Phi_{1,i}\left(\frac{K_{i,j} - K_{i-1,j}}{\Delta x}\right) + \Phi_{1,j}\left(\frac{K_{i,j} - K_{i,j-1}}{\Delta y}\right) + K_{i,j}\nabla.\Phi_1 -$$

$$\Phi_{0,i}\left(\frac{K_{i,j} - K_{i-1,j}}{\Delta x}\right) + \Phi_{0,j}\left(\frac{K_{i,j} - K_{i,j-1}}{\Delta y}\right) + K_{i,j}\nabla.\Phi_0 = Q_\Delta$$

(B-86)

the aim here is to manipulate equation above in order to isolate $K_{i,j}$, hence

$$K_{i,j}\left(\nabla.\Phi_1 + \frac{\Phi_{1,i}}{\Delta x} + \frac{\Phi_{1,j}}{\Delta y}\right) - \frac{\Phi_{1,i}}{\Delta x}K_{i-1,j} - \frac{\Phi_{1,j}}{\Delta y}K_{i,j-1} -$$

$$K_{i,j}\left(\nabla.\Phi_0 + \frac{\Phi_{0,i}}{\Delta x} + \frac{\Phi_{0,j}}{\Delta y}\right) - \frac{\Phi_{0,i}}{\Delta x}K_{i-1,j} - \frac{\Phi_{0,j}}{\Delta y}K_{i,j-1} = Q_\Delta$$

(B-87)

$$K_{i,j} = \left[Q_\Delta + \frac{\Phi_{1,i}}{\Delta x}K_{i-1,j} + \frac{\Phi_{1,j}}{\Delta y}K_{i,j-1} + \frac{\Phi_{0,i}}{\Delta x}K_{i-1,j} + \frac{\Phi_{0,j}}{\Delta y}K_{i,j-1}\right].$$

$$\left[\left(\nabla.\Phi_1 + \frac{\Phi_{1,i}}{\Delta x} + \frac{\Phi_{1,j}}{\Delta y}\right) - \left(\nabla.\Phi_0 + \frac{\Phi_{0,i}}{\Delta x} + \frac{\Phi_{0,j}}{\Delta y}\right)\right]^{-1}$$
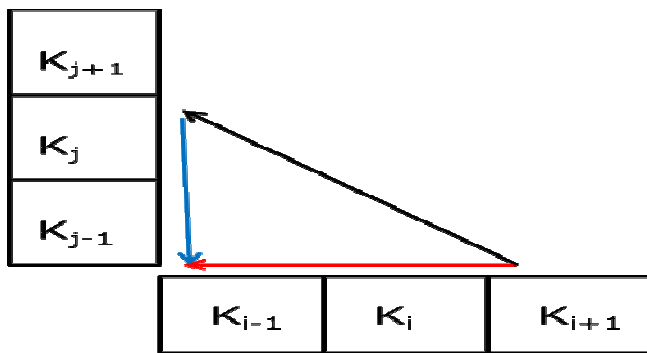
(B-88)

Figure 47-B3: Derivation of the gradient method applied

Equation (B-88) represents the expression proposed by the project to estimate the permeability for the two-phase flow; at initial saturation conditions, the estimated ($K_{i,j}$) depends on changes in the total flow rate (Q_Δ), spatial variability of the initial permeability estimates (K_{i-1} and K_{i-1}) and spatial variability of parameter Φ, defined in equations (B-76 and B-77). $\psi = \left(-M_t - \dfrac{M_o}{f_w} \right)$

C. Matrix norms

The analysis of matrix data in the models brought the need of using matrix norms, these could be using to measure the distance on the space of matrices that quantify the notion of near-singularity from a linear system of poor or nearly singular matrix coefficients.

C.1 Definitions

In presence of isomorphism between R^{mxn} and R^{mn}, *f:* $R^{mxn} \to R$ is a matrix that satisfies the following properties:

$f(A) \geq 0$ $\qquad\qquad A \in R^{mxn}$, $\qquad\qquad (f(A) = 0 \; if \; A = 0)$
$f(A + B) \leq f(A) + f(B)$ $\qquad\qquad A, B \in R^{mxn}$,
$f(\alpha A) = |\alpha| f(A)$ $\qquad\qquad \alpha \in R, A \in R^{mxn}$,

A double bar notation with subscripts are used to designate matrix norms, e.g.: $\|A\| = f(A)$

The norms used by the project include:

The Frobenius norm:

$$\|A\|_F = \sqrt{\sum_{i=1}^{m} \sum_{j=1}^{n} |a_{ij}|^2} \tag{C-1}$$

The p-norms:

$$\|A\|_P = \frac{sup}{x \neq 0} \frac{\|Ax\|_P}{\|x\|_P} \tag{C-2}$$

D. Buckley-Leverett analysis

Buckley-Leverett represents the basic equation for describing immiscible displacement in one dimension. For water displacing oil, the equation determines

the velocity of a plane of constant water saturation travelling through a linear system (Dake, 1978).

The assumptions of the Buckley-Leverett are:

- The flow is linear and horizontal
- Water is injected into an oil reservoir
- Oil and water are both incompressible and immiscible
- and capillary pressure effects are neglected.

The typical saturation profiles produced by Buckley-Leverett theory are:
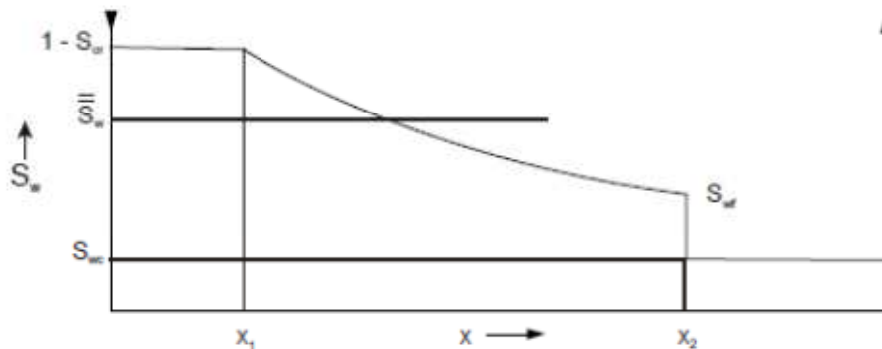
Figure 48-D: Water saturation distribution as a function of distance, prior to breakthrough in the producing well, after (Dake, 1978)

D.1   Derivation of the fractional flow

Figure 49-C1: Schematic representation of an oil-water system used for the derivation of fractional flow equation, adapted from (Harting, et al., 2005)

For a one-dimensional linear reservoir where oil co-exists with water (represented by the figure above), we start by using the Darcy's equation

$$q_o = -\frac{kk_{ro}A}{\mu_o}\frac{\partial P_o}{\partial x} \qquad \text{for oil} \tag{D-1}$$

$$q_w = -\frac{kk_{rw}A}{\mu_w}\frac{\partial P_w}{\partial x} \qquad \text{for water} \tag{D-2}$$
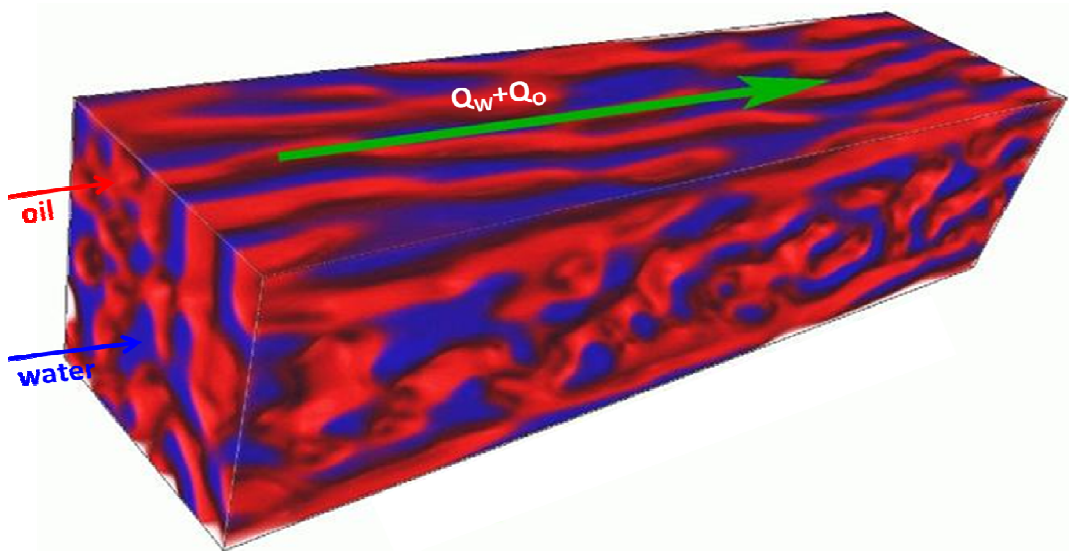
Given that $p_c = p_o - p_w$ the water pressure in (D-2) can be replaced by $p_w = p_o - p_c$ so that

$$q_w = -\frac{kk_{rw}A}{\mu_w}\left(\frac{\partial(P_o - P_c)}{\partial x}\right) \tag{D-3}$$

rearranging

$$-q_w\frac{\mu_w}{kk_{rw}A} = \frac{\partial P_o}{\partial x} - \frac{\partial P_c}{\partial x} \tag{D-4}$$

rearranging (D-1) we obtain

$$-q_o\frac{\mu_o}{kk_{ro}A} = \frac{\partial P_o}{\partial x} \tag{D-5}$$

subtracting (D-4) from (D-5)

$$-\frac{1}{kA}\left(q_w\frac{\mu_w}{k_{rw}} - q_o\frac{\mu_o}{k_{ro}}\right) = -\frac{\partial P_c}{\partial x} \tag{D-6}$$

Given that $q = q_o + q_w$ and $f = \dfrac{1}{q_o + q_w}$ it can be obtained that

$$f_w = \frac{1 + \dfrac{kk_{ro}A}{\mu_o}\dfrac{\partial P_c}{\partial x}}{1 + \dfrac{k_{ro}}{\mu_o}\dfrac{\mu_w}{k_{rw}}} \tag{D-7}$$

or simply

$$f_w = \frac{1}{1 + \dfrac{k_{ro}}{\mu_o}\dfrac{\mu_w}{k_{rw}}} \tag{8}$$

Where:

$$f_w = \frac{1}{1 + \dfrac{\mu_w}{k_{rw}}\cdot\dfrac{k_{ro}}{\mu_o}} \tag{D-9}$$ Fractional flow equation

$$t_{bt} = \frac{L}{V_f} = \frac{L\phi}{u_t}\frac{S_{wf} - S_{wi}}{f_w\big|_{swf}} \tag{D-10}$$ Time for breakthrough

$$\overline{S_w} - S_{wi} = \frac{1}{\left(\dfrac{df_w}{dS_w}\right)_{swf}}$$

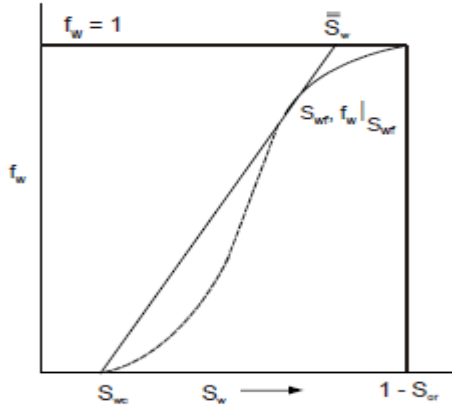The figure bellow represents a typical plot of the corresponding fractional flow curves

Figure 50-C1: Tangent to the fractional flow curve from Sw=Swc, after (Dake, 1978)

D.2 Derivation of the Buckley-Leverett equation

For the derivation of the Buckley-Leverett equation, we start by considering a situation in which water displaces oil in a control box of volume AΔx during a time period Δt
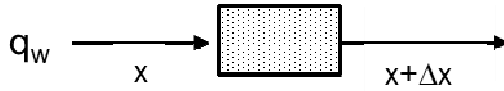
Figure 51-D2: Representation of fluid displacement over a controlled volume AΔx

The mass balance of becomes:

$$\left[\left(q_w \rho_w\right)_x - \left(q_w \rho_w\right)_{x+\Delta x}\right]\Delta t = A\Delta x\left[\left(S_w \rho_w\right)^{t+\Delta t} - \left(S_w \rho_w\right)^t\right]$$

(D-11)

When $\lim_{\Delta x \to 0}$ and $\lim_{\Delta t \to 0}$

$$\frac{\partial}{\partial x}\left(q_w \rho_w\right) = \frac{\partial}{\partial t}\left(S_w \rho_w\right)$$

(D-12)

The equation above is known as the continuity equation.

Assuming that the fluid compressibility can be neglected, i.e.: $\rho_w = const.$

And given that $\rho_w = f_w q$

$$\frac{\partial}{\partial x} f_w = \frac{A\phi}{q} \frac{\partial S_w}{\partial t}$$

(D-13)

Since $f_w(S_w)$ then equation (D-13) can be written as

$$\frac{df_w}{dS_w} \frac{\partial S_w}{\partial x} = \frac{A\phi}{q} \frac{\partial S_w}{\partial t}$$

(D-14)

E. Production data and plots

E.1 MDT data used for generation of pressure-depth relations

Table 10: Pressure and depth information obtained using MDT tool. The wells penetrated are: Exploration well (W0), Production wells (OP1, OP4 and OP5) and Injector well (WI2)

WELL	depth		Formation Pressure
	m/RT	m/msl	psi abs
W0	2272.10	2205.56	3344.50
W0	2274.50	2207.61	3345.54
W0	2321.30	2247.47	3393.25
W0	2325.00	2250.62	3396.73
W0	2329.00	2254.02	3400.96
W0	2384.90	2301.66	3455.16
W0	2399.00	2313.68	3469.63
W0	2398.00	2312.82	3468.53
W0	2424.80	2335.64	3494.25
W0	2426.60	2337.17	3496.15
W0	2428.60	2338.88	3498.33
W0	2429.40	2339.56	3498.99
W0	2443.00	2351.07	3513.26
W0	2445.50	2353.19	3515.40
W0	2581.00	2461.00	3677.28
W0	2584.00	2463.34	3681.14
W0	2587.20	2465.83	3685.12
W0	2682.20	2540.66	3801.29
W0	2684.60	2542.56	3804.38
W0	2687.60	2544.95	3808.39
W0	2682.20	2540.66	3801.46
W0	2687.60	2544.95	3808.25
W0	2587.20	2465.83	3682.14
W0	2429.40	2339.56	3498.90
W0	2329.00	2254.02	3400.16
W0	2326.60	2251.98	3397.56
W0	2384.90	2301.66	3455.00

WELL	depth		Formation Pressure
	m/RT	m/msl	psi abs
OP1	3490	2092.749023	3214.19
OP1	3897	2192.003906	3331.09
OP1	4153	2292.523926	3448.98
OP1	4209.8	2318.068115	3477.5
OP1	4157.05	2294.233154	3449.6
OP1	4153	2292.523926	3447.75
OP1	4112.56	2275.477539	3427.42

WELL	depth		Formation Pressure
	m/RT	m/msl	psi abs
WI2	2206.00	2139.31	3125.00
WI2	2191.60	2130.06	3115.00
WI2	2189.09	2128.42	3113.00
WI2	2211.01	2142.48	3129.00
WI2	2264.48	2175.69	3220.00
WI2	2263.57	2175.13	3219.00
WI2	2313.59	2205.87	3299.00
WI2	2313.10	2205.56	3298.00
WI2	2346.83	2227.08	3295.00
WI2	2344.32	2225.43	3256.00
WI2	2373.57	2244.62	3312.00
WI2	2372.55	2243.94	3311.00
WI2	2397.02	2260.09	3319.00
WI2	2395.07	2258.80	3318.00
WI2	2539.52	2353.73	3475.00
WI2	2533.61	2349.75	3472.00
WI2	2346.47	2226.84	3296.00

WELL	depth m/RT	depth m/msl	Formation Pressure psi abs
OP4	2522.26	2145.79	3223.41
OP4	2544.86	2148.27	3225.34
OP4	2577.62	2151.44	3225.31
OP4	2731.46	2165.07	3217.31
OP4	2916.14	2178.37	3232.15
OP4	3076.97	2187.03	3235.14
OP4	3130.95	2189.39	3237.14
OP4	3667.43	2207.50	3244.03
OP4	3736.92	2208.23	3245.01
OP4	3854.70	2207.79	3243.99

WELL	depth m/RT	depth m/msl	Formation Pressure psi abs
OP5	3165.04	2229.21	3297.91
OP5	3211.77	2240.67	3315.91
OP5	3460.87	2301.33	3363.68
OP5	3579.87	2315.73	3381.29
OP5	3669.77	2318.07	3386.03
OP5	3757.87	2317.90	3387.04

E.2 Thickness, well, model and parameter information

Table 11: Thickness information of the reservoir layers at the different wells

Res. Layer	Reservoir Thickness (m) W0	OP1	OP2	OP3	OP4	OP5	Min	Max	Avg
R1	6.24	62.00	52.84	51.35	49.72	19.00	6.24	62.00	40.19
R2	10.56	25.02	21.10	56.33	19.66	9.00	9.00	56.33	23.61
R3	11.96			387.58	19.66		11.96	387.58	139.73
R4	7.71		42.75				7.71	42.75	25.23
R5		84.00			157.11		84.00	157.11	120.56
R8a	8.91		35.40				8.91	35.40	22.16
R8b	7.10		23.63				7.10	23.63	15.36
R9		15.19					15.19	15.19	15.19
R10a	10.98	20.00	108.62				10.98	108.62	46.53
R10b	8.33	5.52					5.52	8.33	6.92
R12a		35.50					35.50	35.50	35.50
R12b		53.90					53.90	53.90	53.90
R14	67.20						67.20	67.20	67.20
Total	138.99	301.13	284.34	495.26	246.15	28.00			

Table 12: Workflow for estimation of density information - from slope of the pressure-depth plots to density estimation.
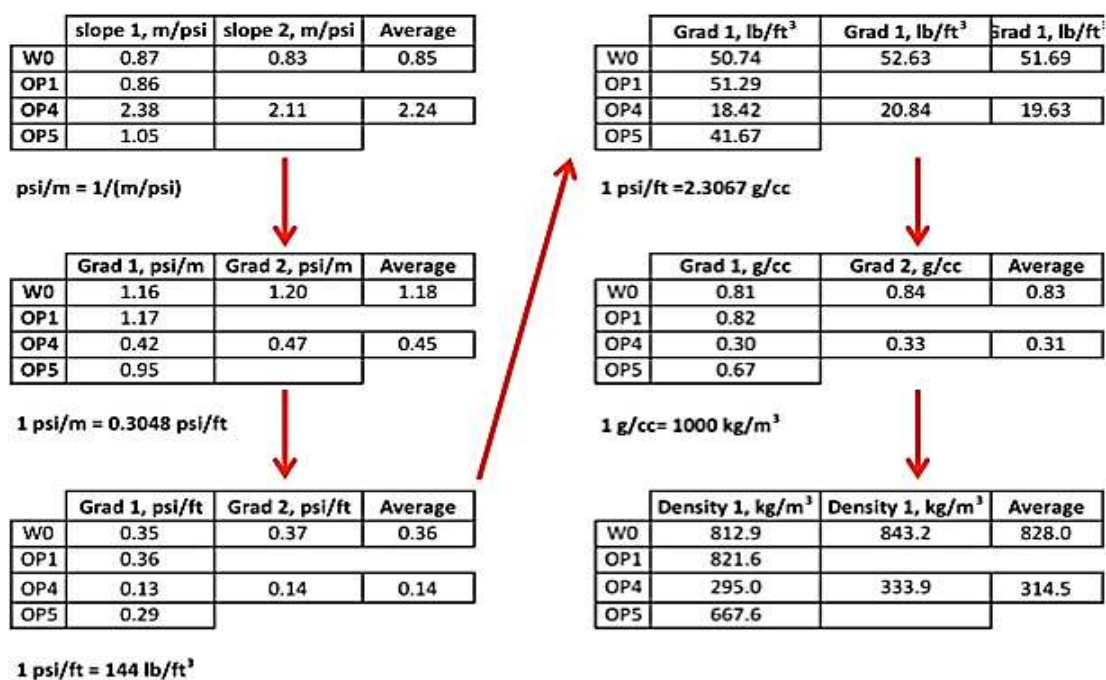
	slope 1, m/psi	slope 2, m/psi	Average
W0	0.87	0.83	0.85
OP1	0.86		
OP4	2.38	2.11	2.24
OP5	1.05		

psi/m = 1/(m/psi)

	Grad 1, psi/m	Grad 2, psi/m	Average
W0	1.16	1.20	1.18
OP1	1.17		
OP4	0.42	0.47	0.45
OP5	0.95		

1 psi/m = 0.3048 psi/ft

	Grad 1, psi/ft	Grad 2, psi/ft	Average
W0	0.35	0.37	0.36
OP1	0.36		
OP4	0.13	0.14	0.14
OP5	0.29		

1 psi/ft = 144 lb/ft³

	Grad 1, lb/ft³	Grad 1, lb/ft³	Grad 1, lb/ft³
W0	50.74	52.63	51.69
OP1	51.29		
OP4	18.42	20.84	19.63
OP5	41.67		

1 psi/ft =2.3067 g/cc

	Grad 1, g/cc	Grad 2, g/cc	Average
W0	0.81	0.84	0.83
OP1	0.82		
OP4	0.30	0.33	0.31
OP5	0.67		

1 g/cc= 1000 kg/m³

	Density 1, kg/m³	Density 1, kg/m³	Average
W0	812.9	843.2	828.0
OP1	821.6		
OP4	295.0	333.9	314.5
OP5	667.6		

Table 13: Summary of the available data per well, utm well coordinates and data provider

Well	W0	WI1	WI2	WI3	OP1	OP2	OP3	OP4	OP5
RT elevation (m)	26	19	19	19	19	19	19	25	19
Well Head X (utm)	148818	148406	148917	146846	147774	147819	147810	147772	147767
Well Head Y (utm)	9146077	9146237	9147297	9144616	9146383	9146378	9146367	9146408	9146396.4
Layers	9	8	8	3	8	8	3	3	3
Data Available	BHP, Well logs, well tops, well trajectories, time-depth laws, checkshots, well markers, completion screens, MDT and RFT data								
Data Provider	Sonangol E.P								

Table 14: Model and parameter information

Model information		Parameter information	
Total number of cells	1007181	**Imput parameters**	**Source**
Number of cells (x)	63	Pressure	Production data
Number of cells (y)	73	Total rate	Production data
Number of cells (z)	219	Pemeability	Estimated from logs
Grid cell dimension, x (m)	100	Water saturation	Estimated from logs
Grid cell dimension, y (m)	100	Porosity	Estimated from logs
Grid cell dimension, z (m)	100	GOR	Estimated from logs
Number of imput wells	8	Attribute data	Seismic

E.3 Plots of the behaviour of the reservoir pressure with time
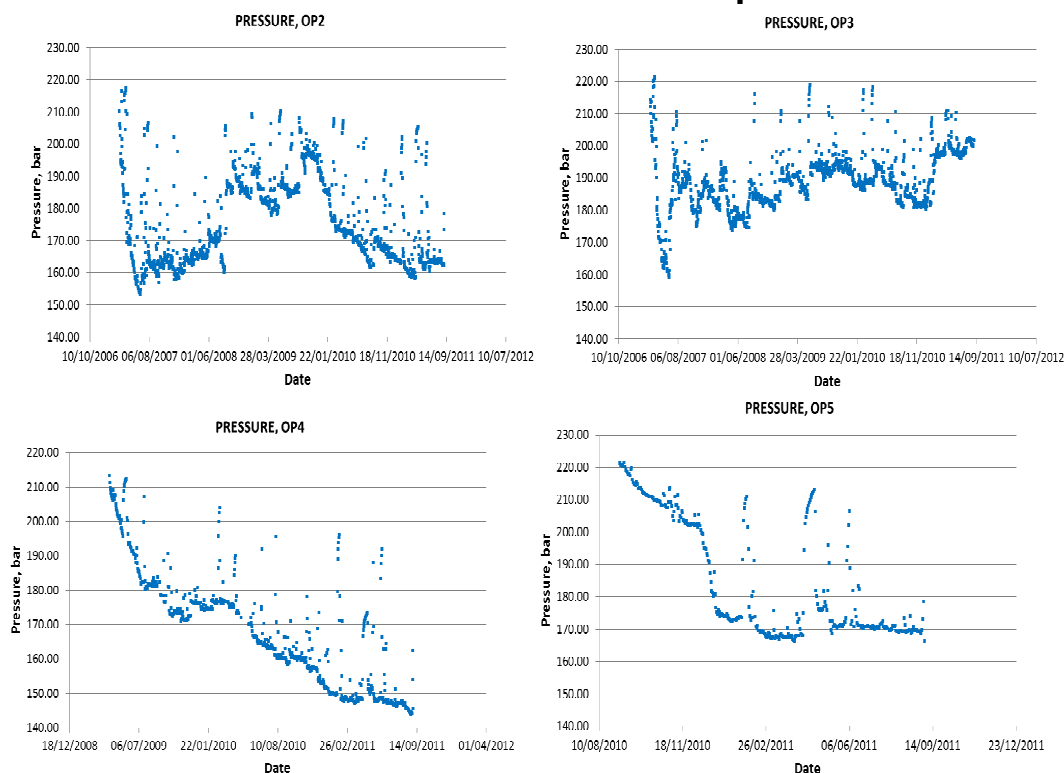
Figure 52-E3: Behaviour of the Reservoir pressure with time

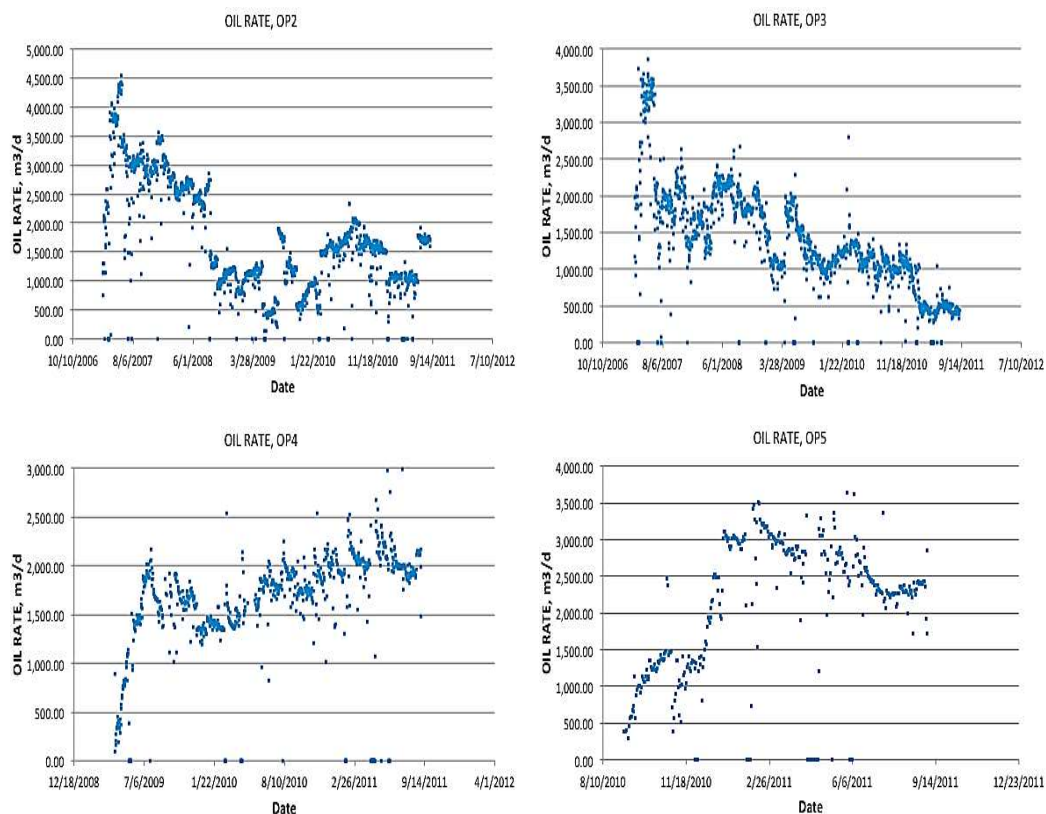## E.4   Plots of the behaviour of the oil flow rate with time

Figure 53: Behaviour of the oil flow rate with time

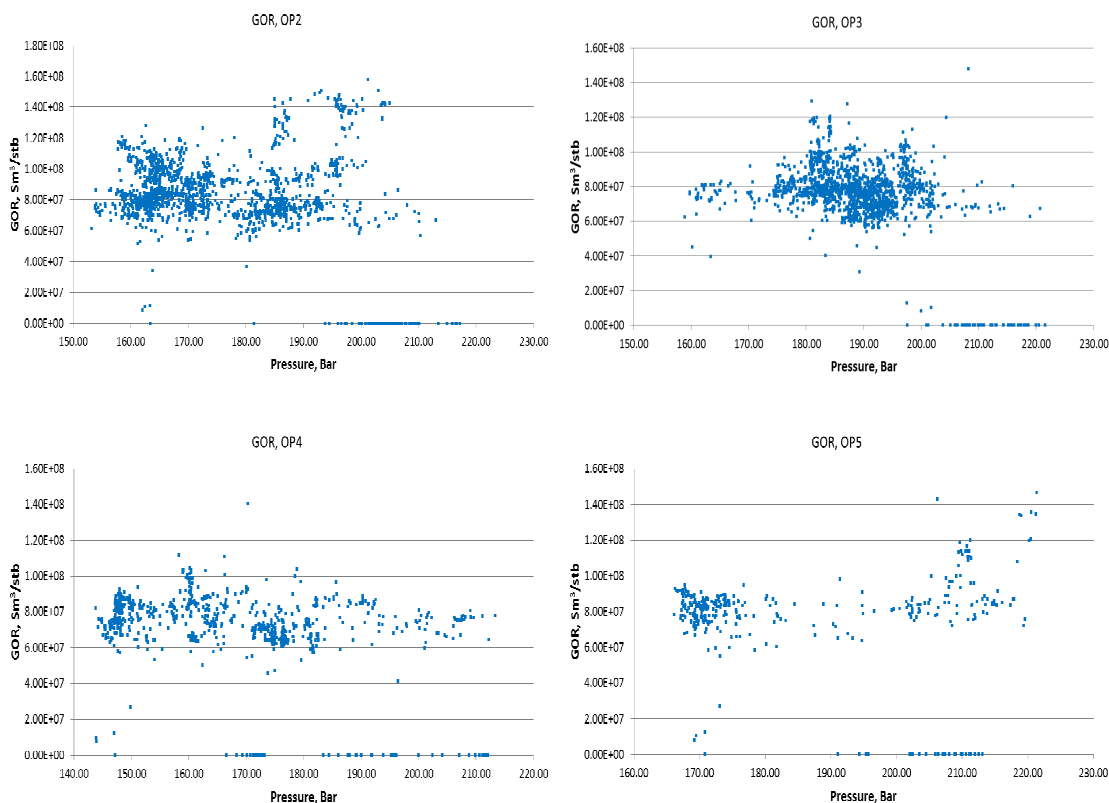## E.5   Plots of the behaviour of the GOR with pressure and GOR with time

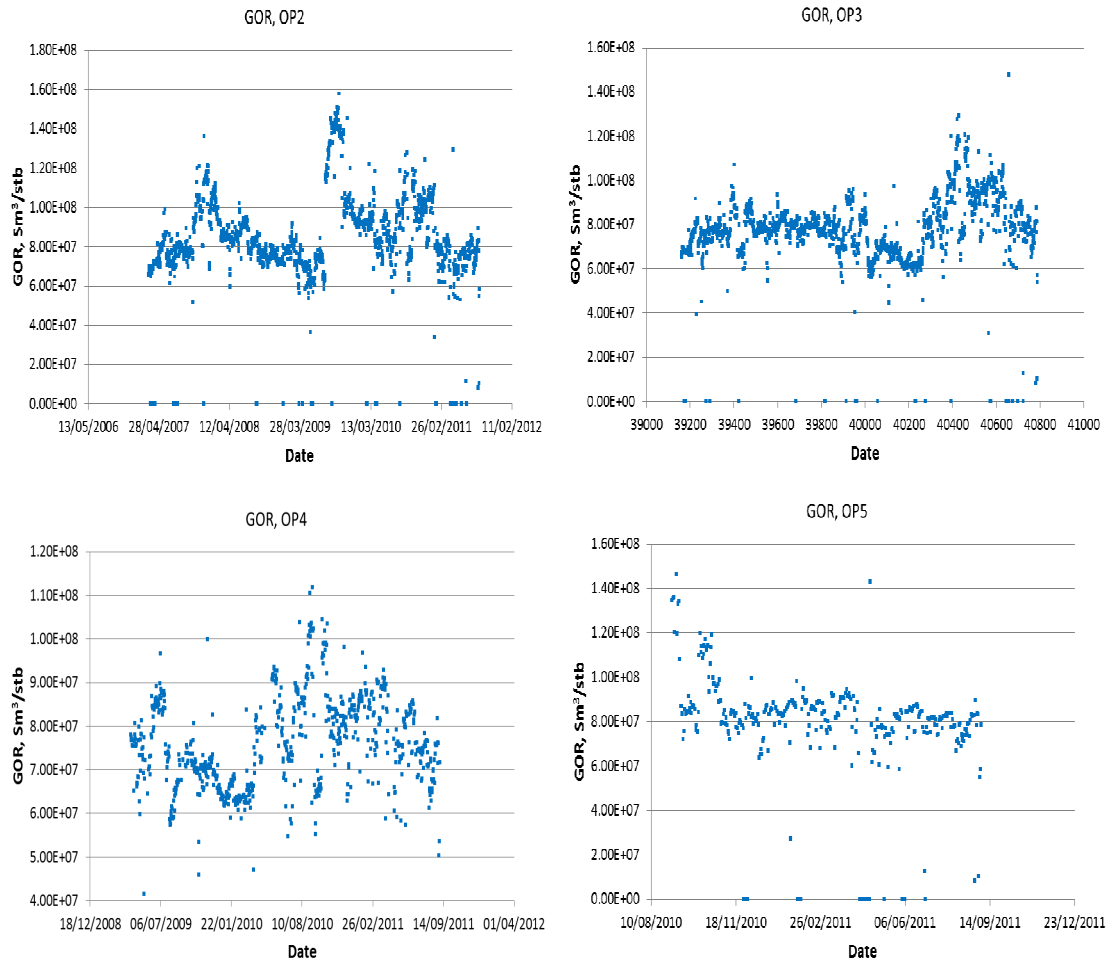**Figure 54-E5:** Behaviour of the GOR vs. Pressure per well

Figure 55-E5: Behaviour of the GOR vs. Pressure with time

F. Regularization and smoothing

Following (Gonzalez-Rodrighez et al., 2005) the regularization approach used to smooth the edges and remove visual discontinuity inherent from the manipulation of matrices of data was as follows:

Given that the initial field permeability is know at well locations and considering that it changes with time and position:

$$\frac{\partial K}{\partial t} = \beta \left(\frac{\partial^2 K}{\partial x^2} + \frac{\partial^2 K}{\partial y^2} \right) = (K_0 - \alpha K) \qquad \text{(F-1)}$$

if K_0 is initial permeability, $(K_0 - \alpha K)$ is the time-dependet heating source and fixed time-step is $\delta t = \theta$ then equation (F-1) can be written as:

123

$$\frac{K^{n+1}-K^n}{\theta} = \beta \triangle K^{(n)} - \left(K_0 - \alpha K^{(n)}\right) \tag{F-2}$$

$$\nabla K_{\partial \Omega}.\vec{n} = 0$$

where $n = 1, 2, 3, \dots, N$ and $\beta = \alpha \gamma$. Expanding equation (F-2) yields:

$$K^{n+1} = K^n + \theta\left(\beta.\Delta K^n + \alpha K^n - K_0\right) \tag{F-3}$$

Once a number n of iterations have been permormed a set of boundary conditions have to used:

$$K(0) = K_0$$

The initial permeability K_0 to be smoothed will be the output from the permeability estimated by the numerical models in chapter 4.

Applying the regularization procedure to the data misfit from the original permeability distribution can be regularized even if n is small (i.e.: N=5 or N=10). This procedure is mostly useful during the computer model using the 4D seismic because of the need to smooth the sharp discontinuities from the permeability-estimated results.

Using Taylor series expansion using constant grid block sizes, parameter ΔK in equations (F-3) was optimized for use with computer software, taking the form:

$$\Delta K\left(i, j\right) = K_{i+1,j} - 2K_{i,j} + K_{i-1,j} + K_{i,j+1} - 2K_{i,j} + K_{i,j-1} \tag{F-4}$$

The the final expression for regularization becomes:

$$\Delta K\left(i, j\right) = K^n + \theta\left[\beta.\left(K_{i+1,j}^n - 2K_{i,j}^n + K_{i-1,j}^n + K_{i,j+1}^n - 2K_{i,j}^n + K_{i,j-1}^n\right) + \alpha K^n - K_0\right] \tag{F-5}$$

G. Pressure saturation inversion

Here a correlation is developed between reservoir properties (i.e.: saturation, pore pressure and porosity) and seismic attributes (pressure/shear velocities and bulk rock density). The development of the notation here derived follows the analogy of Gassmann–Biot (Gassman, 1977; Biot, 1956).

From the following reservoir properties

S = Saturation

$P_\emptyset$ = Pore pressure

Ø = Porosity

It can be obtained that

$$P_{ef} = P_{ob} - P_{por} \tag{G-1}$$

$$C = 9.5 - \left(\phi - \phi_i\right) \times 28 \tag{G-2}$$

Where P_{eff} is the effective pressure, C is the average number of contact per grain, P_{ob} is the overburden pressure and $Ø_i$ is the initial porosity.

In order to calculate the effective bulk K_{HM} and shear G_{HM} moduli's, this approach considers Hertz-Mindlin theory (Mindlin & Deresiewicz, 1953)

$$K_{HM} = \left[\frac{C^2 \left(1-\phi_i\right)^2 G^2}{18\pi^2 \left(1-v\right)^2} \times P_{eff} \right]^{\frac{1}{3}} \tag{G-3}$$

$$G_{HM} = \frac{5-4v}{5(2-v)} \left[\frac{3C^2 \left(1-\phi_i\right)^2 G^2}{2\pi^2 \left(1-v\right)^2} \times P_{eff} \right]^{\frac{1}{3}} \tag{G-4}$$

Where v is the grain Poison's ratio and G is the shear modulus

In order to find the effective and shear moduli (K_{HM} and G_{HM}) at different porosity Ø, the heuristic modified Hashin-Strikman lower bound is used

$$K_{eff} = \left[\frac{\frac{\phi}{\phi_i}}{K_{HM} + \frac{4}{3}G_{HM}} + \frac{1-\frac{\phi}{\phi_i}}{K_{HM} + \frac{4}{3}G_{HM}} \right]^{-1} - \frac{4}{3}G_{HM} \tag{G-5}$$

$$G_{eff} = \left[\frac{\frac{\phi}{\phi_i}}{G_{HM} + \frac{1}{6}G_{HM}\left(\frac{9K_{HM}+8G_{HM}}{K_{HM}+2G_{HM}}\right)} + \frac{1-\frac{\phi}{\phi_i}}{G + \frac{1}{6}G_{HM}\left(\frac{9K_{HM}+8G_{HM}}{K_{HM}+2G_{HM}}\right)} \right]^{-1} - \frac{1}{6}G_{HM}\left(\frac{9K_{HM}+8G_{HM}}{K_{HM}+2G_{HM}}\right)$$

(G-5)

Where K is the grain modulus.

Analysis of logs, cores, and seismic data is associated with typical rock physics problems that result from the use of seismic velocities in rocks saturated with one fluid to predict those of rocks saturated with a second fluid, or equally, predicting saturated-rock velocities from dry-rock velocities, and vice versa.

When seismic waves pass through a rock, the waves induce pore pressure change to the rocks; this pressure resists the compression of the rock and therefore

stiffens the rock. This phenomenon can also be observed when compression pressure is induced to a rock.

The low-frequency Gassmann–Biot (Gassmann, 1951; Biot, 1956) theory predicts the resulting increase in effective bulk modulus, K_{sat}, of the saturated rock using the following equation:

$$S_o + S_w = 1 \tag{G-6}$$

$$K_{fl} = \left(\frac{S_w}{2.715} + \frac{S_o}{0.5} \right)^{-1} \tag{G-7}$$

$$\rho_{fl} = S_w + \frac{4S_0}{5} \tag{G-8}$$

$$K_{sat} = K_{eff} + \frac{\left(1 - \dfrac{K_{eff}}{K}\right)^2}{\dfrac{\phi}{K_{fl}} + \dfrac{1-\phi}{K} - \dfrac{K_{eff}}{K^2}} \tag{G-9}$$

Where K_{eff} is effective bulk modulus of dry rock, K_{sat} is the effective bulk modulus of the rock with pore fluid, K is the bulk modulus of mineral material making up rock, K_{fl} is the effective bulk modulus of pore fluid and Ø is the porosity.

The Gassman equation is also presented as

$$\frac{K_{sat}}{K - K_{sat}} = \frac{K_{eff}}{K - K_{eff}} + \frac{K_{fl}}{\phi(K - K_{fl})} \tag{G-10}$$

$$\mu_{sat} = \mu_{dry}; \quad \mu_{sat} = \mu_{dry}$$

where K_{dry} is the effective bulk modulus of dry rock, K_{sat} is the effective bulk modulus of the rock with pore fluid, K is the bulk modulus of mineral material making up rock, K_{fl} is the effective bulk modulus of pore fluid, f is the porosity, μ_{dry} is the effective shear modulus of dry rock, and μ_{sat} is the effective shear modulus of rock with pore fluid

$$K_{sat} = \frac{\phi\left(\dfrac{1}{K} - \dfrac{1}{K_{fl}}\right) + \dfrac{1}{K} - \dfrac{1}{K_{eff}}}{\dfrac{\phi}{K_{eff}}\left(\dfrac{1}{K} - \dfrac{1}{K_{fl}}\right) + \dfrac{1}{K}\left(\dfrac{1}{K} - \dfrac{1}{K_{eff}}\right)} \tag{G-11}$$

$$\frac{1}{K_{sat}} = \frac{1}{K} + \frac{\phi}{K_{eff} + \dfrac{KK_{fl}}{K - K_{fl}}} \tag{G-12}$$

$$K_{eff} = \frac{K_{sat}\left(\dfrac{\phi K}{K_{fl}}+1-\phi\right)-K}{\dfrac{\phi K}{K_{fl}}+\dfrac{\phi K_{sat}}{K}-1-\phi}$$ (G-13)

In order to compute the seismic attributes pressure velocity (V_p), shear velocity (V_s) and bulk modulus (K_b) a new expression needs to be introduced

$$\rho = \frac{\phi}{\rho_{fl}}+(1-\phi)\times\rho_{grain}$$ (G-14)

$$V_p = \sqrt{\frac{K_{sat}+\dfrac{4}{3}\mu}{\rho}}$$ (G-15)

$$Vs = \sqrt{\frac{\mu}{\rho}}$$ (G-16)

Where ρ_{grain} is constant, μ is the shear modulus, which does not depend on fluid and is equal to G_{eff}.

The approach above is a detailed workflow that can be used to compute seismic attributes (Vp, Vs and Kb) from reservoir properties (S, Pø and Ø). As a requirement for attribute computation, reservoir properties must exist; hence the petro-elastic model is dependent on reservoir data and constrained by its quality.

This project used the statistical inversion approach proposed by (MacBeth, et al., 2005) to estimate reservoir properties using the seismic attributes extracted from the reservoir model; this approach was derived using a two-phase reservoir in which the seismic attribute A, depends on the reservoir thickness (τ), lithology (L), porosity (ϕ), and reservoir pressure (P) and oil saturation (S_o):

$$A = A(x, y, \tau, L, \phi, P, S_o)$$ (G-17)

where A is a mapped function of x and y, defined on the picked horizon of interest. A relationship between 4D seismic and dynamic reservoir changes (pressure and saturation) was established through the formula:

$$\frac{\Delta A(x,y)}{\overline{A_b}} \approx C_S \frac{\Delta S_o(x,y)}{\overline{S_{oi}}} + C_P \frac{\Delta P(x,y)}{\overline{P_i}}$$ (G-18)

where ΔA, ΔS_o and ΔP represent changes in seismic attribute, oil saturation and reservoir pressure respectively; $\overline{A_b}$ represent average baseline response, $\overline{S_{oi}}$ and $\overline{P_i}$

127

are the average initial saturation and pressure in the reservoir. C_s and C_p represent dimensionless coefficients used to calibrate the production data to the 4D seismic signatures.

Equation (G-18) correlates attribute data with dynamic data, considering the initial and final times, this equation can be transformed into:

$$A_0(x,y) - A_1(x,y) \approx C_S \left[S_{n,0}(x,y) - S_{n,1}(x,y) \right] + C_P \left[P_0(x,y) - P_1(x,y) \right] \qquad \text{(G-19)}$$

Because only initial saturation data was estimated from log, through pressure saturation inversion, the saturation at *T1* can be estimated using the expression:

$$S_{n,1}(x,y) \approx \frac{\left\{ \left[A_0(x,y) - A_1(x,y) \right] + C_P \left[P_0(x,y) - P_1(x,y) \right] \right\}}{C_S} + S_{n,0}(x,y) \qquad \text{(8-14)}$$

The equation above used to estimate the saturation of any fluid (S_{oil} or S_{water}) at a given time (in this case *T1*) given that attribute and pressure information are available at *T0* and *T1* in addition to the initial saturation information. Similar to the estimation of saturation, any parameter in (2-14) can be estimated given the initial distribution of the parameter is known and the other parameters to satisfy the equation are available or can be estimated.

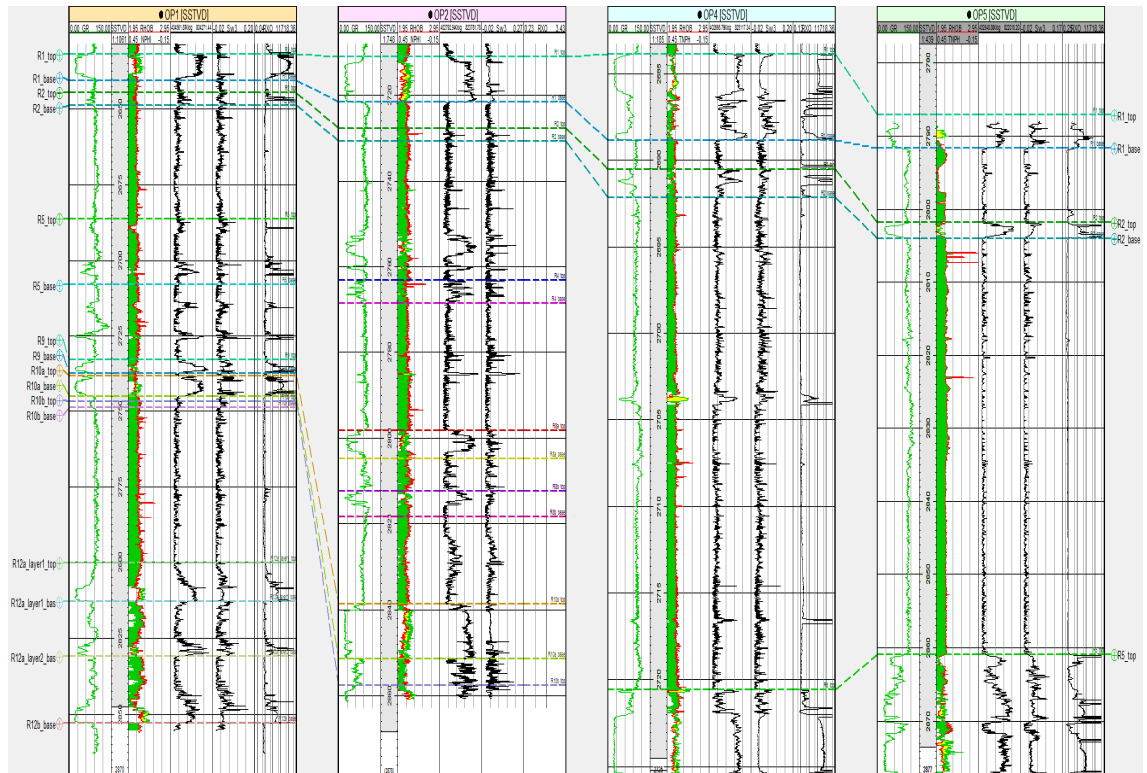# H. Images from the Dalia reservoir model

Figure 56-H: Well correlation of Dalia producing wells OP1-OP5 showing GR, initial water saturation estimated using Coates model and initial permeability estimated using Timur model.
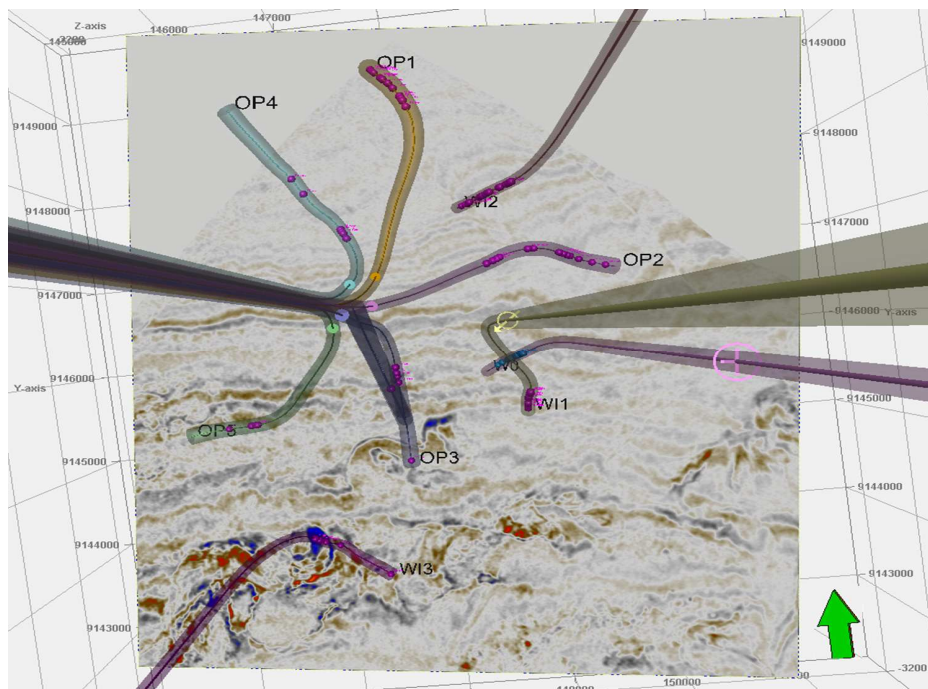

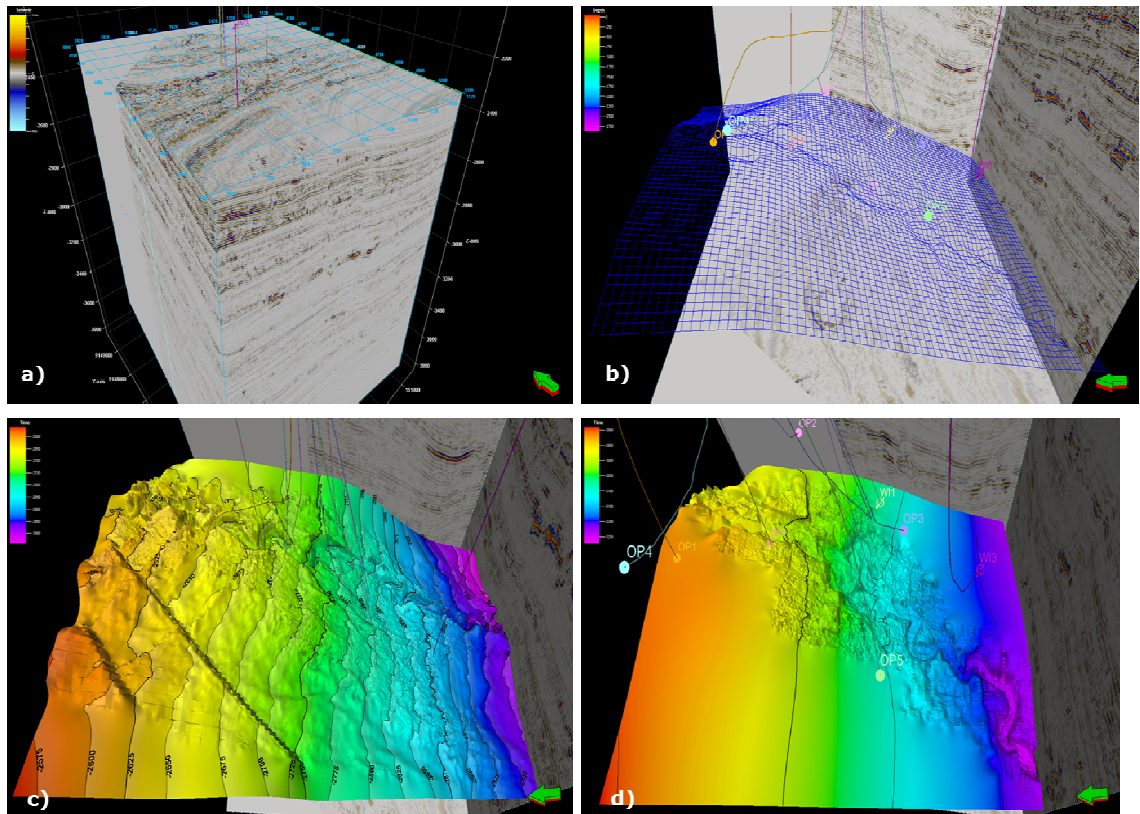**Figure 57-H:** Location and distribution of the drilled wells and seismic plane -3131

Figure 58-H: a) Display of the rendered seismic volume of Dalia Field at T0. **b)** Display of a seismic Inline and X-line and the location of the 100x100 3D grid. **c)** Display of a seismic Inline and X-line and the interpreted top surface of reservoir R1. **d)** Display of a seismic Inline and X-line and the interpreted base surface of reservoir R16.
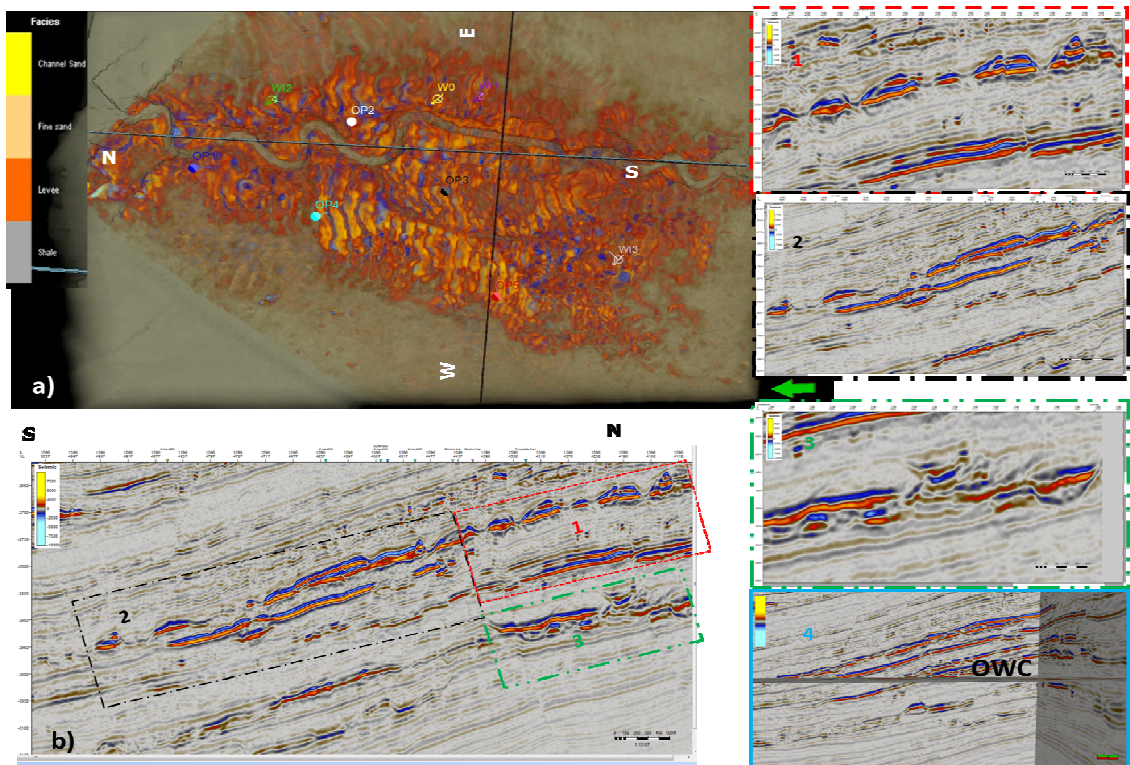
Figure 59-H: a) Geobody extraction of the uppermost reservoir showing sedimentological information. b) E-W Cross-section (X-line 4360) showing the 4 turbiditic channel-levee complexes and a close-up through each one: 1 – close up of the Upper complex; 2 – Close up
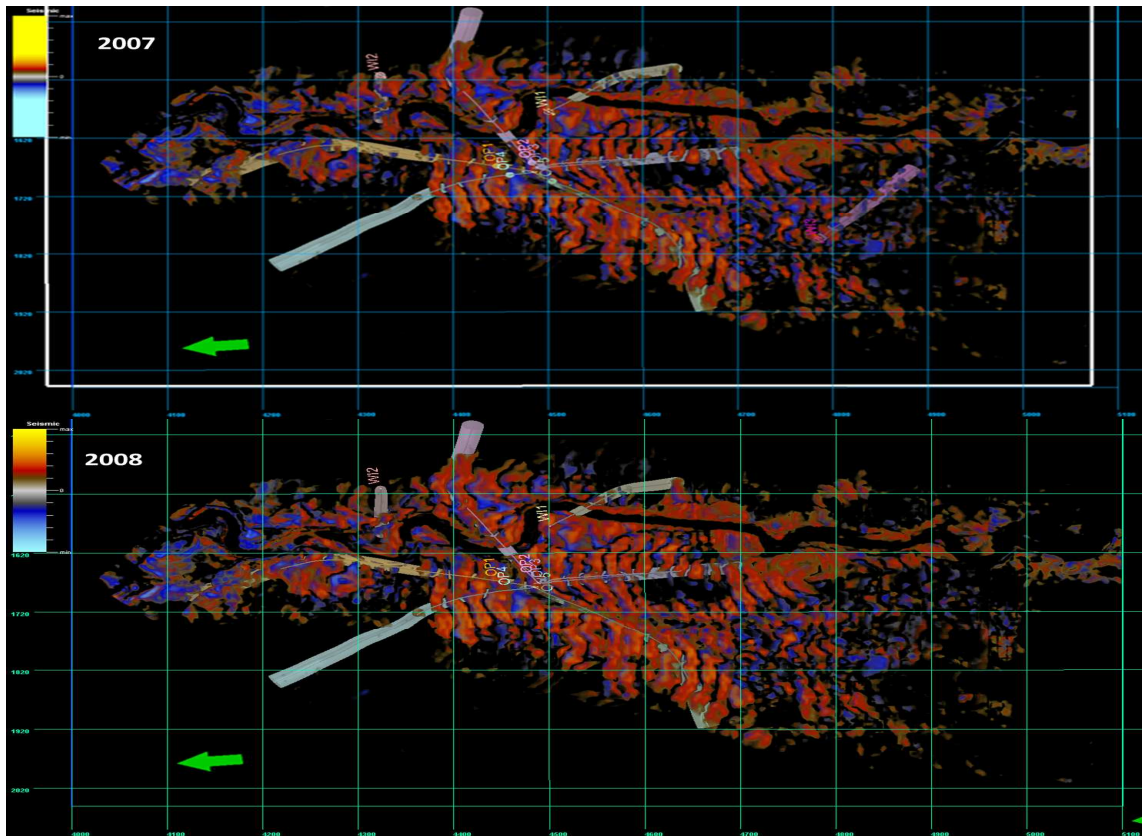
Figure 60-H: Attribute extraction (P-wave) amplitude of seismic through the Upper complex showing the N-S channel, the relative drop in amplitude and the location of the (gree arrow points north). **Top:** 1999 survey; **Bottom:** 2008 survey.
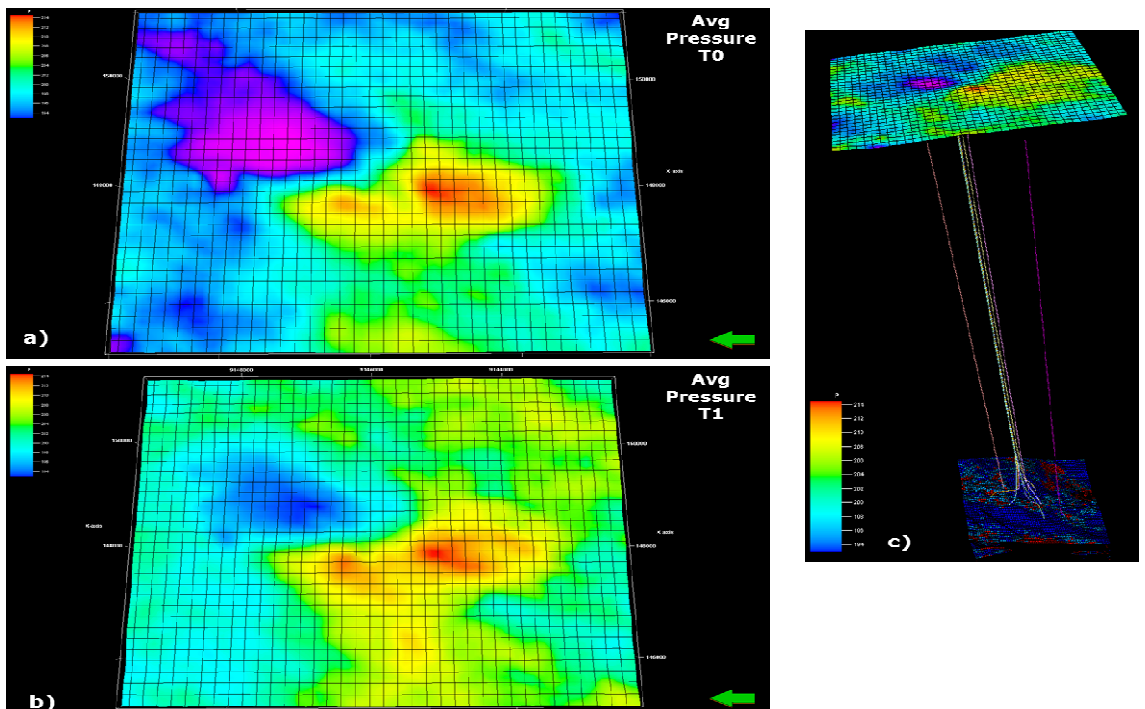

Figure 61-H: Maps of the reservoir pressure **a)** Average (2D) reservoir pressure at T0. **b)** Average (2D) reservoir pressure at T1. **c)** 3D model and arithmetic average (2D) map of the reservoir property (pressure).
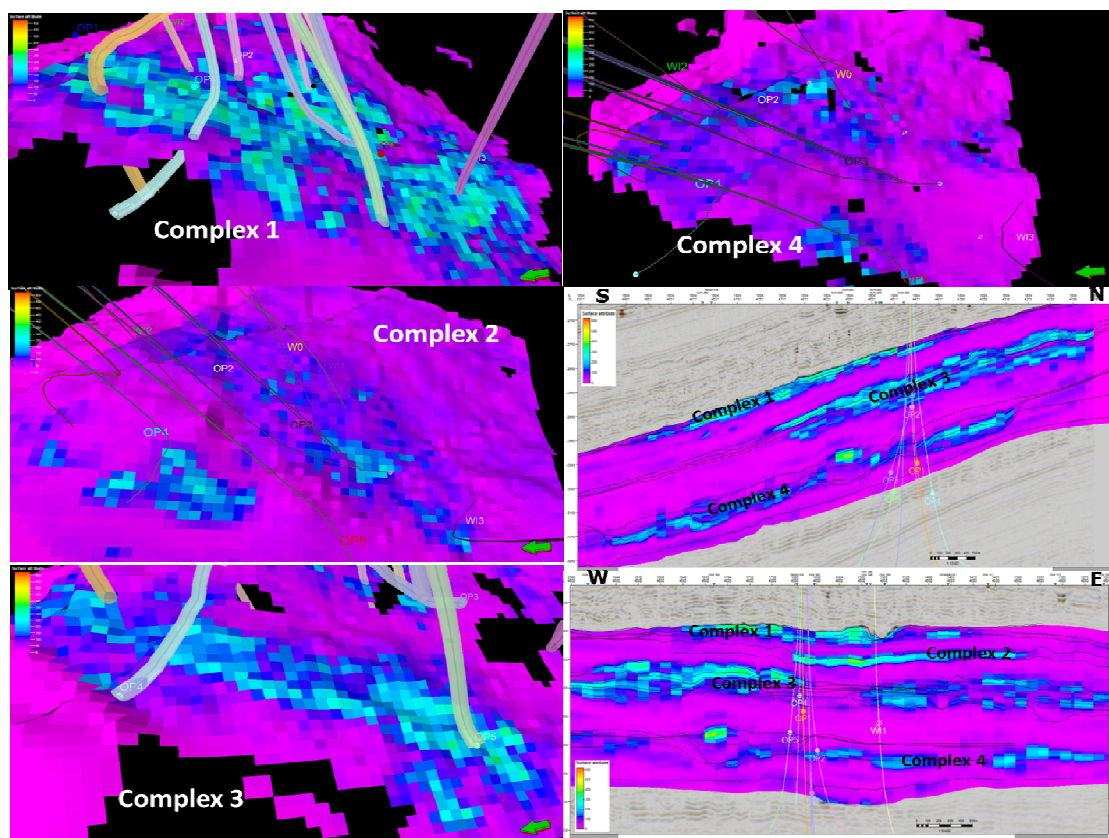
131

Figure 62-H: Seismic attribute maps (RMS amplitude) of the different channel-levee complexes at T0.
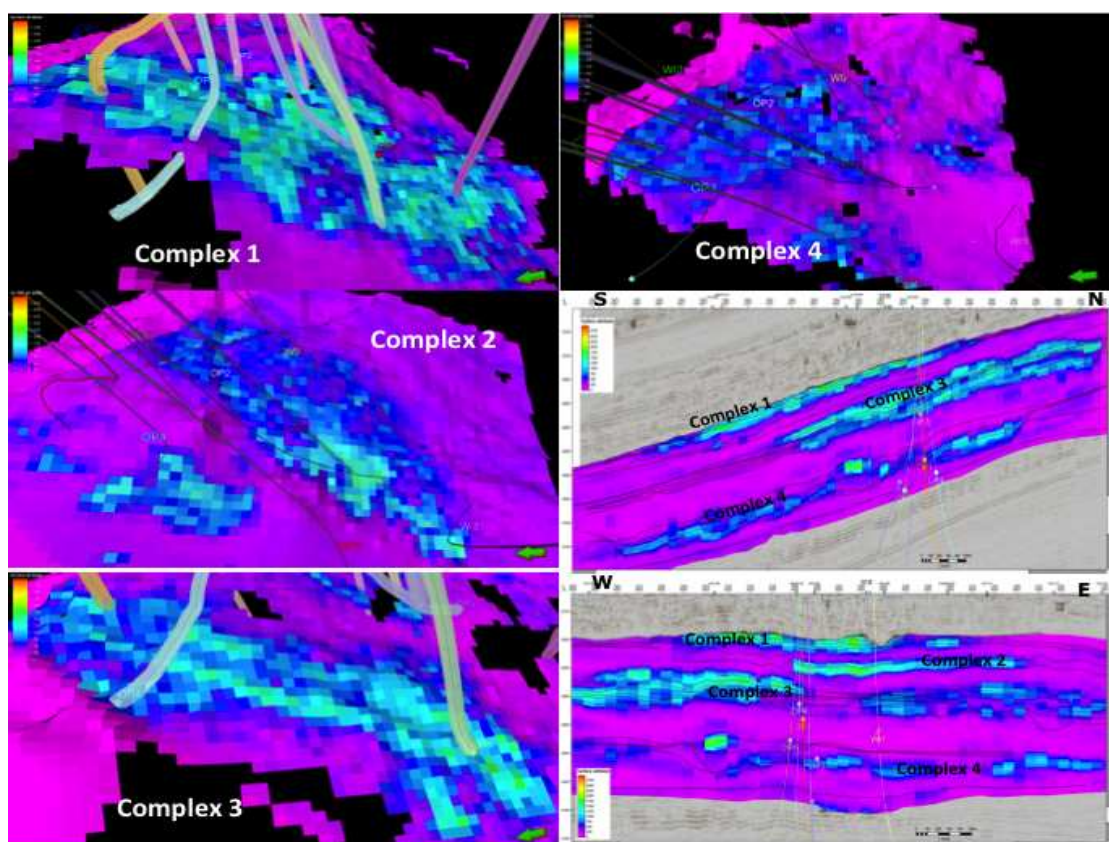

Figure 63-H: Seismic attribute maps (RMS amplitude) of the different channel-levee complexes at T1.
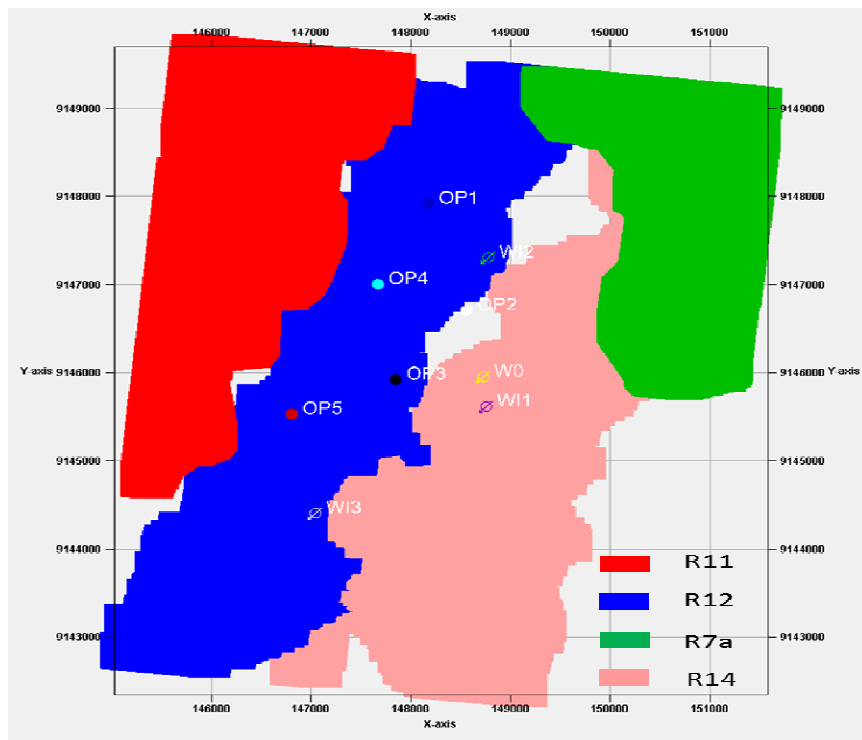
Figure 64-H: Geometry of some of the reservoir layers extracted from the reservoir models of the Dalia Field. The image is to be analysed in comparison with the sedimentological model in Fig 2b.
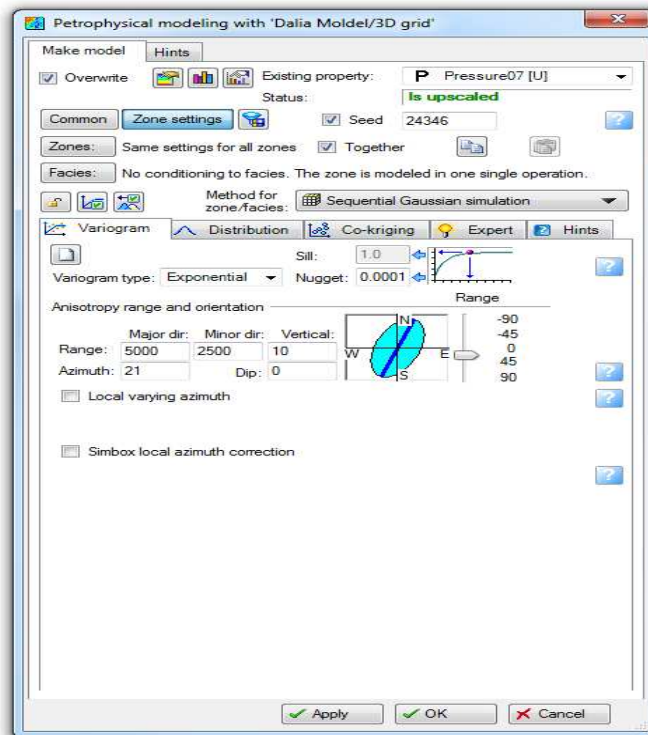

Figure 65-H: Petrophysical modelling pane showing the exponential variagoram type used for the distribution of the properties in teh interwell areas
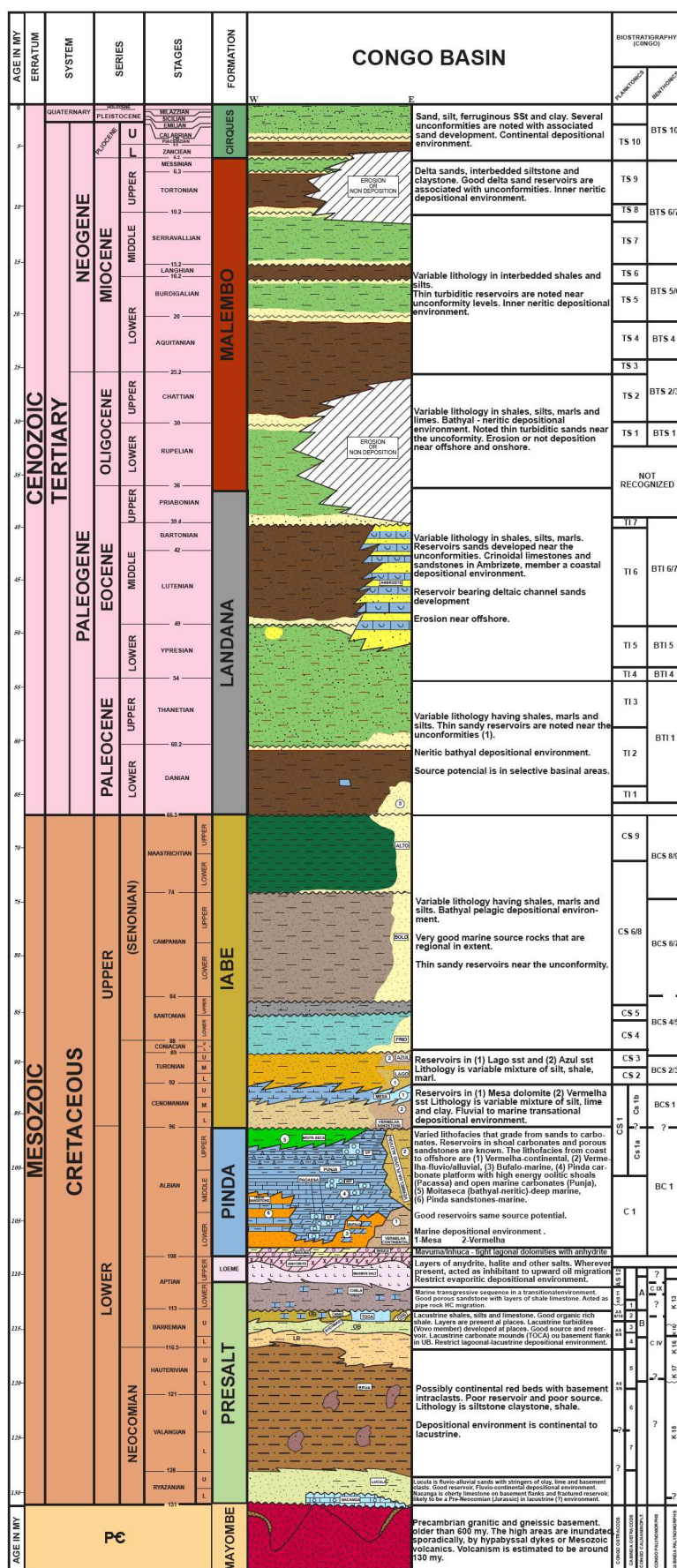
Figure 66-H: Schematic view of Albian Platform in Congo Basin. Varied lithologies are noted across the basin from onshore to present day shelf-slope (source: Angolan Ministry of Petroleum).